PATIENT SPECIFIC CEREBRAL ARTERIAL BLOOD FLOW MODELLING

JASPER HERMANNUS GERHARDUS HELTHUIS

ISBN: 978-94-6375-417-0

Cover design: evelienjagtman.com based on an idea by Jasper Helthuis
Lay-out: evelienjagtman.com
Printed by Ridderprint

The research presented in this dissertation and printing of this thesis was financially supported by a combined project of Netherlands Organisation for Health Research and Development (ZonMw) and The Department of Biotechnology (DBT) of the Ministry of Science and Technology of the Government of India under project number 11.631.0005.

PATIENT SPECIFIC CEREBRAL ARTERIAL BLOOD FLOW MODELLING

Patiënt specifieke cerebrale arteriële bloedstroom modellering

(met een samenvatting in het Nederlands)

Proefschrift

ter verkrijging van de graad van doctor aan de Universiteit Utrecht op gezag van de rector magnificus, prof.dr. H.R.B.M. Kummeling, ingevolge het besluit van het college voor promoties in het openbaar te verdedigen op dinsdag 25 juni 2019 des middags te 12.45 uur

door

Jasper Hermannus Gerhardus Helthuis

geboren op 6 mei 1989
te Almelo

Promotor:
Prof. dr. A. van der Zwan

Copromotor:
Dr. T.P.C. van Doormaal

Content

1

Genereral introduction

Genereral introduction

In literature modelling of cerebral blood flow is of growing interest since decades ranging from physicians trying to better understand diseases to physicist purely finding interest and joy in studying the many complex properties of its bloodflow.[1] For this purpose more insight in various physiological parameters such as the characteristics of the fluid (blood) and the transporting system (cerebral arteries) are of major importance.

Fluid (blood)

The force thriving blood through the arterial circulation is the pressure and flow wave generated by the heart. During each contraction it generates a wave propagation through the arterial system making blood flow pulsatile. Hence, blood flow models often assume pulsatile properties.[2–4] However, for simplification many authors assume a steady state without pulsatility, at the expense of some accuracy.[5–8]

When a fluid is propagating in any system it shows either a laminar or turbulent flow. In a laminar flow, particles are moving in straight lines along another in the same direction, creating an easier to predict flow. In turbulent flow however, movement of particles is more chaotic. Particles move in different directions compared to another.

When blood flows through a smooth artery, more distal from the heart, it is known to show a more laminar flow. However, closer to the heart, but also in pathology like an aneurysm or a stenosis, blood flow is showing a more turbulent nature.[9,10]

Like all fluids, blood has a certain viscosity. This is the resistance of a fluid to flow. Depending on the behaviour of their viscosity, fluids can be divided into two groups. (a) Newtonian fluids and (b) non-Newtonian fluids.

In Newtonian fluids the viscosity remains constant, regardless of the amount of forces applied. A well-known example is water. When one tries to squeeze water out of a plastic bottle, it leaves the bottle twice as hard when the bottle is squeezed twice as hard. The viscosity and thus the resistance to flow of water stays constant.

Non-Newtonian fluids on the other hand are different. In these fluids, the viscosity changes depending on the forces applied.

Many examples exist of which some well-known are sauces (such as ketchup, garlic sauce, mustard and mayonnaise), toothpaste and paint. These fluids show a change in their viscosity when applying a changing force. This means that when one applies a small force on a bottle containing a sauce, for example holding it upside down, the sauce will not leave its bottle and show a high viscosity (e.g. high resistance to flow). However, when applying a large force (for example shaking), the viscosity of the sauce changes and it behave almost like water, very easily leaving the glass bottle (e.g. low resistance to flow).[11–14]

Blood is known to behave non-Newtonianly as blood cells are known to change in viscosity at different shear rates, making modelling more difficult. However, for more simplified models, blood can is often assumed to be a Newtonian fluid as its change in viscosity is known to be non-significant at the shear rates present in most of the arterial circulation.[15]

Beside viscosity, blood has, as all fluids, a certain density. Depending on the compressibility of a fluid this density will increase when a higher pressure is applied. Blood is known to be a compressible fluid with its compressibility being different depending on its composition. An increase in the percentage of red blood cells, as reflected by a change in haematocrit, will lead to a change in compressibility. For most blood flow models however, considering blood to be incompressible will likely suffice.[16]

Arterial wall elasticity

When modelling blood flow, beside physiological properties of blood (the fluid), one has to consider properties of the arterial wall (the structure) as well. Arterial walls are made of multiple layers, form inside to outside: (a) the tunica intima, the innermost layer which is in contact with blood and made of endothelial cells and a supportive layer of elastic lamina. (b) the tunica media which is formed by muscle cells and some elastic connective tissue. (c) the tunica adventitia, which is made mostly from connective tissue.[15]

The arterial wall is known to be elastic, meaning that when a force is applied the arterial wall is deformed. In case of an increased intraluminal pressure the arterial wall is stretched outwards leading to a larger local intraarterial volume. This change in volume for an isolated arterial segment for a specific change in pressure is called the compliance of the arterial segment. The layer of muscles in the arterial wall, changes of the arterial wall due to atherosclerosis and other diseases such as aneurysmal formation can lead to a change in the elastic properties of the arterial wall.[15]

This elasticity has effect on blood flow. Many models often assume arterial walls to be rigid for the sake of simplification.[17] During systole the blood pressure increases, leading to stretching of the arterial wall. During diastole the pressure decreases, which leads to a reduction of the diameter of the arteries. This aids in perfusion during diastole.[15,18]

Dimensions in blood flow modelling

In mathematical blood flow modelling a differentiation between multiple dimensions of modelling is made.

In zero-dimensional (0D) modelling a lumped description of the arterial tree with or without a relationship to time is given. This provides a relationship between pressure and flow, but there are no spatial parameters (hence zero-dimensional), meaning that turbulences and flow wave propagation cannot be studied as these require information on space.[18]

In one- and two-dimensional (1D and 2D) models, spatial parameters are added. These models are also known as distributed models and are formed by splitting the arterial tree into smaller elements through which fluid flow can be propagated and more detailed information can be acquired on flow.[18]

Three-dimensional (3D) models contain information on blood flow in all three spatial directions (x, y and z). These models can capture complex 3D flow patterns (e.g. turbulences, vortexes). They can be used to capture more detailed characteristics on fluid and structure interaction in which properties such as wall shear stresses can be captured.[18]

Basic parameters

When performing mathematical blood flow modelling different parameters/results are of interest. Which parameters and results will be used and calculated depend on the usage case, complexity and dimensions of the model.

In 0D modelling as stated above a relationship between pressure and flow is given. Pressure is expressed as how much force is applied against the arterial wall. Its unit is described as amount of force per unit area. The Système International (SI) unit is Pascal (Pa) measured as newton per square meter. In medicine pressure is often measured as millimetres of mercury (mmHg) in which 1 mmHg is equal to 133,3 Pa.

As long as there is a pressure difference on two sides of a fluid, it will flow from one side to the other. This is measured as a volumetric flow rate, which is defined as the volume of fluid which passes a certain point per unit of time. Its SI unit is cubic metres per second (m^3/s) or millilitres per second (ml/s).

When moving from 0D modelling to higher level models, such as 3D models based on a fluid-structure interaction, the studying of many other parameters is possible. Properties of both the fluid and the arterial wall and their interaction can be calculated.

Within the fluid it is possible to study not only the volumetric flow rate, but also how fast separate particles are moving. This is known as velocity which is defined as change in position (distance travelled) during a unit of time, often in metres per second (m/s). When direction is known flow patterns can be shown ranging from laminar to turbulent flows.

For the arterial wall many properties can be calculated. It is possible to calculate pressure at specific points, giving a pressure distribution along the arterial wall. In case of pulsatile flow displacement of an arterial wall, measured in millimetres (mm) distance, can be provided. Distribution of wall tension, the stress due to stretching of an arterial wall in response to change in pressure, can also be calculated. This is denoted as an amount of force in Newton per unit of surface area in square metres (N/m^2). When blood is flowing through an artery its viscosity causes friction against the arterial wall. The tangential force per unit area caused by this friction on the surface of the arterial wall is called wall shear stress (WSS). WSS is also given in N/m^2.[19–24]

The circle of Willis

Unique in the cerebral arterial circulation is what is called the circle of Willis (circulus arteriosus cerebri Willisii). It is a central vascular structure in which the major cerebral arteries in varying ways are connected with another (figure 1). The afferent arteries are the two internal carotid arteries and the basilar artery of which the latter is fed by the two vertebral arteries.[25]

Each of the internal carotid arteries divides into two arteries, the anterior cerebral artery (ACA) and the middle cerebral artery (MCA). Usually the left and right ACA communicate through a connection between them called the anterior communicating artery (Acom).[25]

The basilar artery bifurcates into two posterior cerebral arteries (PCA). These both have a connection to the distal side of the internal carotid artery by a posterior communicating artery (Pcom). It is by the presence of the Pcom and Acom that blood can freely distribute among the major cerebral arteries.[25]

The complete version of the circle of Willis as described above however is only present in a small part of the population. Many variants exist with duplicated arteries or missing arteries. In addition and consequently also the sizes of the efferent vessels originating from the circle of Willis are highly variable.[26] This high variability of both the afferent as efferent vessels and of the Circle of Willis itself has a high impact on the distribution of cerebral blood flow.[27]

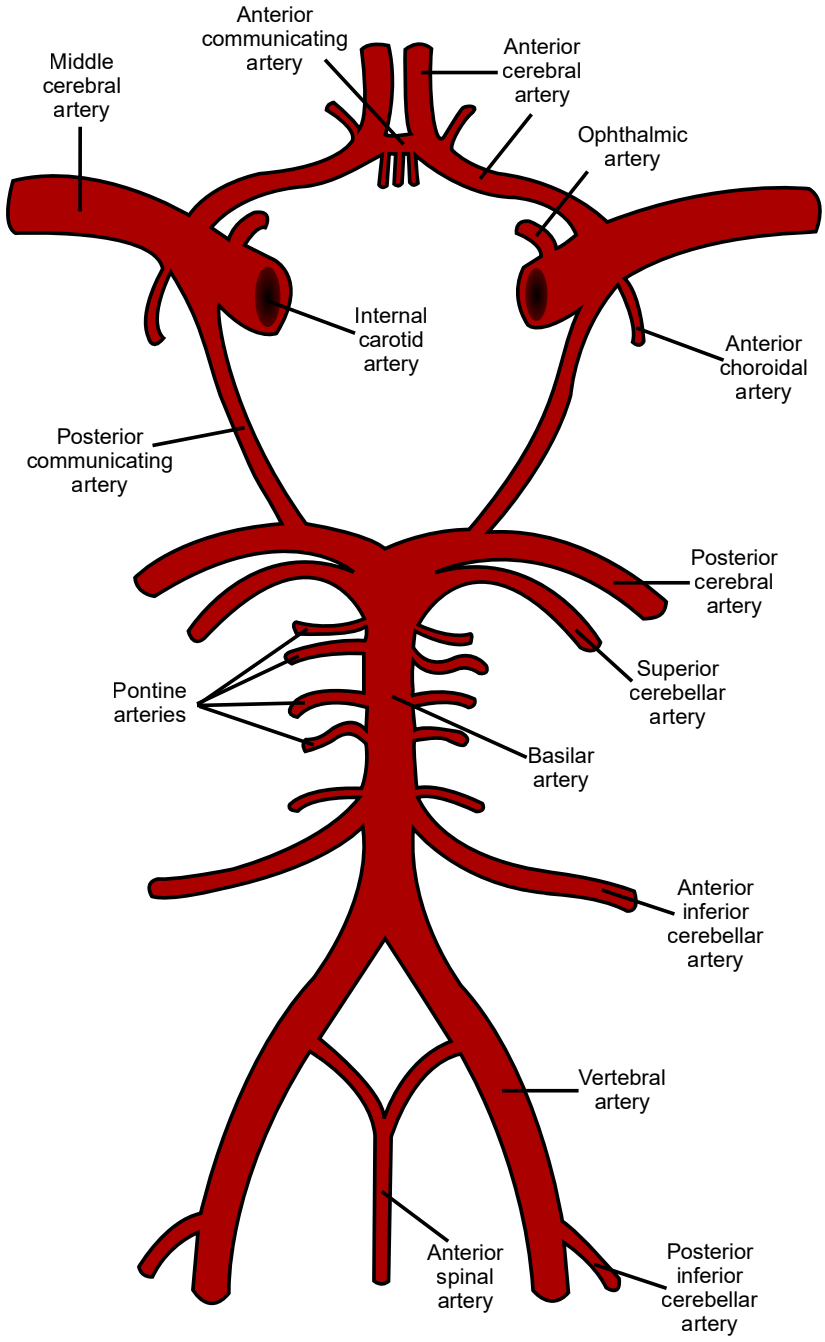

Figure 1: Schematic representation of the circle of Willis.
Illustration by Rhcastilhos. Reused and published under the Public Domain licence from Wikimedia commons

Need for patient-specific cerebral blood flow models

Cerebrovascular diseases are a major cause of morbidity and mortality each year.[28] Treatment of some of these diseases like complex aneurysms is a complex matter, often based on experience and relatively small studies. A patient-specific cerebral blood flow model could aid in selecting the most optimal and individualized treatment.

The prevalence of cerebral aneurysms accounts for 3.6-6% of the general population over the age of 30.[29] Untreated some of these aneurysms may lead to serious morbidity and mortality due to rupture. In case of rupture 25-50% off all patients will not survive and 50% of the surviving population have severe disabilities.[28,30] However, not all aneurysms will rupture and rupture risk is difficult to predict as many factors are involved. Patient-specific 3D flow modelling might aid in detecting aneurysms at risk for further growth or rupture and guide treatment.[23,31–33]

For aneurysms rupture risk estimation, 3D flow modelling might be needed as many complex parameters are of influence on rupture risk.

One example in which a lower dimensional patient-specific cerebral blood flow model could aid is in cerebrovascular revascularisation treatment in which a cerebrovascular bypass is used to replace or augment blood supply. Blood flow modelling could aid in selecting the appropriate recipient location of a bypass and consequently its size and length. Various indications exist for cerebrovascular bypass surgery.[34]

The first is a planned sacrifice of a vessel in the treatment of aneurysms or invading tumours. The above-mentioned cerebral aneurysms can grow in size to what are called complex and giant aneurysms (diameter >25mm). These aneurysm are often difficult to treat but are known to have an increased rupture risk.[35–38] When treating these aneurysm often one or more vessels need to be sacrificed.[34,39] When a tumour is invading arterial structures these also might need to be sacrificed and therefore replaced by a bypass.[34,40]

Flow augmentation is required when in certain regions blood flow supply is insufficient to meet the energy demand of the brain tissue. A well-known example is moyamoya disease. Patients suffer from an occlusive intracranial arteriopathy affecting mainly the distal ICA and proximal MCA. This progressing stenosis and finally occlusive diseases leads to formation of basal lenticulostriate collateral arteries. These patients are in

a state of increased risk for ischemia and haemorrhage. Flow augmentation could reduce the ischemia risk and in addition, reduce the formation of excessive collaterals, which in turn is expected to lower risk for haemorrhage.[41]

In the past augmentative bypass surgery was also frequently performed in ischemic stroke from atherosclerotic occlusion of the internal carotid artery.[34,42] However, the results of a well-known study did diminuate the use of this type of bypass surgery worldwide.[43] One of the criticism on this study were the too broad patient selection criteria within this study. Proper patient specific cerebrovascular modelling could help in selecting those patients that could benefit from augmentive bypass surgery.
Beside predicting optimal cerebrovascular bypass surgery, flow modelling can be used to predicting outcome of balloon occlusion testing (BOT). This is an invasive endovascular procedure used to access the ability of the cerebral collateral circulation. A balloon is temporary inflated in an artery of interest, during which a neurological evaluation takes place to access if there are any symptoms. In case of an asymptomatic neurological evaluation during a BOT it is assumed that an artery can be sacrificed for treatment of a variety of diseases. Using 1D modelling combined with patient-specific non-invasive measurement, Charbel et al. have shown that it is possible to predict the outcome of an BOT, possibly avoiding the need for this invasive procedure.[44]

In summary, there is a variety of cerebrovascular diseases in which blood flow modelling could aid in selecting the optimal treatment. For more complex indications such as predicting aneurysm rupture risk, in which many factors are involved, more complex 3D modelling is likely needed. However, for many other treatment decisions such as selecting an optimal bypass location or predicting outcome of a BOT, lower dimensional model can proof useful.

Aim and outline of this thesis

The aim of this thesis is to develop a simplified patient-specific cerebrovascular blood flow model that might be useful for future use in a clinical setting.

In **chapter II** we describe a 3D flow model using data of two patients who were treated for giant cerebral aneurysms using proximal and distal occlusion. This showed the strengths of such a model. However, it also showed the difficulties in 3D flow modelling. Hence, we believe a more simplified model would be more likely to succeed in clinic in the near future.

No simplified cerebral arterial blood flow model is currently used in a clinical setting. Therefore, we first performed a literature survey to identify causes that might have hampered development of such a simplified patient-specific cerebral blood flow model and solutions published in literature. (**chapter III**)

Important difficulties in cerebral blood flow modelling were shown to arise from distal boundary conditions which were hampered by a high degree of variability, autoregulation and collateral flow in the individual patient. To develop a model incorporating patient-specific distal boundary conditions we opted for usage of a structured arterial tree.

To enable these structured trees to be specific for the cerebral circulation more information on the branching patterns of the cerebral circulation were needed. Therefore, in **chapter IV** we validated a new method using 7T and 9.4T MRI scanning of plastic cerebral arterial casts to enable acquisition of these branching patterns.

Chapter V presents the data acquired using these MRI techniques combined with traditional manual measurements. In **chapter VI** we present and validate a simplified patient-specific model. This model consists of a set of 0D equation based on the Hagen-Poiseuille equations. The branching patterns as gathered in **chapter V** were used to generate distal boundary conditions combined with a simplified autoregulatory model.

Finally, the future possibilities and further possible developments are discussed in **chapter VII**.

References

1. Cerny, L. C. & Walawender, W. P. Leonhardi Euleri's "Principia pro motu sanguinis per arterias determinando". *J. Biol. Phys.* **2,** 41–56 (1974).
2. Hillen, B., Hoogstraten, H. W. & Post, L. A mathematical model of the flow in the circle of Willis. *J. Biomech.* **19,** 187–194 (1986).
3. Alastruey, J. *et al.* Modelling the circle of Willis to assess the effects of anatomical variations and occlusions on cerebral flows. *J. Biomech.* **40,** 1794–1805 (2007).
4. Reymond, P., Merenda, F., Perren, F., Rüfenacht, D. & Stergiopulos, N. Validation of a one-dimensional model of the systemic arterial tree. *Am. J. Physiol. Heart Circ. Physiol.* **297,** H208–H222 (2009).
5. Hillen, B. *et al.* Analysis of flow and vascular resistance in a model of the circle of Willis. *J. Biomech.* **21,** 807–814 (1988).
6. Moorhead, K. T., Doran, C. V, Chase, J. G. & David, T. Lumped parameter and feedback control models of the auto-regulatory response in the circle of willis. *Comput. Methods Biomech. Biomed. Engin.* **7,** 121–130 (2004).
7. Lodi, C. A. & Ursino, M. Hemodynamic effect of cerebral vasospasm in humans: a modeling study. *Ann. Biomed. Eng.* **27,** 257–273 (1999).
8. Cassot, F. *et al.* Hemodynamic role of the circle of Willis in stenoses of internal carotid arteries. An analytical solution of a linear model. *J. Biomech.* **33,** 395–405 (2000).
9. Numata, S. *et al.* Blood flow analysis of the aortic arch using computational fluid dynamics. *Eur. J. Cardio-Thoracic Surg.* **49,** 1578–1585 (2016).
10. Banks, J. & Bressloff, N. W. Turbulence Modeling in Three-Dimensional Stenosed Arterial Bifurcations. *J. Biomech. Eng.* **129,** 40 (2007).
11. Non-Newtonian Fluid. Available at: https://en.wikipedia.org/wiki/Non-Newtonian_fluid. (Accessed: 18th February 2019)
12. Koocheki, A., Ghandi, A., Razavi, S. M. A., Mortazavi, S. A. & Vasiljevic, T. The rheological properties of ketchup as a function of different hydrocolloids and temperature. *Int. J. Food Sci. Technol.* **44,** 596–602 (2009).
13. Bottiglieri, P. *et al.* Rheological characterization of ketchup. *J. Food Qual.* **14,** 497–512 (1991).
14. Chhabra, R. & Richardson, J. *Non-Newtonian flow and applied rheology: engineering applications*. (Butterworth-Heinmann, Elsevier, 2011).
15. Nichils, W. W., O'Rourke, M. F. & Vlachopoulos, C. *McDonald's Blood Flow in Arteries. Theoretical, Experimental and Clinical Principles*. (Hodder Arnold, 2011).
16. Wang, S. H., Lee, L. P. & Lee, J. S. A linear relation between the compressibility and density of blood. *J. Acoust. Soc. Am.* **109,** 390–6 (2001).
17. Steinman, D. A. in *Modeling of Physiological Flows* 1–18 (2012). doi:10.1007/978-88-470-1935-5_1
18. Vosse, F. van de & Stergiopulos, N. Pulse wave propagation in the arterial tree. *Annu. Rev. Fluid Mech.* **43,** 467–499 (2011).
19. Venkatasubramaniam, A. K. *et al.* A comparative study of aortic wall stress using finite element analysis for ruptured and non-ruptured abdominal aortic aneurysms. *Eur. J. Vasc. Endovasc. Surg.* **28,** 168–176 (2004).
20. Isaksen, J. G. *et al.* Determination of wall tension in cerebral artery aneurysms by numerical simulation. *Stroke.* **39,** 3172–3178 (2008).

21. Fillinger, M. F., Marra, S. P., Raghavan, M. L. & Kennedy, F. E. Prediction of rupture risk in abdominal aortic aneurysm during observation: wall stress versus diameter. *J. Vasc. Surg.* **37,** 724–732 (2003).
22. Hall, A. J., Busse, E. F., McCarville, D. J. & Burgess, J. J. Aortic wall tension as a predictive factor for abdominal aortic aneurysm rupture: improving the selection of patients for abdominal aortic aneurysm repair. *Ann. Vasc. Surg.* **14,** 152–157 (2000).
23. Can, A. & Du, R. Association of Hemodynamic Factors With Intracranial Aneurysm Formation and Rupture. *Neurosurgery* **78,** 510–520 (2016).
24. Katritsis, D. *et al.* Wall shear stress: theoretical considerations and methods of measurement. *Prog. Cardiovasc. Dis.* **49,** 307–29 (2007).
25. Hillen, B. Form and heamodynamics of the circulus arteriosus cerebri (Willisii). (1986).
26. van der Zwan, A., Hillen, B., Tulleken, C. A. & Dujovny, M. A quantitative investigation of the variability of the major cerebral arterial territories. *Stroke* **24,** 1951–9 (1993).
27. Krabbe-Hartkamp, M. J. *et al.* Circle of Willis: morphologic variation on three-dimensional time-of-flight MR angiograms. *Radiology* **207,** 103–111 (1998).
28. Hop, J. W., Rinkel, G. J., Algra, A. & van Gijn, J. Case-fatality rates and functional outcome after subarachnoid hemorrhage: a systematic review. *Stroke* **28,** 660–4 (1997).
29. Wardlaw, J. M. & White, P. M. The detection and management of unruptured intracranial aneurysms. *Brain* 205–21 (2000).
30. Hijdra, A., Braakman, R., van Gijn, J., Vermeulen, M. & van Crevel, H. Aneurysmal subarachnoid hemorrhage. Complications and outcome in a hospital population. *Stroke* **18,** 1061–7 (1987).
31. Cebral, J. R. *et al.* Characterization of cerebral aneurysms for assessing risk of rupture by using patient-specific computational hemodynamics models. *Am. J. Neuroradiol.* **26,** 2550–2559 (2005).
32. Sforza, D. M. *et al.* Hemodynamics in growing and stable cerebral aneurysms. *J.Neurointerv. Surg.* (2015).
33. H., M. *et al.* High WSS or low WSS? Complex interactions of hemodynamics with intracranial aneurysm initiation, growth, and rupture: toward a unifying hypothesis. *Am. J. Neuroradiol.* **35,** 1254–1262 (2014).
34. Sia, S. F. & Morgan, M. K. High flow extracranial-to-intracranial brain bypass surgery. *J. Clin. Neurosci.* **20,** 1–5 (2013).
35. Choi, I. S. & David, C. Giant intracranial aneurysms: development, clinical presentation and treatment. *Eur. J. Radiol.* **46,** 178–94 (2003).
36. McCormick, W. F. & Acosta-Rua, G. J. The size of intracranial saccular aneurysms. *J. Neurosurg.* **33,** 422–427 (1970).
37. Wiebers, D. O. *et al.* Unruptured intracranial aneurysms: natural history, clinical outcome, and risks of surgical and endovascular treatment. *Lancet (London, England)* **362,** 103–10 (2003).
38. Nakase, H. *et al.* Long-term outcome of unruptured giant cerebral aneurysms. *Neurol. Med. Chir. (Tokyo).* **46,** 379-84; discussion 384–6 (2006).
39. Esposito, G. & Regli, L. Surgical decision-making for managing complex intracranial aneurysms. *Acta Neurochir. Suppl.* **119,** 3–11 (2014).
40. Charbel, F. T. *et al.* Computerized hemodynamic evaluation of the cerebral circulation for bypass. *Neurosurg. Clin. N. Am.* **12,** 499–508 (2001).

41. Ng, J., Thompson, D., Lumley, J. P. S., Saunders, D. E. & Ganesan, V. Surgical revascularisation for childhood moyamoya. *Childs. Nerv. Syst.* **28,** 1041–8 (2012).
42. The EC/IC Bypass Study Group. Failure of extracranial-intracranial arterial bypass to reduce the risk of ischemic stroke. Results of an international randomized trial. *N. Engl. J. Med.* **313,** 1191–200 (1985).
43. Powers, W. J. *et al.* Extracranial-Intracranial Bypass Surgery for Stroke Prevention in Hemodynamic Cerebral Ischemia. *JAMA* **306,** 1983 (2011).
44. Charbel, F. T. *et al.* A patient-specific computer model to predict outcomes of the balloon occlusion test. *J. Neurosurg.* **101,** 977–988 (2004).

2

Proximal and distal occlusion of complex cerebral aneurysms – implications of flow modelling by fluid structure interaction analysis

Authors:
Jasper H.G. Helthuis, MD[1,3]*, Sindhoor Bhat, MS[2]*,
Tristan P.C. van Doormaal, MD, PhD[1,3], Ramarathnam Krishna Kumar PhD[2],
Albert van der Zwan, MD, PhD[1,3]

Affiliations:
[1] Department of Neurosurgery, University Medical Center Utrecht, Utrecht, The Netherlands
[2] Department of Engineering Design, Indian Institute of Technology Madras, Chennai, India
[3] Brain Technology Institute, Utrecht, The Netherlands
* *Both authors contributed equally to the manuscript*

Status:
Operative Neurosurgery, 2018 Aug 1;15(2):217-230

Abstract

Background: In complex cerebral aneurysms adequate treatment by complete occlusion is not always possible. Partial occlusion by either proximal- or distal occlusion is an alternative. However, the hemodynamic consequences of these partial occlusion options are often not well predictable

Objective: To assess the feasibility of Fluid-Structure Interaction (FSI) analysis to investigate the hemodynamic changes after partial occlusion in cerebral aneurysms.

Methods: Two patients were analysed. One was treated by proximal occlusion and one by distal occlusion. In both flow-replacement bypass-surgery was performed. Three-dimensional models were constructed from magnetic resonance angiography (MRA) scans and used for FSI analysis. A comparative study was done for pre- and postoperative conditions. Postoperative thrombosis was modelled and analysed for the distal occlusion. FSI results were compared to postoperative angiograms and CT-scans.

Results: Proximal occlusion resulted in reduction of velocity, wall shear stresses (WSS) and disappearance of helical flow patterns in the complete aneurysm. Distal occlusion showed a decrease of velocity and WSS in the dome of the aneurysm. Results were validated against postoperative CT-scans and angiograms at 1-, 7- and 9-months follow-up. Addition of thrombus to the distal occlusion model showed no change in velocities and luminal pressure, but resulted in decrease in wall tension.

Conclusion: This pilot study showed hemodynamic changes in two patients with proximal and distal occlusion of complex cerebral aneurysms. The FSI results were in in line with the follow-up CT-scans and angiograms and indicate the potential of FSI as a tool in patient-specific surgical interventions.

Introduction

Surgical intervention plays an important role in the treatment of complex cerebral aneurysms and forms a therapeutic challenge when endovascular treatment modalities are not safe options. Treatment options include: (a) direct vessel reconstruction, (b) completely occluding the aneurysms with/without flow replacement surgery, (c) partial occlusion with/without flow replacement surgery. Partial occlusion is performed by proximal- or distal occlusion.[1]

Partial occlusion is an indirect treatment method aimed at reducing hemodynamic stresses inside the aneurysm by inducing thrombosis.[2,3] The degree of occlusion in small aneurysms is correlated with success-rate of the treatment; hence, the degree of thrombosis in partial occluded complex aneurysms is expected to be related to successful outcome.[4] However as shown in limited case series, complete thrombosis of a complex aneurysm may not always be achieved after partial occlusion and it's not known if treatment will induce thrombosis.[3,5,6]

With recent advances in mathematics the flow dynamics inside an arterial system can be analysed noninvasively. Tools like Computational fluid dynamics (CFD) and Fluid-Structure Interaction (FSI) methods have been used by researchers for this purpose.[7–11] FSI is a numerical technique, solving physiological problems that involves mutual interaction of fluid and structure, whereas, in CFD only fluid dynamics is studied without considering its effects on structure and deformations. As blood flow is pulsatile and results in the movement of elastic arteries, it will further influence fluid flow. Though CFD can predict fluid dynamics closely, shear stresses are often overestimated and wall tension cannot be predicted using rigid arterial wall. Both being important parameters in aneurysm rupture prediction.[7,12]

Based on these points above, the current study is set out as a pilot study to access the feasibility of FSI as a tool in investigating hemodynamic changes and subsequent thrombus formation after partial occlusion in complex cerebral aneurysms.

Methods

Two patients were analysed using FSI to model hemodynamic changes after proximal and distal occlusion of complex cerebral aneurysms. As patient data in this retrospective analysis were fully anonymized institutional review board (IRB) approval and patient consent was not required by our institution.

Case 1 (proximal occlusion)

A 47 year-old female was referred with an incidentally found asymptomatic growing complex aneurysm of the left middle cerebral artery (MCA). Preoperative MRA (3T Time-of-flight MRI, voxel-size 0.5 x 0.5 x 0.5 mm, inter-slice thickness 0.5 mm) confirmed the presence of a giant irregular shaped fusiform aneurysm. Due to its size, the exact anatomical location of the aneurysm was not clear but was assumed to covered most of the left M1 branch including the M2 bifurcation (figure 1). Because of size and side branches emerging from the aneurysm, endovascular treatment was impossible. Microsurgical treatment by partial occlusion was considered. A bypass was constructed from the left external carotid artery to one of the M2 branches for flow replacement. Proximal occlusion of the MCA was performed. A postoperative CT-scan showed a patent bypass and filling of the aneurysm from the distal side. One-month postoperative angiogram scan showed an almost complete thrombosis of the aneurysm. Nine-months computed tomography angiography imaging (CTA) showed complete thrombosis and obliteration of the aneurysm with a patent bypass (figure 1).

Case 2 (distal occlusion)

A 54 year-old female was referred for an incidentally found asymptomatic growing complex cerebral aneurysm of the left MCA. A MRA (7T, T1w, voxel-size 0.2 x 0.2 x 0.2 mm, inter-slice thickness 0.4 mm) showed a large fusiform aneurysm. Again, due to its size, we assumed it covered the complete tract the left M2 branches incorporating a M3 bifurcation. Because of the size of the aneurysm and possible important branches emerging from the aneurysm, endovascular treatment was impossible. Microsurgical distal occlusion of the aneurysm was considered to be the safest option as the proximal side of the aneurysm was difficult to reach and would carry the risk of damaging flow to another M2 artery. A bypass from the superficial temporal artery to one of the M3 branches was constructed for flow replacement. Intraoperatively, however minimal flow (1-3 ml/min) was measured through the bypass using transonic flowmetry (Transonic Systems Inc. Ithaca, NY, USA) and temporary occlusion of the distal part of the aneurysm showed considerable backflow from leptomeningeal collaterals using

indocyanine green. However, this could not be quantified. Microsurgical clipping of distal branches of the aneurysm was performed. Immediate postoperative angiogram and long-term CT-scan (2 week and 7 months) showed a thrombosed bypass and thrombosis of only the dome portion of the aneurysm (figure 2).

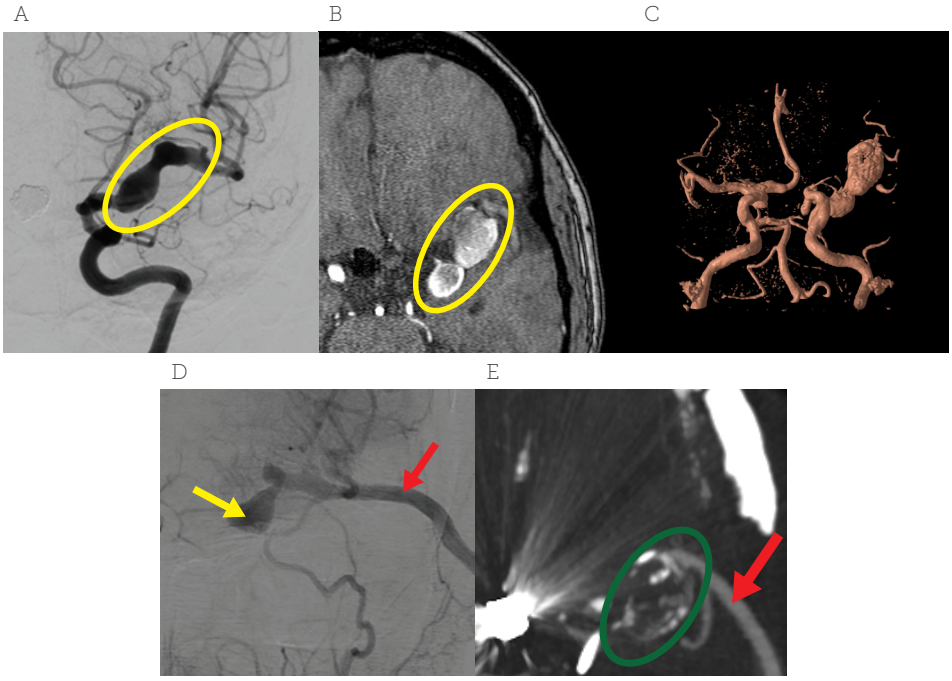

Figure 1: Complex giant aneurysm of case one.
A: preoperative angiogram. Yellow circle marks giant cerebral aneurysm. B: preoperative 3T time of flight MRA. Yellow circle marks gaint cerebral aneurysm. C: preoperative 3D reconstruction mased on 3T MRA D: postoperative angiogram at 1 month. Yellow arrow marks small section of aneursym, remaining part seems thrombosed. Red arrow marks bypass. E: Postoperative CTA at 9 months. Green circle marks area of thrombosis which seems to be the complete aneurysm including the small section which was initially remaining at 1 month postoperative. Red arrow marks bypass.

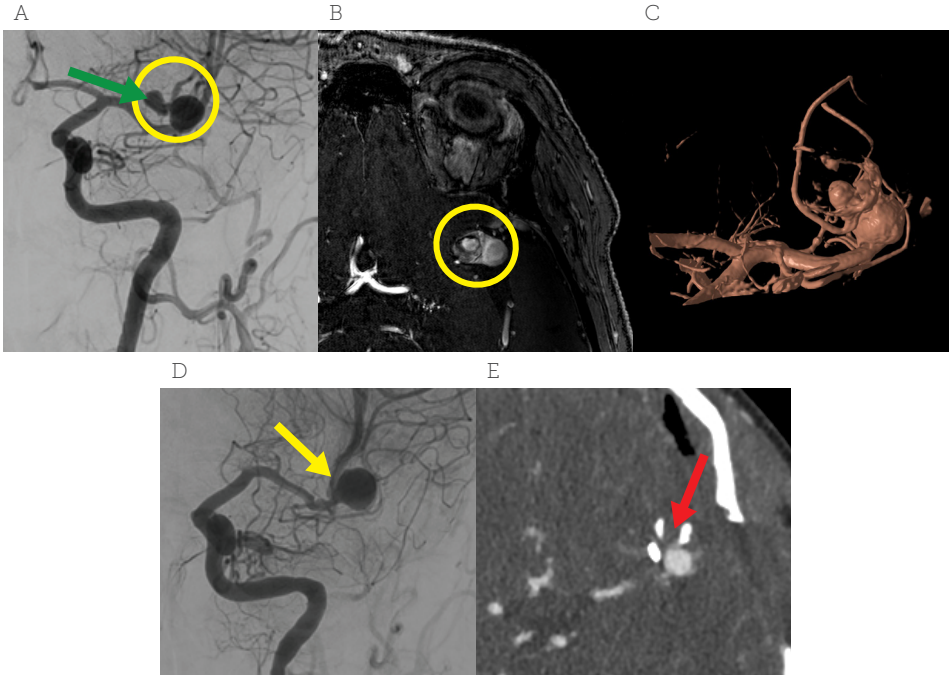

Figure 2: Complex giant aneurysm of case two.
A: preoperative angiogram. Yellow circle marks complex cerebral aneurysms. Green arrow marks apex of aneurysm. B: preoperative contrast enhanced 7T MRA. Yellow circle marks complex cerebral aneurysm. C: preoperative 3D reconstruction mased on 7T MRA. D: postoperative angiogram at 2 weeks. Yellow arrow marks location of thrombosed apex of aneurysm. E: Postoperative CTA at 7 months. Red arrow marks area of postoperative thrombosis which seems not to have changed since 2 weeks postoperative.

Fluid-Structure Interaction

A patient-specific 3D model was reconstructed from the MRA scans. The process followed is depicted in figure 3, with use of the Image Segmentation and Registration toolkit and Visualization toolkit (ITK version 4.6, VTK version 6.1, Kitware Inc., New York, NY, USA).

This 3D model was compared with the MRI-scan and angiogram data and found to be in good agreement. However the model (.stl format) generated cannot be used directly in FSI analysis as the mesh quality will not be adequate. Hence, further processing with surface generation and remeshing was required and performed using Hypermesh. (version 12, Altair Engineering Inc., Troy, MI, USA). An artery structure was meshed with two layers of brick elements and the fluid with tetrahedral elements. To relieve internal stresses in the model, zero pressure geometry was obtained by using the

procedure described by Raghavan et al.[13] This helps in applying boundary conditions. The results of 3D reconstruciton are shown in figure 4. For case two, to understand post-thrombosis effects and estimate probability of further thrombosis, an artificial thrombus was created in the dome of the aneurysm using tetrahedral elements in Hypermesh. Care was taken to visually match the size of this thrombosis as was seen on postoperative CT scan observations (Figure 2). FSI analysis was performed using dynamic implicit method in ADINA (version 9.1, DINA R&D Inc., Watertown, MA, USA). Blood was modelled as Carreau fluid.[14] Aneurysm wall, thrombus and internal carotid arteries were modeled using non-linear hyperelastic Mooney-Rivlin material.[7,15,16] The remaining arteries are considered to be linear elastic with a Young's modulus of 1.6 MPa. Thickness of artery and aneurysm wall were based on measurements in literature.[17–20]

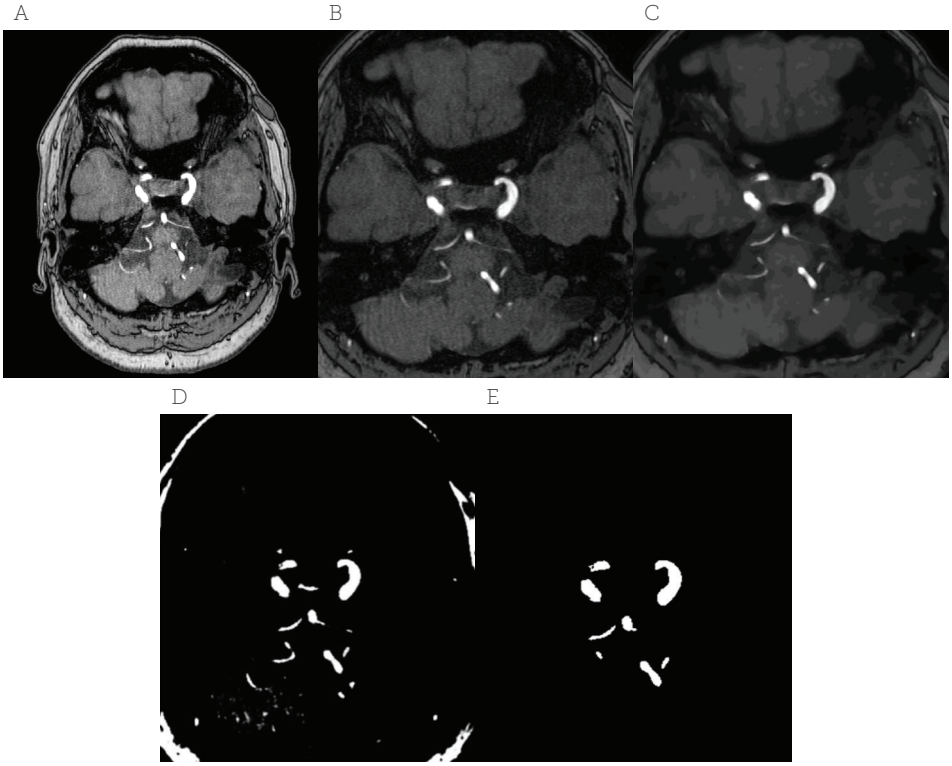

Figure 3: Stages involved in cerebral artery 3D reconstruction
(a) Full image (b) Region of Interest (c) Smoothing (d) Sigmoid image (e) Geodesic active contour segmentation

Boundary conditions for the 3D FSI model were obtained from a 0-D multicompartment electrical lumped parameter model, which was modeled for the complete human systemic arterieal tree using Simulink 2012b (version 8.0, The MathWorks Inc., Natick, Ma, USA).[19] Electrical parameters were calculated based on literature.[19] A detailed review on these models is given by Shi et al.[21] To model aneurysms in the 0D-model, polynomial fitting approach was used similar to Weber et al.[22]

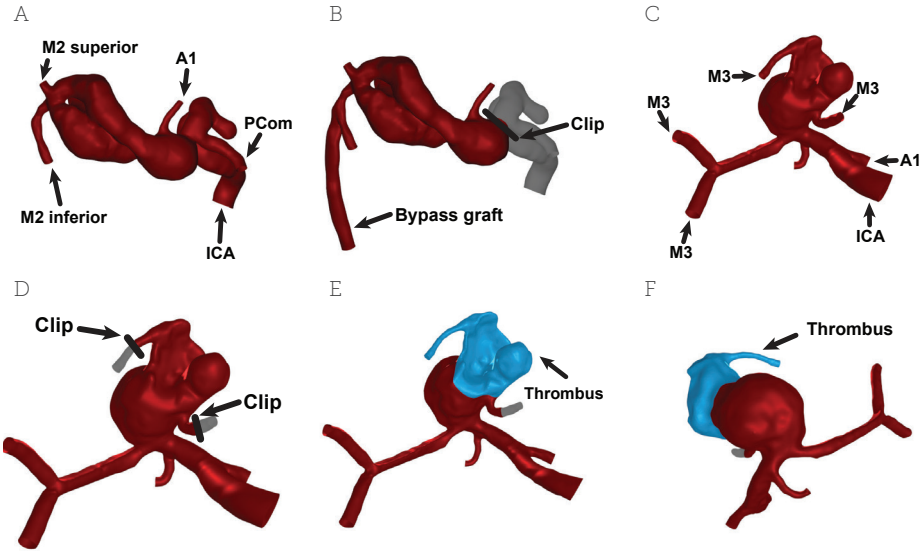

Figure 4: 3D reconstruction of case one and two.
A = case one: preoperative. B = case one: postoperative C = case two: preoperative D = case two: postoperative. E = case two: with thrombus. F = case two: with thrombus.

To obtain a realistic range of pressures as outlet boundary conditions to the 3D model, the pressure differentials obtained from the 0D-model were subtracted from the reference aortic pressure curve taken from Alaustrey et al.[20] Cardiac output was assumed as 5 L/min for both cases. Flow rate at the inlet of ICA was measured from the 0D model and the respective calculated velocity was prescribed as inlet boundary condition (figure 5).

Modelling brain matter and tissue support

To model external support by brain matter and cerebrospinal fluid, spring elements were generated using custom MATLAB 2012b (version 8, The MathWorks Inc., Natick, Ma, USA) code and attached to the external structural nodes in the 3D model.(Figure 6) Based on maximum radial displacement at peak systole in literature, the average spring stiffness was considered 1.5 N/m and stiffness based Rayleigh damping for aneurysm and thrombus structure was 0.0001.[18,22,23]

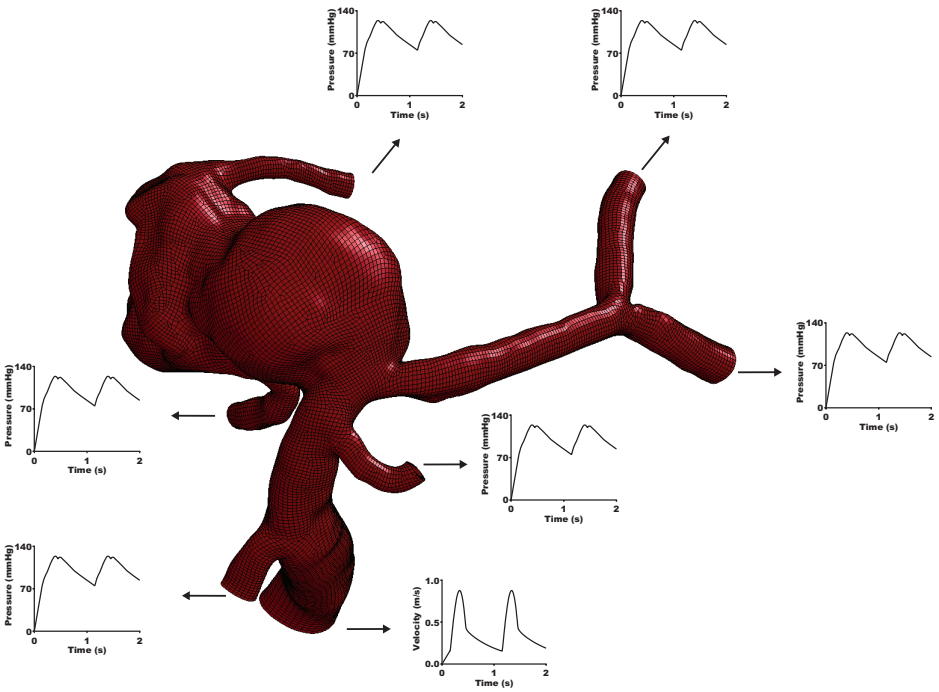

Figure 5: Inlet velocity (m/s) and outlet pressure (mmHg) boundary condition used in the Finite Element model for FSI analysis

Using FSI techniques, results were generated for: (a) velocity, (b) flow patterns using stream lines, (c) numerically injected particles in 3D model in FSI software were traced during 3 cardiac cycles, to understand stagnation. These in turn were used to show regions of stagnated flow and identify potential regions for thrombus region on postoperative CT-scans. (d) Wall shear stress (WSS), (e) maximum displacement, (f) luminal pressure distribution and (g) wall tension distribution (the stress due to stretching of the aneurysm wall), these all might be indicators of rupture risk.

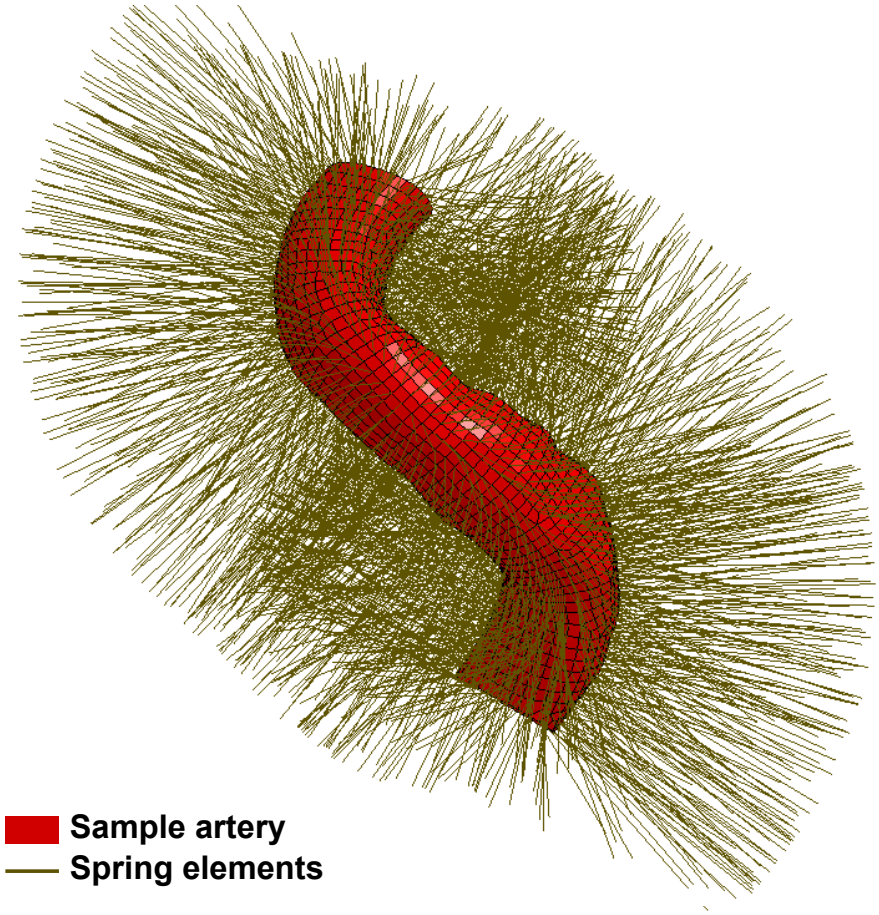

Figure 6: Sample section of artery in red with external spring elements (as green lines) acting as brain matter support. This is used in the finite element model for FSI.

Results

Table 1 summarizes the main results. See also video, supplemental digital content available at https://doi.org/10.1093/ons/opx236, which shows particle tracings pre- and postoperative for both cases.

Case 1 (proximal occlusion)

Stagnation region & thrombosis

Preoperative peak flow velocity in the aneurysm was 0.25 m/s which reduced to 0.05 m/s postoperatively (Figure 7). The proximal side of the aneurysm showed lower velocities. Postoperative, nearly 23% of numerically injected particles was trapped inside the system compared to 7% particles preoperative (figure 8, supplemental video). Only a limited number of particles reaches the proximal side of the aneurysm postoperatively. WSS was lower than 1 N/m^2 in the aneurysm for both situations. A 1-month angiogram showed almost complete thrombosis. A CTA-scan at 9 months revealed complete thrombosis of aneurysm. This visually matched the stagnated flow in a large part of the aneurysm (figure 1).

Flow pattern

Preoperative Dean's vortex and helical flow patterns inside the aneurysm disappeared, with the appearance of a large recirculation zone (Figure 7).

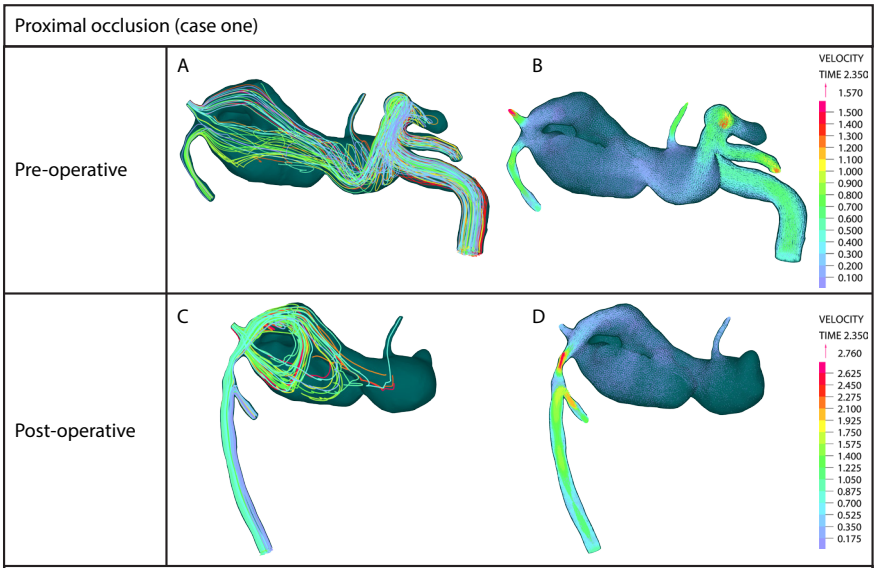

Figure 7: flow patterns and velocities of both case one and two.

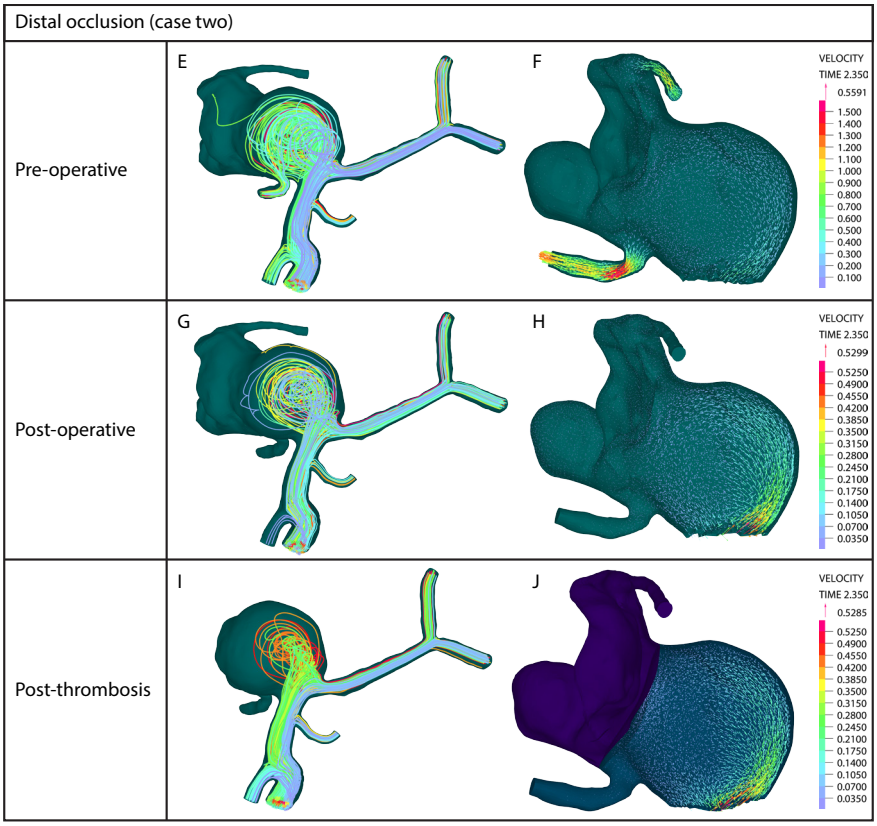

Figure 7: Continued.

Column one shows flow patterns and column two velocities in meters per seconds (m/s). The first two rows show preoperative and postoperative results of case one (proximal occlusion). The third, fourth and fifth rows show preoperative, postoperative results and results after thrombosis of case two (distal occlusion).

Displacement

Postoperative displacement showed a marginal increase from 0.57 mm to 0.59 mm (Figure 9).

Pressure distribution

Maximum pressure inside the aneurysm decreased from 17650 Pa to 16430 Pa after proximal occlusion (6.9% decrease) (Figure 9).

Wall tension

Maximum wall tension in the aneurysm increased from 2453323 N/m^2 to 2890706 N/m^2 (17.8%) postoperative (Figure 9).

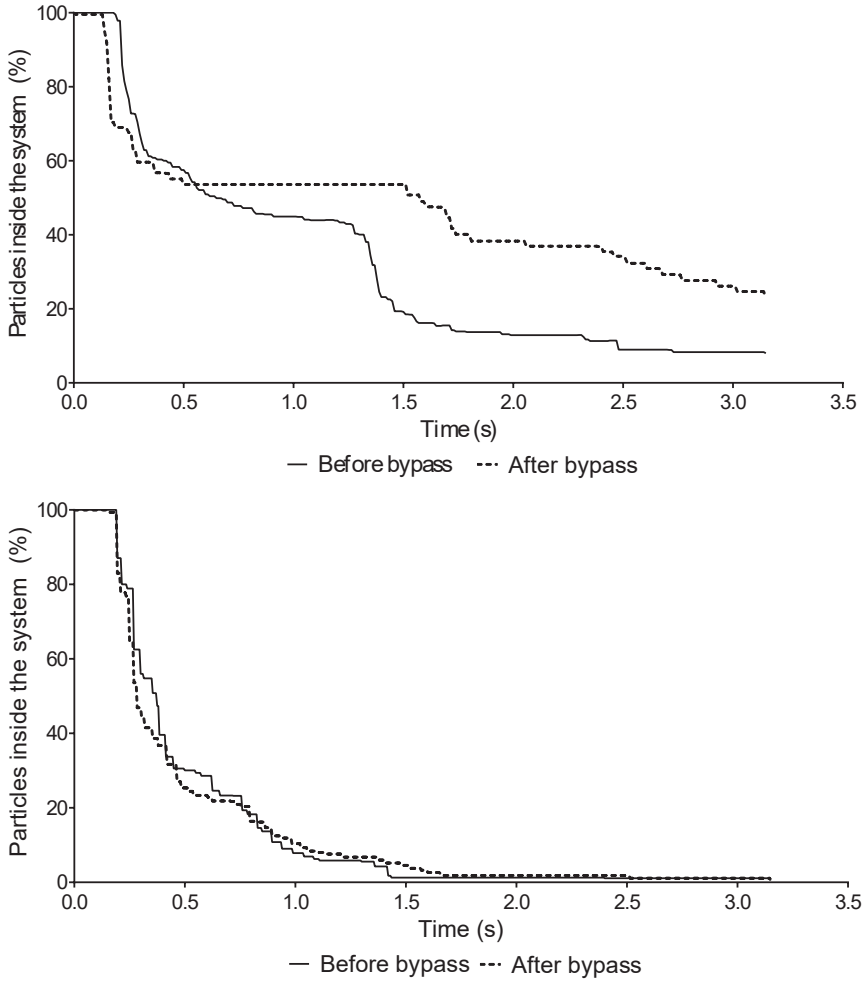

Figure 8: percentage particles left after particle tracing during 3 cardiac cycles (%). top: case one (proximal occlusion), bottom: case two (distal occlusion).

In conclusion, postoperative flow showed a change in flow pattern inside the aneurysm. Dean's vortices and helical flow that were seen preoperatively disappeared, with a distinct decrease in velocity and WSS creating stagnation zones. This stagnation is clearly seen using particle tracing during FSI analysis, that showed an increased percentage of particles trapped inside the aneurysm postoperatively. These observations show an increased potential of thrombosis and match well with postoperative angiograms and CT-scans which demonstrated a complete thrombosis of the aneurysm.

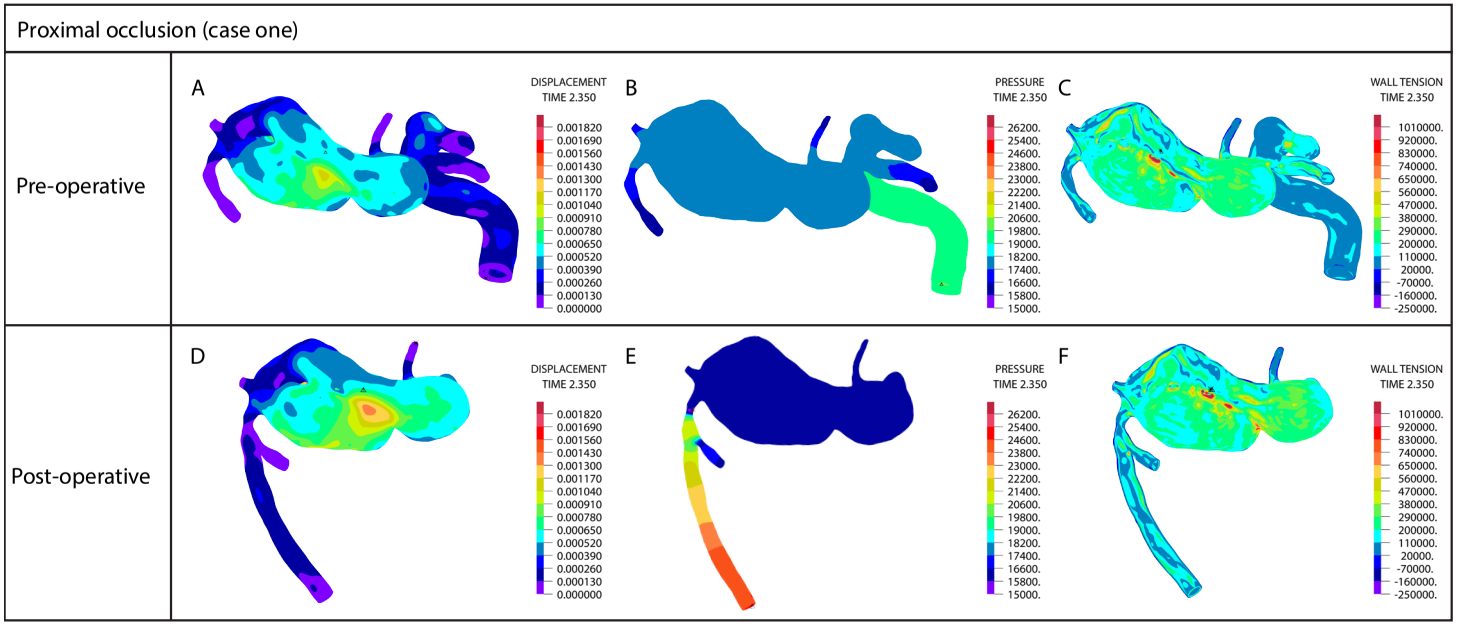

Figure 9: Displacement, pressure and wall tension for case one (proximal occlusion).

First row shows displacement in millimetres (mm), second row shows pressure in pascal (pa) and third row wall tension in newton per square metres (N/m^2). Results are shown for: first column shows preoperative and second column postoperative results.

Case 2 (distal occlusion)

Stagnation region & thrombosis

Velocity distribution for pre- and postoperative conditions are shown in Figure 7. For both pre- and postoperative all the numerically injected particles were washed away within 2 cardiac cycles (figure 8, supplemental video). In both situations the dome of the aneurysm showed velocities lesser than 0.03 m/s and WSS lesser than 0.4 N/m^2. After distal occlusion, a further decrease in velocity and WSS in the dome was observed. A two week follow-up angiogram revealed the development of thrombosis in the dome of aneurysm, which clearly matched the region of low velocities, WSS and particle tracing results (figure 2C). After modelling of thrombosis there was no change in velocities or WSS. A CT-scan at 7-months follow-up showed no further increase of thrombus size, which again visually matched FSI results.

Flow patterns

Complex flow pattern and vortices in several planes are visible in this aneurysm. Flow entering the aneurysm reaches certain height and recirculates back entering distal aneurysm branches. The flow pattern inside the aneurysm is helical in nature and is almost absent in the dome's top most region (Figure 7).

Displacement

Postoperative the maximum displacement increased from 0.43 mm to 0.50 mm at the dome of the aneurysm (16.3% increase). As the inlet flow reduces to 1.2 ml/s, displacement came down to 0.44 mm. After modelling of thrombosis, the location of maximum displacement shifted to the central bulge of the aneurysm and decreased to 0.22 mm (48.8% decrease) (Figure 10).

Pressure distribution

After distal occlusion, maximum pressure inside the aneurysm increased from 19500 Pa to 21560 Pa (10.6% increase). This pressure comes down to preoperative levels with the reduction of inlet flow to 1.2 ml/s. Modelling thrombosis showed negligible changes in the pressure distribution (Figure 10).

Wall tension

Maximum wall tension inside the aneurysm increased from 2209501 N/m^2 to 2530491 N/m^2 after clipping of M3 branches (14.5% increase) This reduces to preoperative level (2210668 N/m^2) with the reduction of inlet flow rate to 1.2 ml/s. Modelling thrombosis resulted in a decrease of maximum wall tension to 1571278 N/m^2 (28.9% decrease; Figure 10)

In conclusion, the flow pattern was helical in nature which reduces as it reaches the dome of the aneurysm. Although particle tracing in FSI showed no stagnation of particles inside the aneurysm, compared to the central region of the aneurysm the dome part had very low velocities and WSS with the absence of helical flow. This further diminished after distal occlusion and shows potential to thrombose the dome portion of the aneurysm. Postoperative angiogram and CT-scan showed thrombosis at the dome of the aneurysm. As shown after modelling of thrombosis, postoperative thrombosis had no effect on velocity and WSS in the remnant of the aneurysm, possibly indicating that further thrombosis was less likely to happen. These observations visually match well with FSI analysis.

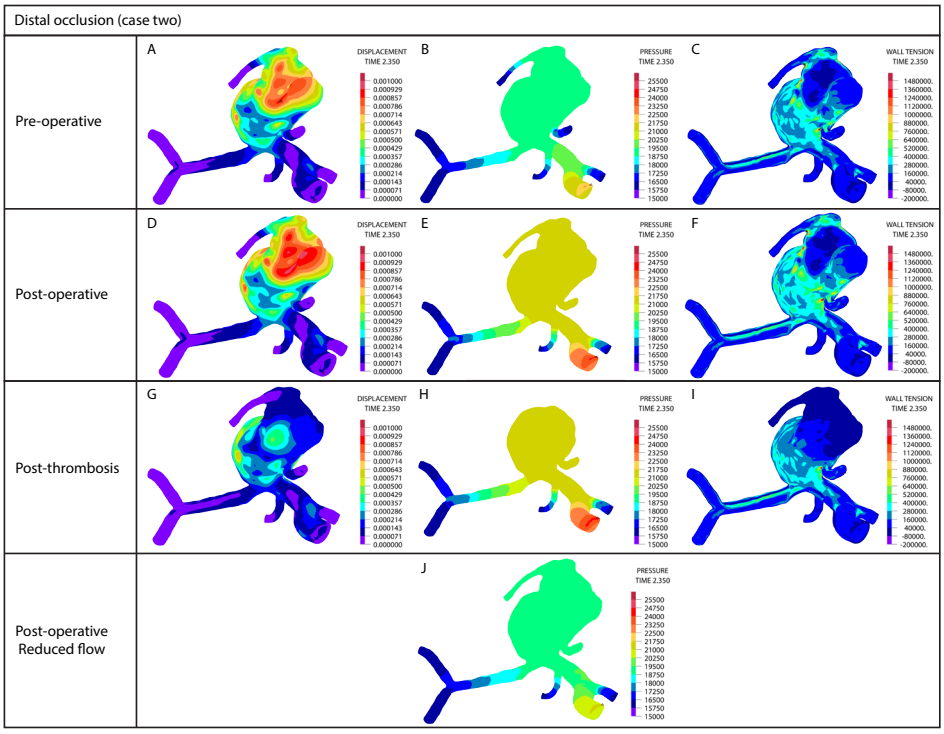

Figure 10: Displacement, pressure and wall tension for case two (distal occlusion).

First row shows displacement in millimetres (mm), second row shows pressure in pascal (pa) and third row wall tension in newton per square metres (N/m^2). Results are shown for: first column shows preoperative, second column postoperative, third column postoperative with thrombus and fourth column postoperative with reduced flow without thrombus.

	Maximum displacement (mm)	Maximum pressure (Pa)	Maximum wall tension (N/m^2)	Particles remaining after 3 cardiac cycles (%)
Proximal occlusion (case one)				
Pre-operative	0.57	17650	2453323	7
Post-operative	0.59	16430	2890706	23
Distal occlusion (case two)				
Pre-operative 1.6 ml/s inlet flow	0.43	19500	2209501	0
Post-operative 1.6 ml/s inlet flow	0.50	21560	2530491	0
Post-operative 1.2 ml/s inlet flow	0.44	19395	2210668	0
After thrombosis 1.6 ml/s inlet flow	0.22*	21490	1571278	0

Table 1: main results of both proximal (case one) and distal (case two) occlusions.

Pa: Pascal. mm: millimetres, N/m^2: Newton per square meters. m/s: meters per seconds. ml/s: millimetres per second. Values marked with a * are at the apex of the aneurysm. Remaining values are of the complete aneurysm.

Discussion

Partial occlusion is aimed at changing hemodynamic conditions to induce thrombosis and obliteration of the aneurysm. This is however not always successful.[3,5,6] Because hemodynamic changes in partial occlusion are not well understood and difficult to capture in an actual patient, it is difficult to clinically investigate whether partial occlusion in a patient will be successful.

In the current study, FSI analysis was used to understand the possible hemodynamic changes during partial occlusion, subsequent thrombus formation and post-thrombosis effects in complex intracerebral aneurysms. Other alternative techniques enable us to capture real time (current state) data of patients. However, tools like FSI give an added advantage in judging possible treatment choices, bypass locations and its outcome as it gives a clear picture of flow and structure dynamics.[11,24–26] This might be used for more patient-specific treatment choices in the future.

Aneurysm thrombosis is a complex process in which many factors are involved. It has been shown in several studies, that low-flow velocity zones and low WSS regions are prone to thrombosis.[27–30] Absence of a helical flow pattern is another parameter which promotes thrombus formation through plaque rupture.[30]

Postoperative thrombosis has an influence in reducing the rupture risk. In case of complete thrombosis, rupture risk is expected to be negligible. However, when the aneurysm not fully thrombosed rupture might still occur.[4]

Rupture risk is difficult to predict accurately as many factors are involved which also change over time. Besides eutrophic and destructive cellular processes and inflammatory responses, hemodynamic stresses are of importance.[31–35] One of these hemodynamic parameters which_might determine aneurysm rupture risk is wall tension.[9,36–38] The rupture risk is expected to increase when the wall tension exceeds the strength of wall tissue. However, as many factors are involved, the current study intents to estimate short term rupture risk. To understand this, thrombosis was modelled for the distal occlusion case.

With thrombosis, a shift in maximum displacement and wall tension, is seen from aneurysm apex to the central region. The cushioning effect of thrombus results in a decrease in wall tension and displacement. This might indicate a temporary decrease in rupture risk. Also, FSI shows no large change in flow patterns in case

two after partial thrombosis, highlighting that further thrombosis was not likely, as was confirmed by 7-months follow-up CTA.

Successful outcomes of partial occlusion are shown in multiple case series. Proximal occlusion was successful in 75 to 100% as reported by two studies.[3,5,39,40] Distal occlusion was successful in 50 to 100% as reported by 8 studies.[1,3,5,6,39–42] As stated before, in the current study only proximal occlusion resulted in complete thrombosis of the aneurysm. FSI was able to accurately describe this before surgery by showing decrease in WSS, velocity and stasis of traced particles in case one and no change in these parameters in case two after treatment.

Both proximal and distal occlusion resulted in an initial increase in wall tension. Increase in postoperative wall tension might indicate a temporary increase in rupture risk. In the proximal occlusion case, this might be explained by a pull force due to change in anatomy by addition of the bypass. In case of distal occlusion, the increase in wall tension is most likely caused by a temporal increase in luminal pressure.

According to Horowitz et al.[42] the changes of pressure on distal clipping will stay within normal daily variability, which varies between 10 and 25%.[43–47] Sudden increase in blood pressure related to increased physical activity induce even larger changes in blood pressure than the daily variability.[48] The increase of luminal pressure after distal occlusion shown in our FSI analysis is within this daily variability and might be considered safe. However, again as many factors influence rupture risk these predictions are highly patient-specific.

Also, after surgery it is expected that flow through the aneurysm decreases as the aneurysm will thrombose and the blood supply to the arteries distal from the clip will occur through collaterals or flow replacement surgery and not through the original feeding arteries. This reduced flow and with the formation of thrombus, a further decrease in wall stresses, displacement and possibly rupture risk might be observed.

In summary, both proximal and distal occlusion techniques can result in a short-term increase in wall tension, which could indicate an increase in immediate rupture risk. However, this is expected to be within daily variability and decreases to preoperative levels after expected reduction of blood flow and thrombosis, likely resulting in only a short temporary increased rupture risk.

Limitations and future scope

The current study has its limitations. Calcifications and other arteriosclerotic vessel wall changes are not accounted for, which might have an impact on arterial wall mechanics. Collateral flow and auto-regulatory responses are also not taken into consideration. Arterial wall thickness and parameters were taken from literature and not measured in the actual patients. Although this might affect the accuracy of the results, we believe this to be minimal. 3T- and 7T-MRI have differences in signal-to-noise ratio and in resolution. These differences combined with the human intervention needed in image pre-processing steps may impact the accuracy of the 3D model. However, with proper selection of image processing techniques and filter parameters, these errors can be reduced regardless if image acquisition method.

We have validated our study only using angiograms and CTA scans of the patient. Further validation using techniques such as 4D MRA, Particle Image Velocimetry for flow pattern and velocity measurements might improve results.

The most important limitation is that only two cases were analysed for the current study. As treatment of complex cerebral aneurysms is a highly patient-specific field, results might be different in other patients. However, this FSI analysis is a pilot study and has shown potential to evaluate complex cases. The entire process for analysing and predicting outcome takes 2 days which is stressful to use in clinic on a regular basis. For clinical feasibility, time optimization is required by building a GUI for image processing and automating mesh generation process. Also, more case studies with long-term follow up should be analysed to create a database for further validation of the method.

Conclusion

The predictions done by FSI analysis in this pilot study on hemodynamic changes in two patients were matching with what was observed on follow-up angiograms and CT-scans, potentially showing the feasibility of the current technique. Though the procedure followed in the current study is time consuming to be directly used in clinic, FSI is a potential tool for patient-specific interventions and future research studies on complex surgeries.

References

1. Esposito, G. & Regli, L. Surgical decision-making for managing complex intracranial aneurysms. *Acta Neurochir. Suppl.* **119,** 3–11 (2014).
2. Maldaner, N. *et al.* Changes in volume of giant intracranial aneurysms treated by surgical strategies other than direct clipping. *Acta Neurochir. (Wien).* **157,** 1117–1123 (2015).
3. Lee, S. H. *et al.* Surgical Flow Alteration for the Treatment of Intracranial Aneurysms That Are Unclippable, Untrappable, and Uncoilable. *J. Korean Neurosurg. Soc.* **58,** 518–527 (2015).
4. Johnston, S. C. *et al.* Predictors of rehemorrhage after treatment of ruptured intracranial aneurysms: the Cerebral Aneurysm Rerupture After Treatment (CARAT) study. *Stroke.* **39,** 120–125 (2008).
5. Kalani, M. Y., Zabramski, J. M., Nakaji, P. & Spetzler, R. F. Bypass and flow reduction for complex basilar and vertebrobasilar junction aneurysms. *Neurosurgery* **72,** 763–776 (2013).
6. Yoon, W. K., Jung, Y. J., Ahn, J. S. & Kwun, B. D. Successful obliteration of unclippable large and giant middle cerebral artery aneurysms following extracranial-intracranial bypass and distal clip application. *J. Korean Neurosurg. Soc.* **48,** 259–262 (2010).
7. Valencia, A. *et al.* Fluid structural analysis of human cerebral aneurysm using their own wall mechanical properties. *Comput. Math. Methods Med.* **2013,** 1–18 (2013).
8. Bazilevs, Y. *et al.* A fully-coupled fluid-structure interaction simulation of cerebral aneurysms. *Comput. Mech.* **46,** 3–16 (2010).
9. Isaksen, J. G. *et al.* Determination of wall tension in cerebral artery aneurysms by numerical simulation. *Stroke.* **39,** 3172–3178 (2008).
10. Rayz, V. L., Lawton, M. T., Martin, A. J., Young, W. L. & Saloner, D. Numerical simulation of pre- and postsurgical flow in a giant basilar aneurysm. *J. Biomech. Eng. ASME* **130,** (2008).
11. Bhat, S., Mathew, J., Balakrishnan, K. R. & Krishna Kumar, R. Effect of Outflow Graft Size on Flow in the Aortic Arch and Cerebral Blood Flow in Continuous Flow Pumps. *ASAIO J.* **63,** 144–149 (2017).
12. Bazilevs, Y., Gohean, J. R., Hughes, T. J. R., Moser, R. D. & Zhang, Y. Patient-specific isogeometric fluid–structure interaction analysis of thoracic aortic blood flow due to implantation of the Jarvik 2000 left ventricular assist device. *Comput. Methods Appl. Mech. Eng.* **198,** 3534–3550 (2009).
13. Raghavan, M. L., Ma, B. & Fillinger, M. F. Non-invasive determination of zero-pressure geometry of arterial aneurysms. *Ann. Biomed. Eng.* **34,** 1414–1419 (2006).
14. Razavi, A., Shirani, E. & Sadeghi, M. R. Numerical simulation of blood pulsatile flow in a stenosed carotid artery using different rheological models. *J. Biomech.* **44,** 2021–2030 (2011).
15. Creane, A. *et al.* Finite element modelling of diseased carotid bifurcations generated from in vivo computerised tomographic angiography. *Comput. Biol. Med.* **40,** 419–429 (2010).
16. Volokh, K. Y. Thrombus rupture via cavitation. *J. Biomech.* **48,** 2186–2188 (2015).
17. Sherif, C. *et al.* Evaluation of cerebral aneurysm wall thickness in experimental aneurysms: comparison of 3T-MR imaging with direct microscopic measurements. *Acta Neurochir. (Wien).* **156,** 27–34 (2014).
18. Takizawa, K., Christopher, J., Tezduyar, T. E. & Sathe, S. Space-time finite element computation of arterial fluid-structure interactions with patient-specific data. *Int. j. numer. method. biomed. eng.* **26,** 101–116 (2010).

19. Reymond, P., Merenda, F., Perren, F., Rüfenacht, D. & Stergiopulos, N. Validation of a one-dimensional model of the systemic arterial tree. *Am. J. Physiol. Heart Circ. Physiol.* **297,** H208-222 (2009).
20. Alastruey, J., Parker, K. H., Peiró, J., Byrd, S. M. & Sherwin, S. J. Modelling the circle of Willis to assess the effects of anatomical variations and occlusions on cerebral flows. *J. Biomech.* **40,** 1794–1805 (2007).
21. Shi, Y., Lawford, P. & Hose, R. Review of zero-D and 1-D models of blood flow in the cardiovascular system. *Biomed. Eng. Online* **10,** 1–38 (2011).
22. Weber, T. F. *et al.* True four-dimensional analysis of thoracic aortic displacement and distension using model-based segmentation of computed tomography angiography. *Int. J. Cardiovasc. Imaging* **30,** 185–194 (2014).
23. Soleimani, E., Dizaji, M. M. & Saberi, H. Carotid Artery Wall Motion Estimation from Consecutive Ultrasonic Images: Comparison between Block-Matching and Maximum-Gradient Algorithms. *J. Tehran Heart Cent.* **6,** 72–78 (2011).
24. Tsang, A. C. O. *et al.* Blood flow in intracranial aneurysms treated with Pipeline embolization devices: computational simulation and verification with Doppler ultrasonography on phantom models. *Ultrason. (Seoul, Korea)* **34,** 98–108 (2015).
25. Tenjin, H. *et al.* Evaluation of intraaneurysmal blood velocity by time-density curve analysis and digital subtraction angiography. *AJNR. Am. J. Neuroradiol.* **19,** 1303–7 (1998).
26. Satoh, T., Onoda, K. & Tsuchimoto, S. Visualization of intraaneurysmal flow patterns with transluminal flow images of 3D MR angiograms in conjunction with aneurysmal configurations. *AJNR. Am. J. Neuroradiol.* **24,** 1436–45 (2003).
27. Bluestein, D., Niu, L., Schoephoerster, R. T. & Dewanjee, M. K. Steady flow in an aneurysm model: correlation between fluid dynamics and blood platelet deposition. *J. Biomech. Eng.* **118,** 280–286 (1996).
28. Wootton, D. M. & Ku, D. N. Fluid mechanics of vascular systems, diseases, and thrombosis. *Annu. Rev. Biomed. Eng.* **1,** 299–329 (1999).
29. Sughrue, M. E., Saloner, D., Rayz, V. L. & Lawton, M. T. Giant intracranial aneurysms: evolution of management in a contemporary surgical series. *Neurosurgery* **69,** 1261–1270 (2011).
30. Liu, X. *et al.* A numerical study on the flow of blood and the transport of LDL in the human aorta: the physiological significance of the helical flow in the aortic arch. *Am. J. Physiol. Heart Circ. Physiol.* **297,** H163-170 (2009).
31. Chow, M. *et al.* Delayed spontaneous rupture of a posterior inferior cerebellar artery aneurysm following treatment with flow diversion: a clinicopathologic study. *AJNR. Am. J. Neuroradiol.* **33,** E46-51 (2012).
32. Frösen, J. *et al.* Saccular intracranial aneurysm: pathology and mechanisms. *Acta Neuropathol.* **123,** 773–786 (2012).
33. Frösen, J. *et al.* Remodeling of saccular cerebral artery aneurysm wall is associated with rupture: histological analysis of 24 unruptured and 42 ruptured cases. *Stroke.* **35,** 2287–2293 (2004).
34. Meng, H., Tutino, V. M., Xiang, J. & Siddiqui, A. High WSS or low WSS? Complex interactions of hemodynamics with intracranial aneurysm initiation, growth, and rupture: toward a unifying hypothesis. *AJNR. Am. J. Neuroradiol.* **35,** 1254–1262 (2014).
35. Sun, N. *et al.* Computational analysis of oxygen transport in a patient-specific model of abdominal aortic aneurysm with intraluminal thrombus. *Br. J. Radiol.* **82,** S18-23 (2009).

36. Fillinger, M. F., Marra, S. P., Raghavan, M. L. & Kennedy, F. E. Prediction of rupture risk in abdominal aortic aneurysm during observation: wall stress versus diameter. *J. Vasc. Surg.* **37,** 724–732 (2003).
37. Hall, A. J., Busse, E. F., McCarville, D. J. & Burgess, J. J. Aortic wall tension as a predictive factor for abdominal aortic aneurysm rupture: improving the selection of patients for abdominal aortic aneurysm repair. *Ann. Vasc. Surg.* **14,** 152–157 (2000).
38. Venkatasubramaniam, A. K. *et al.* A comparative study of aortic wall stress using finite element analysis for ruptured and non-ruptured abdominal aortic aneurysms. *Eur. J. Vasc. Endovasc. Surg.* **28,** 168–176 (2004).
39. Kivipelto, L. *et al.* Bypass surgery for complex middle cerebral artery aneurysms: impact of the exact location in the MCA tree. *J. Neurosurg.* **120,** 398–408 (2014).
40. Kalani, M. Y. S. *et al.* Revascularization and Aneurysm Surgery. *Neurosurgery* **74,** 482–498 (2014).
41. Esposito, G., Fierstra, J. & Regli, L. Distal outflow occlusion with bypass revascularization: last resort measure in managing complex MCA and PICA aneurysms. *Acta Neurochir. (Wien).* **158,** 1523–31 (2016).
42. Horowitz, M. B., Yonas, H., Jungreis, C. & Hung, T. K. Management of a giant middle cerebral artery fusiform serpentine aneurysm with distal clip application and retrograde thrombosis: case report and review of the literature. *Surg. Neurol.* **41,** 221–225 (1994).
43. Degaute, J. P., van de Borne, P., Linkowski, P. & Van Cauter, E. Quantitative analysis of the 24-hour blood pressure and heart rate patterns in young men. *Hypertension* **18,** 199–210 (1991).
44. Drayer, J. I., Weber, M. A., DeYoung, J. L. & Wyle, F. A. Circadian blood pressure patterns in ambulatory hypertensive patients: effects of age. *Am. J. Med.* **73,** 493–499 (1982).
45. Weber, M. A., Drayer, J. I., Nakamura, D. K. & Wyle, F. A. The circadian blood pressure pattern in ambulatory normal subjects. *Am. J. Cardiol.* **54,** 115–119 (1984).
46. Hermida, R. C. *et al.* Circadian rhythm of double (rate-pressure) product in healthy normotensive young subjects. *Chronobiol. Int.* **18,** 475–489 (2001).
47. Ogoh, S. *et al.* Middle cerebral artery flow velocity and pulse pressure during dynamic exercise in humans. *Am. J. Physiol. Heart Circ. Physiol.* **288,** H1526-1531 (2005).
48. Filipovský, J., Ducimetière, P. & Safar, M. E. Prognostic significance of exercise blood pressure and heart rate in middle-aged men. *Hypertension* **20,** 333–339 (1992).

3

Challenges in cerebral arterial blood flow modelling: a narrative review

Authors:
J.H.G.Helthuis, MD, MSc.[1,2], T.P.C. van Doormaal, MD, PhD[1,2], B. Hillen, MD, PhD[3], A. van der Zwan, MD, PhD[1,2]

Affiliations:
[1] University Medical Center Utrecht, Brain Center Rudolph Magnus, Department of neurosurgery, Utrecht, The Netherlands
[2] Brain Technology Institute, Utrecht, The Netherlands
[3] Department of Anatomy, University Medical Centre Nijmegen, Nijmegen, The Netherlands

Status:
Manuscript in preparation

Abstract

There is a lack of patient-specific, clinically applicable mathematical flow models of the cerebral arterial circulation. These patient-specific model could proof useful in clinical decision making, prevent invasive diagnostics and aid research in neurovascular diseases.

The current narrative review provides an up-to-date overview of challenges in development of such a model. The scope of the review is limited to zero-, one- and two-dimensional models. However, many aspects presented will also be of importance for three-dimensional blood flow modelling.

An overview is given of the impact that simplifications in hemodynamic properties (e.g. elastic vs. rigid arteries) might have on the accuracy. Methods for acquisition of patient-specific anatomical description of the larger cerebral arteries are presented. Problems and methods for both proximal and distal boundary conditions are named. Finally, the importance of autoregulation and collateral circulation is described.

Introduction

Background

Since long the human haemodynamic circulation has been of great interest to many scientists. Ranging from physicians searching for causes of certain diseases to mathematicians finding interest in the general description of blood flow through the arterial system. Probably the earliest work describing the mathematic principles of blood flow is that of Leonhard Euler in his work "Principia pro motu sanguinis per arterias determinando", which he most likely submitted in the year 1742 to the academy of sciences in Dijon, France. Euler described a one-dimensional (1D) set of equations based on conservation of mass and momentum.[1]

Following the work of Euler many other authors have contributed to the further understanding of the mathematical description of blood flow through the arterial system. Based on the general mathematical descriptions of fluid (blood) as described by Thomas Young, Poiseuille, Navier and Stokes, many haemodynamic models have been produced throughout history. Ranging from simple zero-dimensional (0D) single artery models, complete complex 1D models for the whole human circulation and three-dimensional (3D) models for aneurysmatic lesions and other pathological conditions.[2–6]

In medicine the use of computer aided techniques is gradually increasing. Higher computational capabilities make it possible to use more patient data and carve the road to better personalized medicine. Hemodynamic computer models could aid the physician in making correct medical decisions by predicting risks of treatment and of no treatment. Hereby invasive diagnostics can be reduced if computer models calculate either the current physiological sate of a patient or the likely outcome of treatment. Besides supporting treatment decisions, hemodynamic computer models could increase knowledge of many different complex vascular diseases. This could eventually lead to the development of new treatment techniques.

Aim and limitations of this narrative review

Despite the vast amount of studies that have been performed on cerebral blood flow modelling, to our knowledge a patient-specific computer model of the cerebral circulation has not been used in clinical practice. In this narrative review an overview will be given of problems which might impact the development of such a clinical applicable patient-specific cerebral blood flow model.

Methods currently used in literature for solving each problem will be presented. This will lead to an overview on how, a clinical applicable patient-specific model might be produced based on the current knowledge on cerebral blood flow modelling.

As shown in recent work, 3D modelling of the full cerebral circulation takes much computational time, even on current supercomputers.[7,8] This makes 3D models less feasible for use in current clinical decision making when most of the cerebral arterial circulation, or at least the full circle of Willis, has to be taken into account. 0D and 1D models are known for their less computational requirements. This makes them more suitable for development of clinically applicable models for easy and fast decision making. Additionally, 3D models require knowledge of difficult dedicated software while 0D and 1D models are more easy to implemented in current practice.[8]

To limit the scope of the current review, only zero-, one- and two-dimensional models are taken into account. However, many shortcomings and methods described in the current review will also be applicable to cerebral hemodynamic 3D flow models.

Methods

To collect information used in writing this narrative review, a search was performed on MEDLINE/PubMed, Scopus and Embase on 10th January 2019 using a Boolean combination of the following terms and their respective synonyms: *Cerebral* AND *flow* AND *mathematical model*.(see table 1 for search syntax) The database searches were limited to search only in title and abstract except for Web of Science which was searched in Topic. Duplicates where removed using Mendeley Desktop (Version 1.12.4, Mendeley Ltd., London, United Kingdom). These studies were screened on title and abstract using the following inclusion criteria: (a) interest of paper must comprise computational mathematical zero-, one- or two-dimensional cerebral arterial blood flow modelling, (b) English or Dutch language, (c) all research designs are included except for conference abstracts if they did not describe their mathematical method, (d) human subjects. Incorporated studies and reviews where manually cross-referenced to identify additional relevant studies. Additional non-systematic searches were performed in case information in identified studies was lacking. The literature survey and identification of relevant studies were performed by author JH.

Results

A total of 9774 (Pubmed: 3909, Embase 5106, Scopus 5993) results of all three databases were combined. After removal of duplicates a total of 7951 studies remained. After selection on title and abstract we selected 194 potentially relevant studies. After full text reading a total of 49 studies were deemed relevant and incorporated in the current narrative review. (Supplemental A shows characteristics of these studies)

Database	Search syntax
MEDLINE/ PubMed	(Cerebral[TIAB] OR brain[TIAB] OR (Circle[TIAB] AND willis[TIAB]) OR cerebro[TIAB] OR cerebrovascular[TIAB] OR intracranial[TIAB]) AND (Flow[TIAB] OR fluid[TIAB] OR wave[TIAB] OR hemodynamics[TIAB] OR hemodynamic[TIAB] OR haemodynamical[TIAB] OR hemodynamical[TIAB] OR haemodynamics[TIAB] OR haemodynamic[TIAB] OR circulation[TIAB] OR pulse[TIAB] OR flux[TIAB]) AND (((mathematical[TIAB] OR computer[TIAB] OR computational[TIAB] OR numerical[TIAB] OR dimensional[TIAB] OR 1D[TIAB] OR 0D[TIAB] or 3D[TIAB]) AND (model[TIAB] OR modelling[TIAB] OR modeling[TIAB] OR simulation[TIAB] OR models[TIAB])) OR equation[TIAB] OR equations[TIAB] OR poiseuille[TIAB] OR navier[TIAB] OR stokes[TIAB])
Embase	(Cerebral:ti:ab OR brain:ti:ab OR (Circle:ti:ab AND willis:ti:ab) OR cerebro:ti:ab OR cerebrovascular:ti:ab OR intracranial:ti:ab) AND (Flow:ti:ab OR fluid:ti:ab OR wave:ti:ab OR hemodynamics:ti:ab OR hemodynamic:ti:ab OR haemodynamical:ti:ab OR hemodynamical:ti:ab OR haemodynamics:ti:ab OR haemodynamic:ti:ab OR circulation:ti:ab OR pulse:ti:ab OR flux:ti:ab) AND (((mathematical:ti:ab OR computer:ti:ab OR computational:ti:ab OR numerical:ti:ab OR dimensional:ti:ab OR 1D:ti:ab OR 0D:ti:ab or 3D:ti:ab) AND (model:ti:ab OR modelling:ti:ab OR modeling:ti:ab OR simulation:ti:ab OR models:ti:ab)) OR equation:ti:ab OR equations:ti:ab OR poiseuille:ti:ab OR navier:ti:ab OR stokes:ti:ab)
Scopus	(TITLE-ABS(Cerebral) OR TITLE-ABS(brain) OR (TITLE-ABS(Circle) AND TITLE-ABS(willis)) OR TITLE-ABS(cerebro) OR TITLE-ABS(cerebrovascular) OR TITLE-ABS(intracranial)) AND (TITLE-ABS(Flow) OR TITLE-ABS(fluid) OR TITLE-ABS(wave) OR TITLE-ABS(hemodynamics) OR TITLE-ABS(hemodynamic) OR TITLE-ABS(haemodynamical) OR TITLE-ABS(hemodynamical) OR TITLE-ABS(haemodynamics) OR TITLE-ABS(haemodynamic) OR TITLE-ABS(circulation) OR TITLE-ABS(pulse) OR TITLE-ABS(flux)) AND (((TITLE-ABS(mathematical) OR TITLE-ABS(computer) OR TITLE-ABS(numerical) OR TITLE-ABS(dimensional) OR TITLE-ABS(1D) OR TITLE-ABS(0D) OR TITLE-ABS(3D)) AND (TITLE-ABS(model) OR TITLE-ABS(modelling) OR TITLE-ABS(modeling) OR TITLE-ABS(simulation) OR TITLE-ABS(models))) OR TITLE-ABS(equation) OR TITLE-ABS(equations) OR TITLE-ABS(poiseuille) OR TITLE-ABS(navier) OR TITLE-ABS(stokes))

Table 1: search syntax for each database.

Discussion

When developing a cerebrovascular blood flow model a few aspects are of importance to achieve patient-specificity and required accuracy. These are discussed separately below.

Hemodynamic properties

The arterial circulation is a complex system in which there is interaction of many hemodynamic physiologic properties of both blood an arterial wall. These hemodynamic properties can be modelled to different magnitudes and can be governed using different equations. More comprehensive overviews of possible sets of equations governing the interaction between fluid and structure are available in many literature sources and books, hence the current review refrains from going in depth on this subject.[9–14]

Blood can be considered as a Newtonian or non-Newtonian fluid. In literature only one study based on a 1D model assumes non-Newtonian properties of blood flow.[15] Almost all other available 1D cerebral blood flow models assume Newtonian properties. Blood is known to behave non-Newtonian, however with shear rate values above 100 $s^{-1,}$ especially for 1D flow models, the change in viscosity becomes negligible and blood can be considered Newtonian.[9] This is the case in the non-capillary cerebral circulation. As shown by Razavi et al.[16] in 3D flow modelling in a healthy control case there is no relevant difference when utilizing Newtonian or non-Newtonian properties for blood. However, when modelling diseases such as vascular stenosis, non-Newtonian properties might have an effect relevant to mostly 3D models in case accurate results are needed.[17,18]

Further, blood is known to be compressible.[19] However, to our knowledge all 1D models published in literature assume blood to be incompressible, reducing complexity of the model. There are no adequate studies comparing the effects of assuming blood to be incompressible.

Many 1D models are further simplified and assume arterial wall to be non-elastic.[20–26] This results most often in the use of Hagen-Poiseuille equations.[9,27] The main advantage of this simplification is the resulting linear set of equations which are fast and easy to solve. However, only little data is known on the actual drop in accuracy by the assumptions made in the Hagen-Poiseuille equations. Hillen et al. compared a 1D model including pulsatile flow and elastic arterial walls with a model based on the Hagen-Poiseuille equations, and found a difference in calculated flow of 7,6-9.3%.[22,28] If for example a stenosis or aneurysm is modelled, these differences might increase.

Grinberg et al.[8] compared a 3D model to a 1D model with and without elastic properties. When neglecting elasticity of arterial wall, the 1D and 3D model showed a good agreement. Introduction of elasticity in the 3D model resulted in a discrepancy in the amplitude of flowrate and pressure oscillations during a cardiac cycle, however the time-averaged flowrate and pressure drop were found to be in good agreement. Their sensitivity analysis showed that with regards of flowrates and mean pressure a 25% difference in elasticity parameters resulted in a difference of about 4%, confirming relatively low effects of elasticity.[8]

These results show that that simplification of a model does not necessary result in a large drop in accuracy regarding volumetric flow rates. The choices for simplification should depend on the intended clinical usage case. When pressure fluctuations, flow patterns and wall stresses are of importance in for example a cerebral aneurysm rupture prediction model, a 3D model with adequate elastic properties is required. When less accuracy is needed a 0D or 1D flow model with elastic arteries or probably even a set of equations according to the Hagen-Poiseuille's equations might suffice.

Anatomical description

Many studies in literature utilize a standard dataset of the human cerebral arterial anatomy, previously acquired by other authors.[22,28–32] These datasets are good for testing purposes during a development phase. However, from the initial development of a model, one has to keep in mind how the patient's anatomical morphology will be acquired and incorporated into the model to ensure applicability in a patient-specific clinical situation.

Due to the easily accessible nature of published datasets, few authors utilize actual patient data in cerebral blood flow models.[4,8,23,24,33–42] The authors which do so most often acquire morphological data by using magnetic resonance angiography (MRA) techniques.[4,8,25,34,35,39,42,43] Limited numbers authors also utilize 3D digital rotational angiography (3DRA)[23,43] or computed tomography angiography (CTA)[41].

3DRA is known to depict more detail then other imaging techniques which should results in a more correct model. Another advantage of 3DRA is that only vascular lumina are shown. However due its invasiveness, catheterisation for 3DRA is less often used and less feasible for final use in clinic.[44] Additionally 3DRA is known to be sensitive for inhomogeneity in contrast-agent.[45]

CTA is known to be problematic when arteries of interest are close to bone as the intensity values of bone and contrast agent will overlap.[44,45] However, MRI is more sensitive to the chosen protocol as different scanning parameters might lead to an increase or decrease in size of arteries and there might be loss of signal in case of turbulent or disturbed flow in especially large aneurysms.[45] Limited studies have tried to estimate differences in accuracy of 3DRA, CTA and MRA for use in 3D fluid dynamics.[44–48] In some studies measurements are performed using a phantom model of an intra-cranial aneurysm[46–48], while others acquired in-vivo data.[44,45,47] Most authors conclude 3DRA to be the superior technique in term of accuracy for this purpose.[44,46–48] Results on CTA or MRA are mixed but show that both techniques are feasible and mainly limited by the acquired resolution. Surface reconstruction errors are mostly within the range of 1 voxel size.[44–48]

Hence, in most cases due to easy accessibility, lower costs and patient-risks, CTA and MRA are the preferred method to acquire patient-specific morphology.

Proximal boundary conditions

The proximal boundary conditions, which are the input to the cerebral blood flow model, are often easier to acquire than the distal boundary conditions (see below). Most often velocity, flow and pressure or a combination of these are used as proximal boundary conditions. Additionally, these values can be considered as static or pulsatile in nature. Many models published in literature utilize a standard dataset for their models' input, which is off-course not patient-specific.[15,21,22,24,25,27,28,31,33,36,40,41,49–68] Other capture actual patient-specific data.[5,8,23,26,29,34,37,39–43,57,69–72]

Phase-contrast MRA (PC-MRA) and Doppler ultrasound are the most prevalent techniques for capturing proximal boundary conditions.[5,23,34,35,39–42,57,69,70,72,73] Both techniques capture information on the velocity of blood. Combined with the cross-sectional area of the artery a volumetric flow rate can be calculated. This cross-sectional area can be acquired during the same imaging session as when performing the velocity measurements. An advantage of PC-MRA is that it will return a 2D velocity map for an artery, which might aid in 3D flow modelling as it results in a realistic velocity profile as input. Also, in the same imaging session of PC-MRA an MRA can be performed to acquire information on the patient's arterial morphology (see above).

Pressure cannot be captured using these methods and is most often measured using a finger blood pressure monitor or intra-arterial per-operative blood pressure measurement, which both can capture the pulsatility of the blood pressure.[26,49,71] By performing a pressure cuff artery blood pressure measurement information on the

systolic and diastolic pressure is acquired, which can be used to calculate a mean arterial pressure (MAP) or can be converted to a pulsatile pressure when combined with a standard pressure curve based on literature.[5,22,23,26,28,37,40,49,71–73]

When developing a mathematical flow model for the cerebral circulation, it is of importance to choose an adequate method of acquiring proximal boundary conditions before development starts. The availability of the acquisition method and the ease of usage, as well as required accuracy need to be kept in mind during this selection process. Doppler ultrasound of carotid arteries in the neck as well as a finger or radial artery blood pressure measurement are often cheap, safe and easily accessible which is ideal for less complex models, while PC-MRI might result in an increased accuracy.

Distal boundary conditions

As stated above an anatomical description of patient-specific morphology is most often acquired using CTA, MRA or 3DRA. The reconstruction of the distal side of the arterial tree is hampered as those arteries are in diameter well below the acquired voxel size of these imaging techniques. Hence, we cannot capture a patient-specific description of distal arteries. However, a large part of the cerebral resistance and flow changes are caused by distal arterioles and especially capillaries.[74,75] Additionally the brain is known to show a high variability in vascular territories.[76,77] Consequently, in a patient-specific cerebral blood flow model, the distal side of the arterial tree, while not being visualisable in the actual patient, is of major importance and highly variable between different subjects. For these reasons the distal boundary conditions applied to a model will often have the largest impact on the model's validity.

Most studies utilize a generic terminal resistance pattern often based on standard databases[4,27,31,33,34,52,60,66] or according to a set ratio[23,25,28,30,58,78,79] while placing a venous pressure behind these terminal resistances. This method however will not result in patient specific distal boundary conditions.

Few authors have tried to find more patient specific boundary conditions.[35,36,43,59,80,81] Charbel et al. described a sector model in which efferent arteries end in resistances for which the resistance is calculated using among others phase-contrast MR angiography (PC-MRA) measurements of actual subject.[43] Using their method they were able to produce a patient-specific model which in turn was used to accurately predict outcomes of a balloon occlusion test, confirming the model was able to adequately capture distal boundary conditions.

Roessler et al. used terminal resistances of which the resistance was estimated by calculating the total peripheral resistance, based on pressure difference between the MAP and central venous pressure and the mean total cerebral blood flow, and dividing this total resistance according to the ratio of the cross-sectional areas of all efferent arteries.[35]

Other methods rely on some form of generating the vasculature distally to larger efferent arteries. Salehi et al.[59] used a structured arterial tree approach. Using branching patterns of arterial trees terminal resistances are calculated based on the radius of efferent arteries. This method was initially described by Olufsen et al. for usage in the pulmonary arterial tree.[82] Other methods rely on automatic vessel growth algorithms in which certain constrains (e.g. a volume of interest, distance between arteries, microvascular density) are used to construct an optimized arterial tree is formed.[36,80,81]

In conclusion, to attain patient-specific boundary conditions only a limited number of methods are described so far. (a) usage of patient-specific blood flow measurements (such as PC-MRA), (b) a division of resistance according to cross-sectional area of efferent arteries, (c) structured trees based on branching patterns or more complex automatic vessel growth algorithms.[35,36,43,59,80,81]

Autoregulation

Despite the brain constituting to only 2% of the total body weight, it uses approximately 15% of the cardiac output. Blood flow to different regions of the brain is known to be variable in time and regulated by what is known as cerebral autoregulation. Changes in blood pressure ranging from 60mmHg to 150mmHg are largely corrected by this autoregulatory response leading to a generally unaltered total cerebral blood flow (CBF). When studying these effects there is a known static relationship between CBF and mean arterial pressure in which CBF is kept relatively constant. Additionally there are separate autoregulatory responses to dynamic changes as for example a sudden change in pressure and local changes in metabolism due to increased or decreases neuronal activity or disease.[13,83,84]

There are many different factors involved in this autoregulatory response. More important factors are nitric oxide (NO), carbondioxide (CO_2), Kalium (K^+), Hydrogen (H^+), adenosine, prostaglandins and different theories on neurovascular coupling. Recent studies also highlight the importance of capillary pericytes.[13,74,83,85–87] The relationship between many of these factors and the autoregulatory response are still not well understood but are outside the scope of the current review.

Due to the importance of autoregulation on cerebral blood flow, we expect that if a mathematical model needs to be clinical applicable some form of autoregulation needs to be incorporated. Roughly halve of current published cerebral arterial blood flow models incorporate some form of autoregulation, further highlighting it importance.[5,15,20,21,24–27,31,49–51,54–57,63,67–69,71–73,78,88,89]

Autoregulatory models most often describe an underlying response to some of the above mentioned metabolic or physiologic changes. A linear or non-linear relationship is used in which a physiological change leads to a change in most often peripheral resistances and/or capacitance. Changes in either blood pressure or flow are most often used as a triggering factor and should suffice in most clinical applicable models. Only a few studies utilizing a roughly linear change in resistance on pressure change.[57,68] We would advise to use a non-linear relationship for an autoregulatory response when possible as is done by most studies. This non-linear relationship should either be fitted to actual experimental patient data or based on theoretical assumptions in literature.[5,15,25,27,49,51,54–56,61–63,65,67,88,89]

Another often used method are proportional-integral (PI) controllers which try to keep blood flow in separate regions constant.[20,21,25,78] More complex models include neurogenic activity, changes in CO_2, oxygen saturation and other metabolic subsystems, but are less likely to be clinical applicable unless specific diseases are of interest.[31,50,64,69,72]

The choice of which physiological parameters and which autoregulatory response to use depends on the intended usage case of the cerebral arterial flow model, however most often a non-linear relationship between pressure and peripheral resistance or a PI controller should suffice. There is no data to accurately support which choice of non-linear relationship and assumptions are most accurate. If actual measurements of cerebral perfusion or autoregulation in patients will be used the chosen autoregulatory model needs to be tailored towards the selected measurement method.[84]

Collateral circulation

Cerebral collateral circulation can be divided in two separate parts, (a) the proximal side consisting of anastomosis within the circle of Willis and (b) more distal collateral pathways formed by leptomeningeal collateral arteries.[90]

A normal circle of Willis is present in case of a full arterial "circle" formed by both posterior cerebral arteries (P1 segments), both posterior communicating arteries, both anterior cerebral arteries (A1 segements) and an anterior communicating artery

(Acom). In these cases blood flow can easily communicate between the anterior blood supply through the internal carotid artery and posterior blood supply trough the basilar artery in direction of the inflow locations of all cerebral vascular territories. The ability of collateral flow through the circle of Willis is known to result in a lower prevalence of border zone cerebral infarctions in case of an ICA occlusion, showing its importance.[91]

Dispite being called the "normal" circle of Willis, only up to halve of the population is known to demonstrate a full circle of Willis.[91–94] Many variants exist with absence or duplication of parts of the circle of Willis. The differences in configuration of the circle of Willis will have a profound effect on directions of flow, making it of importance to most patient specific cerebral arterial blood flow modelling. However, as stated above in the section *Anatomical description* the morphology of the circle of Willis can most often be captured using 3DRA, CTA or MRA.

Distal collateral flow is formed by what are called leptomeningeal anastomoses. These are formed by pial arteries connecting between the cortical territories of 2 major cerebral arteries (e.g. the MCA and anterior cerebral artery (ACA)). The importance of these are highlighted by the profound difference in extend of infarction in ischemic events with occlusion of the MCA, ranging from almost complete perfusion to complete stroke of the vascular territory of the MCA.[95] Previous research suggests that the number of these leptomeningeal anastomosis are highly variable among different patients.[95]

As many of these collaterals are <1mm in diameter and often of the size closer to arterioles, current imaging techniques are not reliably able to capture these collaterals *in vivo*, hence indirect measurements are used. Conventional cerebral angiography is still considered the golden standard. This technique, as well as other imaging techniques used (e.g. dynamic computed tomography angiography dCTA), most often rely on dynamically studying the extend and rate of back-filling of arteries with blood, for example on dynamic images after contrast injection on angiography. Also specific MRI changes as for example vascular hyperintensities on fluid-attenuated inversion recovery MRI sequences, might be an indirect indication of presence of leptomeningeal collaterals.[90,95–97]

Whether leptomeningeal collaterals need to be added to a model to be patient-specific depends on the usage case of that specific model. However, acquiring adequate information on the presence or absence of leptomeningeal collaterals is only possible by indirect and often subjective measurements as stated above. This makes addition of patient specific leptomeningeal collateral to any cerebral arterial flow model difficult.

Due to this limitation up till today only one study has been able to adequately add leptomeningeal collateral flow to a cerebral blood flow model. Charbel et al. developed an 1D cerebral flow model with distal boundary conditions in sectors.[43] Leptomeningeal collaterals were added between these different sectors. Based on PC-MRI flow measurements in the larger cerebral arteries, cerebral perfusion based on ^{99}Tc-HMPAO SPECT scan and digital subtraction angiography of the cerebral circulation the resistances of these sectors and presence or absence of leptomeningeal collaterals were fitted. This model was in turn tested on 16 patients who underwent a balloon occlusion test to evaluate collateral circulation. Simulation of the same balloon occlusion test in the mathematical model resulted in a 100% sensitive and 100% specific test to identify patients who could not tolerate the balloon occlusion test, showing that the model was able to accurately predict the presence of leptomeningeal collaterals.[43]

In summary, the brain is known to have a collateral flow proximally at the level of the circle of Willis and distally due to leptomeningeal collateral anastomoses. The anatomy of the circle of Willis can easily be captured using current imaging techniques. Leptomeningeal collaterals are known to be highly variable. This variability can only be captured by indirect techniques. Hence up to today to the best of our knowledge only one cerebral blood flow model was able to incorporate patient specific leptomeningeal collateral circulation by fitting to flow measurements, perfusion measurements and anatomic description from digital subtraction angiography.[43]

Conclusion

This narrative review set out to draft an overview of challenges in the development of patient-specific cerebral arterial blood flow models feasible for usage in clinic. When developing such a model, assumptions have to me made regarding simplification of hemodynamic properties and arterial wall elasticity. These will have an effect on accuracy. It is of importance to acquire a patient-specific anatomical description using imaging techniques CTA and MRA are likely most feasible. Proximal boundary conditions are easy to acquire using pressure or velocity measurements. However, distal boundary conditions are more difficult as these are influenced by a high degree of variability, autoregulation and collateral circulation. Depending on the intended usage case of the model choices have to be made regarding all these aspects during the initial development phase.

References

1. Cerny, L. C. & Walawender, W. P. Leonhardi Euleri's "Principia pro motu sanguinis per arterias determinando". *J. Biol. Phys.* **2,** 41–56 (1974).
2. Young, T. The Croonian Lecture: On the Functions of the Heart and Arteries. *Philos. Trans. R. Soc. London* **99,** 1–31 (1809).
3. Sutera, S. P. & Skalak, R. The History of Poiseuille's Law. *Annu. Rev. Fluid Mech.* **25,** 1–20 (1993).
4. Reymond, P., Merenda, F., Perren, F., Rüfenacht, D. & Stergiopulos, N. Validation of a one-dimensional model of the systemic arterial tree. *Am. J. Physiol. Heart Circ. Physiol.* **297,** H208–H222 (2009).
5. Olufsen, M. S., Nadim, A. & Lipsitz, L. A. Dynamics of cerebral blood flow regulation explained using a lumped parameter model. *Am. J. Physiol. Regul. Integr. Comp. Physiol.* **282,** R611–R622 (2002).
6. Fillinger, M. F., Marra, S. P., Raghavan, M. L. & Kennedy, F. E. Prediction of rupture risk in abdominal aortic aneurysm during observation: wall stress versus diameter. *J. Vasc. Surg.* **37,** 724–32 (2003).
7. Grinberg, L., Anor, T., Madsen, J. R., Yakhot, A. & Karniadakis, G. E. Large-scale simulation of the human arterial tree. *Clin. Exp. Pharmacol. Physiol.* **36,** 194–205 (2009).
8. Grinberg, L., Cheever, E., Anor, T., Madsen, J. R. & Karniadakis, G. E. Modeling blood flow circulation in intracranial arterial networks: a comparative 3D/1D simulation study. *Ann. Biomed. Eng.* **39,** 297–309 (2011).
9. Nichils, W. W., O'Rourke, M. F. & Vlachopoulos, C. *McDonald's Blood Flow in Arteries. Theoretical, Experimental and Clinical Principles*. (Hodder Arnold, 2011).
10. Vosse, F. van de & Stergiopulos, N. Pulse wave propagation in the arterial tree. *Annu. Rev. Fluid Mech.* **43,** 467–499 (2011).
11. Cebral, J. R., Löhner, R. & Burgess, J. E. Computer simulation of cerebral artery clipping: Relevance to aneurysm neuro-surgery planning. in (2000).
12. Shi, Y., Lawford, P. & Hose, R. Review of zero-D and 1-D models of blood flow in the cardiovascular system. *Biomed. Eng. Online* **10,** 33 (2011).
13. David, T. & Moore, S. Modeling perfusion in the cerebral vasculature. *Med. Eng. Phys.* **30,** 1227–1245 (2008).
14. Moore, S. *et al.* 3D models of blood flow in the cerebral vasculature. *J. Biomech.* **39,** 1454–1463 (2006).
15. Pucher, R. K. & Auer, L. M. Effects of vasospasm in the middle cerebral artery territory on flow velocity and volume flow. A computersimulation. *Acta Neurochir. (Wien).* **93,** 123–128 (1988).
16. Razavi, S. E. & Sahebjam, R. Numerical simulation of the blood flow behavior in the circle of Willis. *BioImpacts* **4,** 89–94 (2014).
17. Razavi, A., Shirani, E. & Sadeghi, M. R. Numerical simulation of blood pulsatile flow in a stenosed carotid artery using different rheological models. *J. Biomech.* **44,** 2021–2030 (2011).
18. Carty, G., Chatpun, S. & Espino, D. M. Modeling Blood Flow Through Intracranial Aneurysms: A Comparison of Newtonian and Non-Newtonian Viscosity. *J. Med. Biol. Eng.* **36,** 396–409 (2016).
19. Wang, S. H., Lee, L. P. & Lee, J. S. A linear relation between the compressibility and density of blood. *J. Acoust. Soc. Am.* **109,** 390–6 (2001).

20. David, T., Brown, M. & Ferrandez, A. Auto-regulation and blood ow in the cerebral circulation. *Int. J. Numer. Methods Fluids* **713,** 701–713 (2003).
21. Ferrandez, A. *et al.* Numerical models of auto-regulation and blood flow in the cerebral circulation. *Comput. Methods Biomech. Biomed. Engin.* **5,** 7–20 (2002).
22. Hillen, B. *et al.* Analysis of flow and vascular resistance in a model of the circle of Willis. *J. Biomech.* **21,** 807–814 (1988).
23. Kailasnath, P. *et al.* Intracarotid pressure measurements in the evaluation of a computer model of the cerebral circulation. *Surg. Neurol.* **50,** 257–263 (1998).
24. Moorhead, K. T. *et al.* Metabolic model of autoregulation in the Circle of Willis. *J. Biomech. Eng.* **128,** 462–466 (2006).
25. Moorhead, K. T., Doran, C. V, Chase, J. G. & David, T. Lumped parameter and feedback control models of the auto-regulatory response in the circle of willis. *Comput. Methods Biomech. Biomed. Engin.* **7,** 121–130 (2004).
26. Panerai, R. B. *et al.* Linear and nonlinear analysis of human dynamic cerebral autoregulation. *Am. J. Physiol. - Hear. Circ. Physiol.* **277,** H1089–H1099 (1999).
27. Lodi, C. A. & Ursino, M. Hemodynamic effect of cerebral vasospasm in humans: a modeling study. *Ann. Biomed. Eng.* **27,** 257–273 (1999).
28. Hillen, B., Hoogstraten, H. W. & Post, L. A mathematical model of the flow in the circle of Willis. *J. Biomech.* **19,** 187–194 (1986).
29. Stergiopulos, N., Young, D. F. & Rogge, T. R. Computer simulation of arterial flow with applications to arterial and aortic stenoses. *J. Biomech.* **25,** 1477–88 (1992).
30. Ferrández, A., David, T., Bamford, J., Scott, J. & Guthrie, A. Computational models of blood flow in the circle of Willis. *Comput. Methods Biomech. Biomed. Engin.* **4,** 1–26 (2000).
31. Alastruey, J. *et al.* Reduced modelling of blood flow in the cerebral circulation: Coupling 1-D, 0-D and cerebral auto-regulation models. *Int. J. Numer. Methods Fluids* **56,** 1061–1067 (2008).
32. Blanco, P. J. *et al.* Computational modeling of blood flow steal phenomena caused by subclavian stenoses. *J. Biomech.* **49,** 1593–1600 (2016).
33. Müller, L. O. & Toro, E. F. A global multiscale mathematical model for the human circulation with emphasis on the venous system. *Int. j. numer. method. biomed. eng.* **30,** 681–725 (2014).
34. Reymond, P. *et al.* Patient-specific mean pressure drop in the systemic arterial tree, a comparison between 1-D and 3-D models. *J. Biomech.* **45,** 2499–2505 (2012).
35. Roessler, F. C., Reith, W. & Siegel, G. Simulation of cerebral hemodynamics for preoperative risk assessment. *Brain Res.* **1118,** 183–191 (2006).
36. Vaičaitis, N. M., Sweetman, B. J. & Linninger, A. A. A Computational Model of Cerebral Vasculature, Brain Tissue, and Cerebrospinal Fluid. *Computer Aided Chemical Engineering* **29,** 1530–1534 (2011).
37. Brosig, R. *et al.* Blood flow quantification using 1D CFD parameter identification. in *MEDICAL IMAGING 2014: IMAGE PROCESSING* (ed. Ourselin, S and Styner, M.) **9034,** 90342R (2014).
38. Charbel, F. *et al.* Neurovascular flow simulation review. *Neurol. Res.* **20,** 107–115 (1998).
39. DeVault, K. *et al.* Blood Flow in the Circle of Willis: Modeling and Calibration. *Multiscale Model. Simul.* **7,** 888–909 (2008).
40. Guanghong, D. *et al.* Hemodynamic model and mathematical method to calculate the dynamics index for cerebral circulation. *J. Hydrodyn.* **9,** 71–81 (1997).

41. Ho, H., Mithraratne, K., Schmid, H., Sands, G. & Hunter, P. Computer simulation of vertebral artery occlusion in endovascular procedures. *Int. J. Comput. Assist. Radiol. Surg.* **5,** 29–37 (2010).
42. Linninger, A. A. *et al.* A mathematical model of blood, cerebrospinal fluid and brain dynamics. *J. Math. Biol.* **59,** 729–759 (2009).
43. Charbel, F. T. *et al.* A patient-specific computer model to predict outcomes of the balloon occlusion test. *J. Neurosurg.* **101,** 977–988 (2004).
44. Geers, A. J. *et al.* Patient-specific computational hemodynamics of intracranial aneurysms from 3D rotational angiography and CT angiography: An in vivo reproducibility study. *Am. J. Neuroradiol.* **32,** 581–586 (2011).
45. Ren, Y. *et al.* Reproducibility of image-based computational models of intracranial aneurysm: A comparison between 3D rotational angiography, CT angiography and MR angiography. *Biomed. Eng. Online* **15,** 50 (2016).
46. Poethke, J. *et al.* in *4th European Conference of the International Federation for Medical and Biological Engineering* 1889–1893 (Springer, Berlin, Heidelberg, 2009). doi:10.1007/978-3-540-89208-3_450
47. Piotin, M. *et al.* CT angiography, MR angiography and rotational digital subtraction angiography for volumetric assessment of intracranial aneurysms. An experimental study. *Neuroradiology* **45,** 404–409 (2003).
48. Goubergrits, L. *et al.* Reproducibility of image-based analysis of cerebral aneurysm geometry and hemodynamics: An in-vitro study of magnetic resonance imaging, computed tomography, and three-dimensional rotational angiography. *J. Neurol. Surgery, Part A Cent. Eur. Neurosurg.* **74,** 294–302 (2013).
49. Aoi, M. C., Kelley, C. T., Novak, V. & Olufsen, M. S. Optimization of a Mathematical Model of Cerebral Autoregulation Using patient Data. in *Proceedings of 7th IFAC Symposium on Modelling and Control in Biomedical Systems* **7,** 6 pages (2010).
50. Banaji, M., Tachtsidis, I., Delpy, D. & Baigent, S. A physiological model of cerebral blood flow control. *Math. Biosci.* **194,** 125–173 (2005).
51. Bekker, A., Wolk, S., Turndorf, H., Kristol, D. & Ritter, A. Computer simulation of cerebrovascular circulation: assessment of intracranial hemodynamics during induction of anesthesia. *J. Clin. Monit.* **12,** 433–444 (1996).
52. Cassot, F. *et al.* Effects of anterior communicating artery diameter on cerebral hemodynamics in internal carotid artery disease: A model study. *Circulation* **92,** 3122–3131 (1995).
53. Fahy, P. *et al.* An experimental investigation of the hemodynamic variations due to aplastic vessels within three-dimensional phantom models of the circle of willis. *Ann. Biomed. Eng.* **42,** 123–138 (2014).
54. Gao, E. Z. *et al.* Mathematical considerations for modeling cerebral blood flow autoregulation to systemic arterial pressure. *Am. J. Physiol. - Hear. Circ. Physiol.* **274,** H1023–H1031 (1998).
55. Hoffmann, O. Biomathematics of intracranial CSF and haemodynamics. Simulation and analysis with the aid of a mathematical model. *Acta Neurochir. Suppl.* **40,** 117–130 (1987).
56. Moody, D. M., Santamore, W. P. & Bell, M. A. Does tortuosity in cerebral arterioles impair down-autoregulation in hypertensives and elderly normotensives? A hypothesis and computer model. *Clin. Neurosurg.* **37,** 372–387 (1991).
57. Ornstein, E. *et al.* A computer simulation of the haemodynamic effects of intracranial arteriovenous malformation occlusion. *Neurol. Res.* **16,** 345–352 (1994).

58. Papapanayotou, C. J., Cherruault, Y. & De La Rochefoucauld, B. A mathematical model of the circle of Willis in the presence of an arteriovenous anomaly. *Comput. Math. with Appl.* **20,** 199–206 (1990).
59. Salehi, S. S., Firoozabadi, B. & Saidi, M. S. Numerical and 1-D modeling of systemic circulation along with cerebral vasculature. in *2012 19th Iranian Conference of Biomedical Engineering (ICBME)* 17–21 (IEEE, 2012). doi:10.1109/ICBME.2012.6519652
60. Schwarz, M. *et al.* Integration of the Circle of Willis into Avolio's model of the arterial haemodynamics. in *6th IASTED International Conference on Biomedical Engineering, BioMED 2008* 193–198 (2008).
61. Ursino, M. A mathematical study of human intracranial hydrodynamics. Part 1 - The cerebrospinal fluid pulse pressure. *Ann. Biomed. Eng.* **16,** 379–401 (1988).
62. Ursino, M. & Digiammarco, P. A mathematical model of the relationship between cerebral blood volume and intracranial pressure changes: The generation of plateau waves. *Ann. Biomed. Eng.* **19,** 15–42 (1991).
63. Ursino, M. & Giulloni, M. Quantitative assessment of cerebral autoregulation from transcranial Doppler pulsatility: a computer simulation study. *Med. Eng. Phys.* **25,** 655–666 (2003).
64. Ursino, M. & Magosso, E. Role of tissue hypoxia in cerebrovascular regulation: A mathematical modeling study. *Ann. Biomed. Eng.* **29,** 563–574 (2001).
65. Ursino, M. A mathematical study of human intracranial hydrodynamics. Part 2 - Simulation of clinical tests. *Ann. Biomed. Eng.* **16,** 403–416 (1988).
66. Viedma, A., JimenezOrtiz, C. & Marco, V. Extended Willis circle model to explain clinical observations in periorbital arterial flow. *J. Biomech.* **30,** 265–272 (1997).
67. Wang, S. A Lumped Parameters Dynamic Model for Cerebral Circulation. in *APCMBE 2008: 7TH ASIAN-PACIFIC CONFERENCE ON MEDICAL AND BIOLOGICAL ENGINEERING* (ed. Peng, Y and Weng, X.) **19,** 147–150 (2008).
68. Zagzoule, M. & Marc-Vergnes, J. P. A global mathematical model of the cerebral circulation in man. *J. Biomech.* **19,** 1015–1022 (1986).
69. Connolly, M. *et al.* Reproduction of consistent pulse-waveform changes using a computational model of the cerebral circulatory system. *Med. Eng. Phys.* **36,** 354–63 (2014).
70. Ji, C. S., He, Y. & Liang, F. Y. A modeling study of blood flow and oxygen transport in the circle of Willis. in *3rd International Conference on Biomedical Engineering and Informatics* 1114–1118 (2010).
71. Payne, S. J. & Tarassenko, L. Combined transfer function analysis and modelling of cerebral autoregulation. *Ann. Biomed. Eng.* **34,** 847–858 (2006).
72. Spronck, B., Martens, E. G. H. J., Gommer, E. D. & van de Vosse, F. N. A lumped parameter model of cerebral blood flow control combining cerebral autoregulation and neurovascular coupling. *AJP: Heart and Circulatory Physiology* **303,** H1143–H1153 (2012).
73. Olufsen, M., Tran, H. & Ottesen, J. Modeling cerebral blood flow control during posture change from sitting to standing. *Cardiovasc. Eng.* **4,** 47–58 (2004).
74. Hall, C. N. *et al.* Capillary pericytes regulate cerebral blood flow in health and disease. *Nature* **508,** 55–60 (2014).
75. Gould, I. G., Tsai, P., Kleinfeld, D. & Linninger, A. The capillary bed offers the largest hemodynamic resistance to the cortical blood supply. *J. Cereb. Blood Flow Metab.* **37,** 52–68 (2017).
76. van Laar, P. J. *et al.* In vivo flow territory mapping of major brain feeding arteries. *Neuroimage* **29,** 136–44 (2006).

77. van der Zwan, A., Hillen, B., Tulleken, C. A. & Dujovny, M. A quantitative investigation of the variability of the major cerebral arterial territories. *Stroke* **24,** 1951–9 (1993).
78. Moore, S. M., Moorhead, K. T., Chase, J. G., David, T. & Fink, J. One-dimensional and three-dimensional models of cerebrovascular flow. *J. Biomech. Eng.* **127,** 440–449 (2005).
79. Cassot, F. *et al.* Branching patterns for arterioles and venules of the human cerebral cortex. *Brain Res.* **1313,** 62–78 (2010).
80. Reichold, J. *et al.* Vascular graph model to simulate the cerebral blood flow in realistic vascular networks. *J. Cereb. Blood Flow Metab.* **29,** 1429–1443 (2009).
81. Schneider, M., Reichold, J., Weber, B., Székely, G. & Hirsch, S. Tissue metabolism driven arterial tree generation. *Med. Image Anal.* **16,** 1397–414 (2012).
82. Olufsen, M. S. Structured tree outflow condition for blood flow in larger systemic arteries. *Am. J. Physiol.* **276,** H257-68 (1999).
83. Zauner, A., Daugherty, W. P., Bullock, M. R. & Warner, D. S. Brain oxygenation and energy metabolism: part I-biological function and pathophysiology. *Neurosurgery* **51,** 289–301; discussion 302 (2002).
84. Fantini, S., Sassaroli, A., Tgavalekos, K. T. & Kornbluth, J. Cerebral blood flow and autoregulation: current measurement techniques and prospects for noninvasive optical methods. *Neurophotonics* **3,** 031411 (2016).
85. Tzeng, Y.-C. & Ainslie, P. N. Blood pressure regulation IX: cerebral autoregulation under blood pressure challenges. *Eur. J. Appl. Physiol.* **114,** 545–59 (2014).
86. Bor-Seng-Shu, E. *et al.* Cerebral hemodynamics: concepts of clinical importance. *Arq. Neuropsiquiatr.* **70,** 352–6 (2012).
87. Attwell, D. *et al.* Glial and neuronal control of brain blood flow. *Nature* **468,** 232–243 (2010).
88. Lakin, W. D. *et al.* A whole-body mathematical model for intracranial pressure dynamics. *J. Math. Biol.* **46,** 347–383 (2003).
89. Liang, F. *et al.* A computational model study of the influence of the anatomy of the circle of willis on cerebral hyperperfusion following carotid artery surgery. *Biomed.Eng Online.* **10,** 84 (2011).
90. Liebeskind, D. S. Collateral circulation. *Stroke* **34,** 2279–2284 (2003).
91. Hendrikse, J., Hartkamp, M. J., Hillen, B., Mali, W. P. & van der Grond, J. Collateral ability of the circle of Willis in patients with unilateral internal carotid artery occlusion: border zone infarcts and clinical symptoms. *Stroke* **32,** 2768–73 (2001).
92. Alpers, B. J., Berry, R. G. & Paddison, R. M. Anatomical studies of the circle of Willis in normal brain. *A. M. A. Arch. Neurol. psychiatry* **81,** 409–418 (1959).
93. Hartkamp, M. J., van der Grond, J., van Everdingen, K. J., Hillen, B. & Mali, W. P. T. M. Circle of Willis Collateral Flow Investigated by Magnetic Resonance Angiography. *Stroke* **30,** 2671–2678 (1999).
94. Krabbe-Hartkamp, M. J. *et al.* Circle of Willis: morphologic variation on three-dimensional time-of-flight MR angiograms. *Radiology* **207,** 103–111 (1998).
95. Brozici, M., Van der Zwan, A. & Hillen, B. Anatomy and Functionality of Leptomeningeal Anastomoses: A Review. *Stroke* **34,** 2750–2762 (2003).
96. Menon, B. K. *et al.* Assessment of leptomeningeal collaterals using dynamic CT angiography in patients with acute ischemic stroke. *J Cereb Blood Flow Metab* **33,** 365–371 (2013).
97. M.J., L. *et al.* Predicting collateral status with magnetic resonance perfusion parameters: Probabilistic approach with a tmax-derived prediction model. *Stroke* **46,** 2800–2807 (2015).

Supplemental A

Author	Hemodynamics		Boundary conditions	Autoregulation	Leptomeningeal collaterals	Additional patient data
Alastruey, 2008[31]	Flow characteristics: pulsatile, non-linear Vessel wall: elastic, non-linear	Standard dataset	Proximal: pressure and velocity curves Distal: windkessel model	Non-linear change in resistances in response to change in CO_2	Not incorporated	None
Aoi, 2010[49]	Flow characteristics: pulsatile, linear Vessel wall: elastic, non-linear	Standard dataset	Proximal: pressure curve Distal: modelling the vasculature up to the venous system based on standard data.	Non-linear sigmoid control function changing compliance in response to cerebral blood flow	Not incorporated	None
Banaji, 2005[50]	Flow characteristics: pulsatile, linear Vessel wall: elastic, non-linear	Standard dataset	Proximal: pressure curve Distal: modelling vascular system based on standard data up to the venous system. Venous pressure behind	Non-linear change in response to changes in pressure, CO_2, oxygen saturation and other metabolic subsystems	Not incorporated	None
Bekker, 1996[51]	Flow characteristics: steady, linear Vessel wall: elastic, non-linear	Standard dataset	Proximal: static pressure Distal: compartments up till venous system, central venous pressure	Non-linear change in resistance in response to pressure changes	Not incorporated	None

Supplemental table: Relevant studies identified using a search in MEDLINE/PubMed, Scopus and Embase. MRA = magenetic resonsance angiography, n = number of subjects, PC-MRA = phase-contrast MRA, MCA = middle cerebral artery, PCA = posterior cerebral artery, 3DRA = 3D rotational angiography, MAP = mean arterial pressure, CTA = computed tomography angiography, CCA = common carotid artery, CO_2 = carbon dioxide.

Brosig, 2014[37]	Flow characteristics: pulsatile, non-linear Vessel wall: elastic, non-linear	3DRA (data of a phantom)	Proximal: volumetric flow based on measurement of bolus (contrast agent) arrival time during 3DRA Distal: optimized resistances based on the 3DRA data.	Not incorporated	Not incorporated	None
Cassot, 1995[52]	Flow characteristics: pulsatile, non-linear Vessel wall: elastic	Standard dataset	Proximal: pressure curve Distal: resistance blocks based on by standard data	Not incorporated	Not incorporated	None
Charbel, 2004[43]	Flow characteristics: pulsatile, non-linear Vessel wall: elastic, non-linear	MRA (n=16)	Proximal: PC-MRA Distal: resistances calculated using PC-MRA measurements	Not incorporated	Fitted based on the PC-MRA measurements.	None
Connoly, 2014[71]	Flow characteristics: pulsatile, non-linear Vessel wall: elastic, non-linear	Standard dataset	Proximal: volumetric flow rate Distal: compartment model based on standard data	Non-linear change in resistance response to CO_2	Not incorporated	None
David, 2003[20]	Flow characteristics: steady, non-linear Vessel wall: rigid	Standard dataset	Proximal: static pressure (92mmHg) Distal: resistance blocks divided by standard ratio with venous pressure distally from these.	Non-linear PID controller.	Not incorporated	None

Supplemental table: Continued

Devault, 2008[39]	Flow characteristics: pulsatile, non-linear Vessel wall: elastic, non-linear	MRA (n=1)	Proximal: doppler flow measurements Distal: windkessel model based on standard dataset	Not incorporated	Not incorporated	None
Ferrandez, 2002[21]	Flow characteristics: steady, linear Vessel wall: rigid	Standard dataset	Proximal: static pressure (92mmHg) Distal: resistance blocks divided by standard ratio with venous pressure distally from these.	Non-linear PID controller.	Not incorporated	None
Gao, 1998[54]	Flow characteristics: steady, linear Vessel wall: elastic, non-linear	Standard dataset	Proximal: pressure curve Distal: modelling arterial system based on Murray Law of minimum work. System consisted one compartment. Venous pressure behind.	Non-linear change in resistances in response to pressure change	Not incorporated	None
Grindberg, 2011[8]	Flow characteristics: pulsatile, non-linear Vessel wall: elastic, non-linear	MRA (n=2)	Proximal: PC-MRA Distal: windkessel model based on standard data	Not incorporated	Not incorporated	None
Guanghong 1997[40]	Flow characteristics: pulsatile, linear Vessel wall: elastic, linear	Standard dataset	Proximal: pressure curve Distal: transcranial doppler measurements of the major cerebral arteries.	Not incorporated	Not incorporated	None

Supplemental table: Continued

Hillen, 1986[28]	Flow characterisics: pulsatile, non-linear Vessel wall: Elastic, linear	Standard dataset	Proximal: Pressure curve Distal: resistance blocks divided by standard ratio with venous pressure distally from these.	Not incorporated	Not incorporated	None
Hillen, 1988[22]	Flow characteristics: steady, linear Vessel wall: rigid	Standard dataset	Proximal: Static pressure (92mmHg) Distal: resistance blocks divided by standard ratio with venous pressure distally from these.	Not incorporated	Not incorporated	None
Ho, 2010[41]	Flow characteristics: pulsatile, non-linear Vessel wall: elastic, non-linear	CTA (n=1)	Proximal: pressure curve Distal: Resistances of short rapid tapering arterial segments	Not incorporated	Not incorporated	Doppler velocity measurement in CCA for validation
Hoffman, 1987[55]	Flow characteristics: steady, non-linear Vessel wall: elastic, non-linear	Standard dataset	Proximal: static pressure Distal: venous pressure behind a compartment model based on standard data	Non-linear change in resistance based on perfusion pressure	Not incorporated	None
Ji, 2010[69]	Flow characteristics: pulsatile, non-linear Vessel wall: elastic, non-linear	Standard dataset	Proximal: velocity measured using doppler Distal: windkessel model	Not incorporated	Not incorporated	None

Supplemental table: Continued

Kailasnath, 1998[23]	Flow characteristics: steady, linear Vessel wall: rigid	3DRA (n=14)	Proximal: MAP Distal: resistance blocks divided by standard ratio with venous pressure distally from these.	Not incorporated	Not incorporated	None
Lakin, 2003[89]	Flow characteristics: pulsatile, linear Vessel wall: elastic, linear	Standard dataset	Proximal: pressure and flow curve at the level of the aorta Distal: modelling vascular system based on standard data up to the venous system. Venous pressure behind	Non-linear change in resistances in response to change in pressure.	Not incorporated	None
Liang, 2011[88]	Flow characteristics: pulsatile, non-linear Vessel wall: elastic, non-linear	Standard dataset	Proximal: pressure and flow based on 0D-model of the heart and body Distal: resistance blocks divided by standard ratio with a model of the venous circulation behind	Non-linear change in arteriolar resistance in response to pressure change	Not incorporated	None
Linninger, 2009[42]	Flow characteristics: pulsatile, linear Vessel wall: elastic, linear	MRA (n=11)	Proximal: PC-MRA velocity curve Distal: modelling vascular system up to venous system based on standard data. Venous pressure behind.	Not incorporated	Not incorporated	None

Supplemental table: Continued

Lodi, 1999[27]	Flow characteristics: steady, linear Vessel wall: elastic, linear	Standard dataset	Proximal: static pressure (100mmHg) Distal: converging all major arteries into serial resistances representing the vasculature based on standard data	Non-linear change of compliance in response to pressure change	Not incorporated	None
Moody, 1991[56]	Flow characteristics: steady, linear Vessel wall: elastic, non-linear	Standard dataset	Proximal: static pressure Distal: converging all major arteries into serial resistances representing the vasculature based on standard data. Venous pressure behind.	Non-linear change according to an autoregulatory curve	Not incorporated	None
Moorhead, 2004[25]	Flow characteristics: steady, linear Vessel wall: rigid	Standard dataset	Proximal: Static pressure Distal: resistance blocks based on standard data with venous pressure distally from these.	Non-linear change in resistances in response to pressure change	Not incorporated	None
Moorhead, 2006[24]	Flow characteristics: steady, linear Vessel wall: rigid	MRA (n=1)	Proximal: Static pressure Distal: resistance blocks divided by standard ratio with venous pressure distally from these.	Non-linear PID controller in response to oxygen changes	Not incorporated	None

Supplemental table: Continued

Müller, 2014[33]	Flow characteristics: pulsatile, non-linear Vessel wall: elastic, non-linear	MRA	Proximal: pressure curve Distal: resistance blocks resistance blocs based on standard data with venous pressure behind	Not incorporated	Not incorporated	None
Olufsen, 2002[5]	Flow characteristics: pulsatile, linear Vessel wall: elastic, non-linear	Standard dataset	Proximal: pressure curve Distal: resistance blocks based on by standard data with venous pressure behind.	Non-linear. Changes to pressure and flow.	Not incorporated	Finger measured blood pressure Doppler velocity of MCA for validation (n = 10)
Ornstein, 1994[57]	Flow characteristics: pulsatile, linear Vessel wall: elastic, linear	Standard dataset	Proximal: pressure curve Distal: modelling up to the venous system based on standard data. Venous pressure behind.	Linear change in resistance in response to pressure change	Not incorporated	None
Panerai, 1999[26]	Flow characteristics: pulsatile, both linear and non-linear Vessel wall: rigid	Standard dataset	Proximal: pressure and velocity curves measured using finger blood pressure and transcranial doppler of MCA (n=47) Distal: modelling vascular system based on standard data up to the venous system. Venous pressure behind	Linear and non-linear response in response to pressure change	Not incorporated	Transcutaneous CO_2 pressure measurement (n=47)

Supplemental table: Continued

Papapanayotou, 1990[58]	Flow characteristics: pulsatile, non-linear Vessel wall: elastic, linear	Standard dataset	Proximal: Pressure curve Distal: resistance blocks divided by standard ratio with venous pressure distally from these.	Not incorporated	Not incorporated	None
Payne, 2006[70]	Flow characteristics: pulsatile, non-linear Vessel wall: elastic, non-linear	Standard dataset	Proximal: pressure and velocity curves measured using finger blood pressure and transcranial doppler of MCA (n=5) Distal: modelling vascular system based on standard data up to the venous system. Venous pressure behind	Linear change in resistance in response to cerebral blood flow	Not incorporated	None
Pucher, 1988[15]	Flow characteristics: pulsatile, non-linear Vessel wall: elastic, non-linear	Standard dataset	Proximal: velocity curve based on standard data Distal: modelling vascular system up to venous system based on standard data. Venous pressure behind	Non-linear change in resistances in response to pressure change	Not incorporated	None
Reymond, 2009[4]	Flow characteristics: pulsatile, non-linear Vessel wall: elastic, non-linear	MRA (n=6)	Proximal: pressure-volume curve at level of the heart Distal: resistance blocks divided by standard ratio with venous pressure distally from these.	Not incorporated	Not incorporated	None

Supplemental table: Continued

Reymond, 2012[34]	Flow characteristics: pulsatile, non-linear Vessel wall: elastic, non-linear	MRA (n=1)	Proximal: PC-MRA at level of aorta Distal: resistance blocks resistance blocs based on standard data with venous pressure behind	Not incorporated	Not incorporated	None
Roessler, 2006[35]	Flow characteristics: pulsatile, linear Vessel wall: elastic, non-linear	MRA (n=4)	Proximal: velocity curve based on transcranial doppler Distal: Resistance blocks based on arterial diameter. Venous pressure behind.	Not incorporated	Not incorporated	None
Salehi, 2012[59]	Flow characteristics: pulsatile, non-linear Vessel wall: elastic, non-linear	Standard dataset	Proximal: pressure curve Distal: structured tree based on branching patterns and method reported by Olufsen et al.[82]	Not incorporated	Not incorporated	None
Schwarz, 2008[60]	Flow characteristics: pulsatile, linear Vessel wall: elastic, linear	MRA (n=1)	Proximal: pressure curve Distal: standard resistances based on literature. 0mmHg pressure behind	Not incorporated	Not incorporated	None
Spronck, 2012[72]	Flow characteristics: pulsatile, linear Vessel wall: elastic, non-linear	Standard dataset	Proximal: pressure curve Distal: resistance blocks based on standard data with venous pressure distally from these.	Non-linear change in resistance in response to changes in pressure and increased brain activity.	Not incorporated	Transcranial doppler measurements of PCA. (n=11)

Supplemental table: Continued

Ursino, 1988[61]	Flow characteristics: pulsatile, linear Vessel wall: elastic, non-linear	Standard dataset	Proximal: pressure curve Distal: converging all major arteries into serial resistances representing the vasculature based on standard data	Non-linear change in resistance in response to pressure changes	Not incorporated	None
Ursino, 1988[65]	Flow characteristics: pulsatile, linear Vessel wall: elastic, non-linear	Standard dataset	Proximal: pressure curve Distal: converging all major arteries into serial resistances representing the vasculature based on standard data	Non-linear change in resistance in response to pressure changes	Not incorporated	None
Ursino, 1991[62]	Flow characteristics: steady, linear Vessel wall: elastic, non-linear	Standard dataset	Proximal: static pressure (85mmHg) Distal: converging all major arteries into serial resistances representing the vasculature based on standard data	Non-linear change in resistance in response to pressure changes	Not incorporated	None
Ursino, 2001[64]	Flow characteristics: pulsatile, linear Vessel wall: elastic, non-linear	Standard dataset	Proximal: pressure curve Distal: modelling vascular system based on standard data up to the venous system. Venous pressure behind	Non-linear change in resistances in response to change in pressure, CO_2 and oxygen saturation	Not incorporated	None

Supplemental table: Continued

Ursino, 2003[63]	Flow characteristics: pulsatile, linear Vessel wall: elastic, non-linear	Standard dataset	Proximal: pressure curve Distal: converging all major arteries into serial resistances representing the vasculature based on standard data	Non-linear change in resistance in response to pressure changes	Not incorporated	None
Vaičaitis, 2011[36]	Flow characteristics: pulsatile, non-linear Vessel wall: elastic, linear	MRA (n=1)	Proximal: pressure curve Distal: modelling vasculature up to the artriol level using a constrained constructive optimization algorithm. 50mmHg pressure behind	Not incorporated	Not incorporated	None
Viedema, 1997[66]	Flow characteristics: pulsatile, non-linear Vessel wall: elastic, non-linear	Standard dataset	Proximal: velocity curve Distal: resistance blocks based on by standard data.	Non-linear PID controller.	Not incorporated	None
Wang, 2008[67]	Flow characteristics: pulsatile, linear Vessel wall: elastic, linear	Standard dataset	Proximal: Pressure curve Distal: resistance blocks divided by standard ratio with venous pressure distally from these.	Non-linear in response to pressure changes	Not incorporated	None
Zagzoule, 1986[68]	Flow characteristics: pulsatile, non-linear Vessel wall: elastic, linear	Standard dataset	Proximal: Pressure curve Distal: converging all major arteries into serial resistances representing the vasculature based on standard data	Linear change in resistance in response to pressure changes	Not incorporated	None

Supplemental table: Continued

4

High resolution 7T and 9.4T-MRI of human cerebral arterial casts enables accurate estimations of the cerebrovascular morphometry

Authors:
Jasper H.G.Helthuis, MD, MSc.[1,3], Albert van der Zwan, MD, PhD[1,3], Tristan P.C. van Doormaal, MD, PhD[1,3], Ronald L.A.W. Bleys, MD, PhD[2], Anita A. Harteveld, MSc[4], Annette van der Toorn, PhD[6], Mariana Brozici, MD[2,5], Jeroen Hendrikse, PhD[4], Jaco J.M.Zwanenburg, PhD[4]

Affiliations:
[1] University Medical Center Utrecht, Brain Center Rudolf Magnus, Department of Neurology and Neurosurgery, Utrecht, The Netherlands
[2] University Medical Center Utrecht, Department of Anatomy, Utrecht, The Netherlands
[3] Brain Technology Institute, Utrecht, The Netherlands
[4] University Medical Center Utrecht, Department of Radiology, Utrecht, The Netherlands
[5] Heilig Hart Ziekenhuis, Department of Pulmonology, Mol, Belgium.
[6] Biomedical MR Imaging and Spectroscopy Group, Center for Image Sciences, University Medical Center Utrecht, The Netherlands.

Status:
Operative Neurosurgery, 2018 Aug 1;15(2):217-230

Abstract

Quantitative data on the morphology of the cerebral arterial tree could aid in modelling and understanding cerebrovascular diseases, but is scarce in the range between 200 micrometres and 1 mm diameter arteries. Traditional manual measurements are difficult and time consuming. 7T-MRI and 9.4T-MRI of human cerebral arterial plastic casts could proof feasible for acquiring detailed morphological data of the cerebral arterial tree in a time efficient method. One cast of the complete human cerebral arterial circulation embedded in gadolinium-containing gelatine gel was scanned at 7T-MRI (0.1mm isotropic resolution). A small section of another cast was scanned at 9.4T-MRI (30μm isotropic resolution). Subsequent 3D-reconstruction was performed using a semi-automatic approach. Validation of 7T-MRI was performed by comparing the radius calculated using MRI to manual measurements on the same cast. As manual measurement of the small section was not feasible, 9.4T-MRI was validated by scanning the small section both at 7T-MRI and 9.4T MRI and comparing the diameters of arterial segments. Linear regression slopes were 0.97 (R-squared 0.94) and 1.0 (R-squared 0.90) for 7T-MRI and 9.4T-MRI. This data shows that 7T-MRI and 9.4T-MRI and subsequent 3D reconstruction of plastic casts is feasible, and allows for characterization of human cerebral arterial tree morphology.

Introduction

Quantitative data on the morphology of the cerebral arterial tree could lead to better understanding of cerebral blood flow and could aid in modelling and understanding cerebrovascular diseases.[1] One example would be generation of a general hemodynamic model for study on specific diseases, such as stroke. A secondary option is to generate boundary conditions in patient-specific aneurysm flow models, for planning and evaluating the risk of by-pass surgery. The cerebral arterial resistance is known to be generated largely by the arterioles and capillaries.[2,3]

However, to our knowledge only a limited number of studies to quantify this morphology of arteries in the range between 200 micrometres and 1 mm diameter have been performed.[4–6] The paucity of data in this range hampers the development of both general and patient-specific models of the entire cerebral arterial circulation.

The larger end of the 0.2-1mm range can be obtained by in vivo angiographic imaging with MRI,3D computed tomography angiography (CTA) or 3D digital subtraction angiography.[6,7] However, even with modern techniques the smaller end is not well visualized in vivo and is vulnerable to measurement errors due to motion of the subject.

Detailed morphological data over the entire range could be acquired by manual measurements on corrosion casts of the cerebral arterial tree which are obtained by injecting a solidifying material (e.g. plastic) in the major cerebral arteries. These casts can retain arteries up to the pre-arteriole level, after removing brain tissue by corroding with substances such as potassium hydroxide. An alternative is manual dissection of arteries and subsequent measurement.[8–10]. However, measurements on casts and dissection are difficult and time consuming to perform on smaller arteries. Micro-CT and confocal laser microscopy can ease these measurements. Availability of scanners which can handle larger samples at a high resolution are limited. 7T magnetic resonance imaging (MRI) has the advantage of reaching high resolutions combined with a larger field of view, comparable to industrial micro-CT systems. 7T MRI could proof to be a good alternative to micro-CT, especially when the latter is not available or when local available systems cannot handle large sample sizes.[5,11–14] Additionally, a (semi)-automatic subsequent 3D reconstruction technique could ease and greatly speed up the measurement process. This technique could fill the gap of missing data in the 0.2-1 mm range by scanning polymer cerebral arterial casts.

The aim of the current study was to access the feasibility of 7T-MRI and 9.4T-MRI scanning of human cerebral arterial plastic casts for acquiring detailed morphological data for a large part of the cerebral arterial tree.

Methods

Cast preparation

Casts were available from a previous unpublished study in which casts were stored after air-drying. These casts were made from vessels of two brains that were derived from bodies that were donated to the Department of Anatomy. From these persons written informed consent was obtained during life that allowed the use of their entire bodies for educational and research purposes. In accordance with the Dutch law on dead bodies no IRB approval was required. There was no knowledge of cerebrovascular disease in the subjects and the cause of death was not related with any cerebrovascular disease. The unembalmed human brains (both females, 78 and 57 years)) were obtained by cutting its connecting structures to the skull base after removal of the skull cap. Casts (see *figures 1a* and *2a*) were produced by cannulating the six major cerebral arteries of the brain after the circle of Willis and injecting these with a mixture of Araldite F/hardener HY 2967/dilutioner DY 026 SP and by subsequently corroding them, as described previously in more detail.[15]

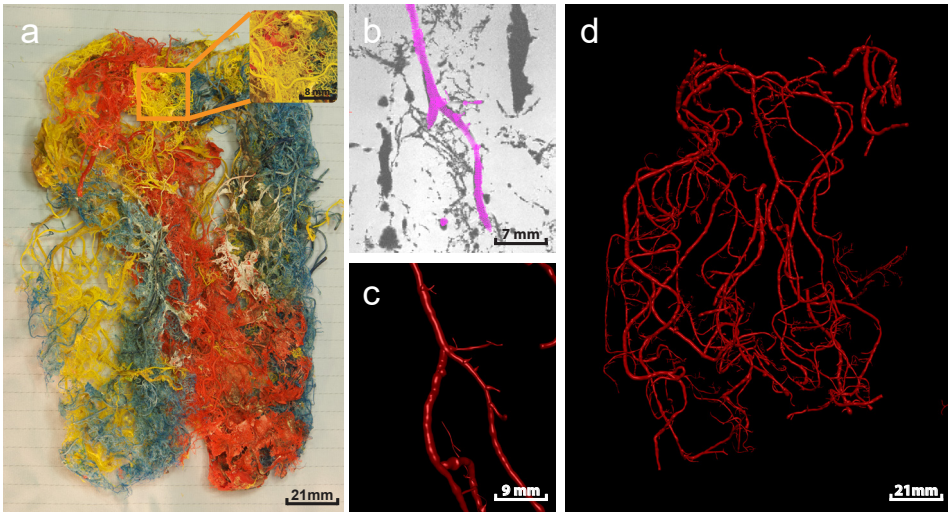

Figure 1: A human cerebral cast scanned with 7T MRI.

a) Photographic image of the complete cast. The inset shows the enlarged section indicated by the orange square. Different pigments where used for different major cerebral arteries during injection of Araldite F. b) Detail of a 7T MRI image (100 µm isotropic resolution), with segmented artery as displayed in Simple Neurite Tracer. c) The segmented artery of panel b in 3D representation. d) 3D visualisation of all reconstructed arteries. As the reconstruction approach was semi-automatic not all arteries in the casts are segmented, only arteries which were manually selected in Simple Neurite Tracer are reconstructed to 3D.

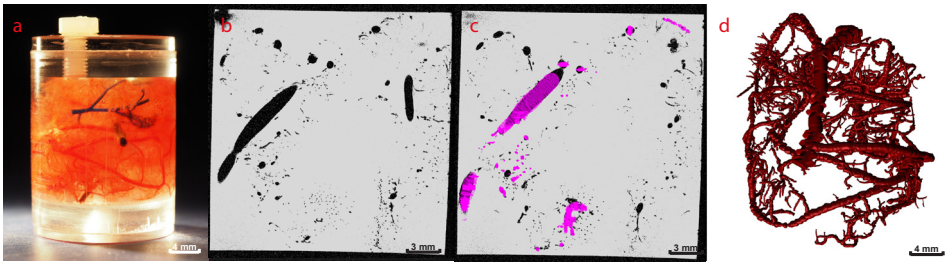

Figure 2: Small section of the human cerebral cast scanned with 9.4T MRI.
a) The cast section embedded in gel in a small plastic container, b) Single slice from MRI (30 µm isotropic resolution), c) Segmented arteries on single slice as displayed in Simple Neurite Tracer. d) 3D visualisation of all reconstructed arteries.

Preparation for scanning

7T-MRI

A challenge for scanning polymer vessel casts with MRI is that the solid polymers do not yield an MRI detectable signal. This could be overcome by embedding the cast in a gadolinium-containing gel. The cast (female, 78 years) was placed in a 14% gelatine tap water gel. To increase the attainable signal-to-noise ratio per unit scan time for high resolution imaging, the T_1 of the gel was shortened by using gadolinium-containing contrast-agent ($2.8*10^{-3}$ mL contrast-agent/mL water; Gadobutrol, Gadovist 1.0mmol/mL, Bayer Schering Pharma, Newbury, UK). The complete cast was placed in a custom-made PVC container to which the gadolinium-gelatine solution was added, while avoiding the formation of air bubbles by slowly pouring the gadolinium-gelatine solution. The container was left overnight at 5 degrees Celsius for the gelatine to solidify.

9.4T-MRI

From one cast (female, 57 years) a small cylindrical section with approximate dimensions of 7.5mm radius and 15mm height was cut with a diagonal pliers aided by an operating microscope (Universal S3, Carl Zeiss Meditec Inc., Dublin, California, USA, magnification 10-40x). This section was placed in a custom-made polymethyl methacrylate (Perspex) container and the above-mentioned gadolinium-gelatine solution was added. The Perspex container was subsequently placed in a desiccator for 10 minutes, followed by an ultrasonic cleaner for 10 minutes to remove air from the solution. During these steps, solidification of the solution was prevented by placing the container in a hot tap water bath. The container was left overnight at 5 degrees Celsius.

Scan protocol

7T-MRI

Imaging was performed on a 7T whole body system (Philips Healthcare, Cleveland, OH, USA) with a 60 cm bore diameter and maximum gradient strength / slew rate of 40 mT/m / 200 mT/m/s, a custom-made 16-channel surface coil (MR Coils B.V. Zaltbommel, The Netherlands) for signal reception, and a volume transmit/receive coil for transmission (Nova Medical, Wilmington, MA, USA). The following imaging parameters were used for T1w imaging of both casts: TR 35 ms, TE 15 ms, flip angle 60 degrees, number of slices 300, bandwidth 106.4 Hz/pixel, TFE factor (number of excitations in each shot) 1004. The scanner resonance frequency was measured and adjusted between each shot (of approximately 35 s duration), to mitigate potential artefacts caused by frequency drift of the scanner. The field-of-view (FOV) was 150x150x30mm^3 with an acquired voxel size of 0.1x0.1x0.1mm^3. The scan duration was 3h46min.

9.4T-MRI

Imaging was performed on a 9.4T/21 cm MR system (Varian Inc., Palo Alto, CA, USA) equipped with a gradient insert of 6cm internal diameter with gradients up to 1 T/m. A home-built inductively coupled 3 turn surface coil with an internal diameter of 21 mm was used that tightly fitted the sample. A 3D balanced SSFP sequence was used with the following scan parameters: TR/TE 8/4ms, flip angle 45°, acquired voxel size of 0.03x0.03x0.03 mm^3 and a FOV of 19.8x19.8x19.8 mm^3, phase increments of 0°, 90°,180° and 270° for subsequent image acquisitions and 18 averages per phase increment. The acquisition time for a single 3D image (without phase increments) was about 58 minutes, resulting in a total acquisition time of 18*4*58 minutes = 70 hrs. The raw data were multiplied with a 3D Hanning window (660 points in every direction) and zerofilled to 1320 points in every direction before Fourier transformation. After Fourier transformation the complex images of the different phase increments were added and the absolute of the summed result was used for further quantification.

Post-processing

Normalization

The small receiver elements of the 7T-MRI receiver coil caused signal fall-off at further distance from the coils, which hampered automated image analysis. This image inhomogeneity was corrected by data normalization. The density of the cast in the gelatine-gel was relatively low, thus justifying to ignore the presence of the cast in the gel, and to use a straightforward moving average filter (empirically chosen size 24x24x5) to obtain the normalization factor map for correction. (*Figure 3a* and *3b*)

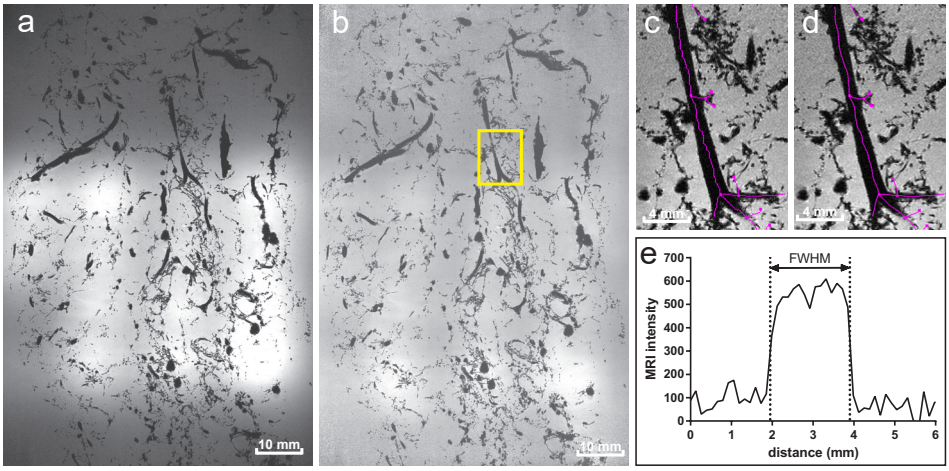

Figure 3: Post-processing steps.

a) Original 7T MRI single image showing the signal inhomogeneity due to local small receive coils. b) Normalized image with yellow square marking close-up region of interest. c) Close-up of non-smoothed centerlines. d) Close-up of smoothed centerlines. e) example of one intensity profile trough the artery on which the estimated radius (obtained with full-width at half-maximum method) of the artery is depicted.

Centrelines

The 3D morphology of the cerebral arterial tree was described by artery centrelines and radii. Full automatic computation of centrelines was impossible due to many small (smaller than the voxel size) intertwined arteries that appeared as blobs. Hence, we used a semi-automatic approach aided by Simple Neurite Tracer (SNT, Version 2.0.2)[16] in Fiji (ImageJ 1.50b, National Institutes of Health, USA)[17,18]. By selecting two locations in a vessel, SNT automatically generates the centreline between these two locations, based on voxel intensity values. This curved centreline is composed of many short, straight line pieces between automatically generated nodes. Bifurcations were made by starting a second path on a previously generated path Image contrast was inverted prior to generation of the centrelines in SNT.(*Figure 3c*)

Centrelines generated by SNT had a slight saw tooth profile, which was corrected by applying a smoothing algorithm (SmoothN, version 1.37) in MatLab (version 8.3, MathWorks Inc., Natick, MA, USA).[19,20] On visual inspection a smoothing parameter of 20 proved to be optimal. (*Figure 3d*)

Radius calculation

Radius calculation was performed using a custom MatLab code that calculated the radius for all nodes. For each node, fifty radial intensity profiles were sampled by rotating the profile (in steps of 7.2 degrees) around the centreline at three locations spread over the straight line piece connecting the node of interest and its previous connecting node. We opted for using these three locations as we wanted each node to represent the average radius of the straight line connecting with the previous node.

SNT automatically generates the At locations where multiple arteries are very close, some of the radial intensity profiles will yield an overestimation of the actual radius as the second artery might also be included in radius calculation. As the radii obtained from the 50 radial intensity profiles should represent a circular artery, the circularity index (*Q*) was computed at each location to detect this overestimation:

$$Q = \frac{(4 \times \pi \times A)}{L^2}$$

in which *A* is the cross-sectional area and *L* the circumferential length. In case of a perfect circle, Q is equal to 1, whereas in a shape less like a circle (*e.g.* an ellipse) Q decreases.

For each location, the fraction 1-Q largest radii were excluded. For example a Q of 0.80 would mean that the largest 20% of calculated radii were excluded. Visual inspection at a number of locations showed that this heuristic approach was effective at removing incorrect data profiles. The remaining radii for all points were averaged. After calculation the radii for all nodes, the results were saved in a file containing the arterial tree with all connectivity information and radii in a standard text file format (SWC format), as specified by Cannon et al.[21]

Validation of MRI measurements

The 7T-MRI measurements were validated by measuring the artery diameters at 50 locations by hand using a digital calliper on the cast (Mitutoyo Corp. Takatsu-ku, Japan, Accuracy ±0.001 mm) aided by an operating microscope (Universal S3, Carl Zeiss Meditec Inc., Dublin, California, USA, magnification 10-40x) at the same location as in the MRI data using the calculated radii.

As the small arteries scanned with 9.4T-MRI could not be measured manually using a calliper, validation of 9.4T-MRI data was performed by scanning the container with the small cast section also on the 7T MRI, and comparing the measured radii at 50 arterial segments. Only segments with a 7T-MRI radius larger than one voxel (0.1 mm) were regarded valid for the validation measurements Therefore, segments with a smaller radius were excluded from analysis.

Statistical analysis

Linear regression analysis was performed for the manual and 7T-MRI measurements, and for the 7T and 9.4T-MRI measurements. An intraclass correlation coefficient (ICC) using a Two-Way Mixed effect looking for absolute agreement of data and Bland-Altman plots with a range of agreement defined as a mean bias of ±2 standard deviations (SD) were performed. An acceptable threshold of bias was set at +/- 0.05 mm as this is expected to be comparable to variability in manual measurements. Linear regression analysis was used on the Bland-Altman plots to check for proportional differences. Linear regression and production of graphs was done using GraphPad Prism (version 6.01, GraphPad Software, Inc. La Jolla, CA, USA). All other statistical analyses were performed using IBM SPSS Statistics (version 23.0.0.0, IBM Company, Armonk, NY, USA). The datasets generated during and/or analysed during the current study and MatLab scripts are available from the corresponding author on reasonable request.

Results

3D reconstruction results

Figure 1 and 2 show photographs of the casts (*figures 1a* and *2a*), an example of the 7T and 9.4T-MRI data (*figures 2b*, *3a* and *3b*) and the subsequent reconstructed arterial tree (*figures 2d and 3d*). Using 7T and 9.4T-MRI arteries with radii down to 100 and 30 micrometres, respectively, could be reconstructed. The median radius for 7T-MRI was 0.4 mm (interquartile range 0.28-0.52 mm) and 0.12 mm (interquartile range 0.09-0.17 mm) for 9.4T-MRI. (*Figure 4*)

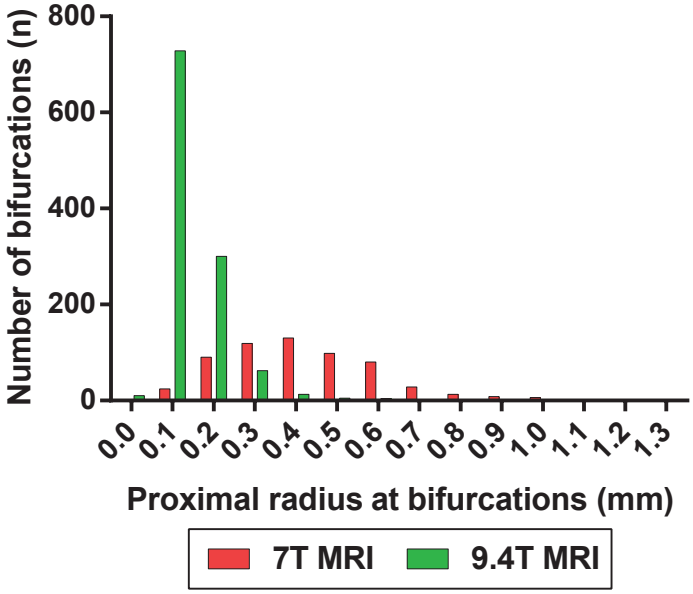

Figure 4: Absolute number of bifurcations for radius (mm) of proximal arteries of all bifurcations as measured on cast. Zero bin contains all values < 0.05 mm.

MRI validation

Linear regression analysis of the manual measurements vs. the 7T MRI radii (*Figure 5a*) showed a slope of 0.97 (95%-CI 0.90-1.04, Y-intercept: 0.07, R-squared=0.94). The ICC of single measurements was 0.96 (95%-CI 0.91-0.98). The Bland-Altman plot showed a bias of -0.05 mm with limits of agreement between 0.23 and -0.13 mm (*Figure 5b*). Linear regression analysis on the Bland-Altman showed no significant slope (-0.001 mm/mm, 95%-CI -0.072-0.070 mm/mm, p=0.98).

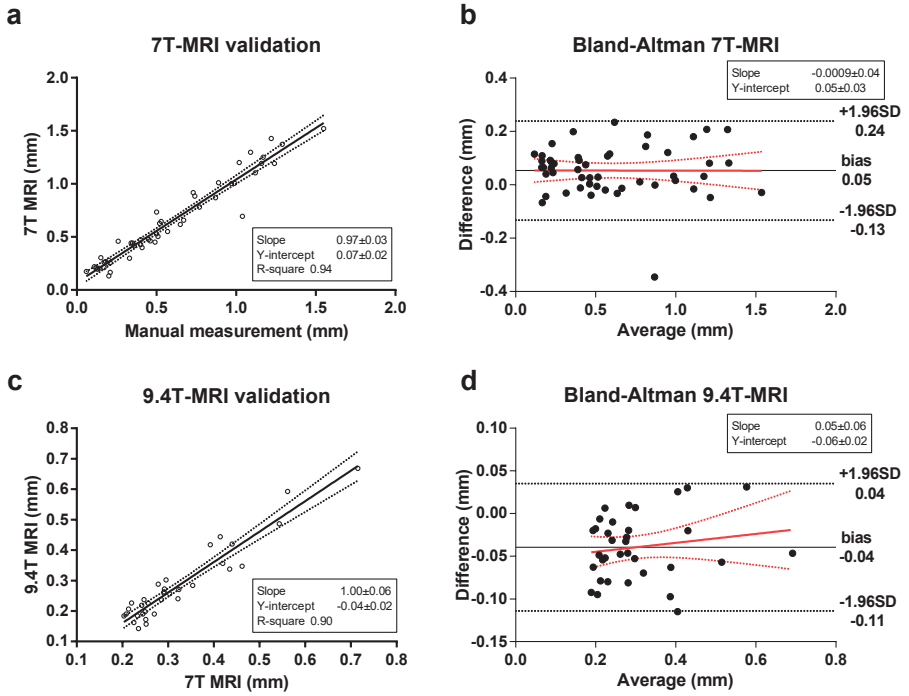

Figure 5: 7T-MRI and 9.4T-MRI validation.

a-b) 7T-MRI validation by comparison of direct manual diameter measurements on cast using digital callipers and measurement performed on 3D reconstructed cast. c-d) 9.4T-MRI validation by comparison of diameter measurements performed using 7T and 9.4T-MRI on the same segments in a casts. a) Linear regression (solid line) analysis with 95%-confidence interval (dotted lines) of manual versus 7T MRI measurements. b) Blant-altman plot of difference versus average for 7T MRI validation (difference: 7T MRI minus manual measurements) . c) Linear regression (solid line) analysis with 95%-confidence interval (dotted lines) of 7T versus 9.4T MRI. d) Blant-Altman plot of difference versus average for 9.4T MRI validation (difference: 9.4T diameter minus 7T diameter).

Of the 50 segments selected for 9.4T-MRI validation, 16 had a 7T-MRI diameter < 0.1 mm and were excluded, yielding 34 measurements for comparison with 7T-MRI. Linear regression analysis (*Figure 5c*) showed a slope of 1.00 (95%-CI: 0.88-1.12, Y-intercept: -0.04, R-square = 0.90).The ICC of single measurements was 0.90 (95%-CI 0.43-0.97). The Bland-Altman plot showed a bias of 0.05 mm with limits of agreement between 0.04 and -0.11 mm (see *Figure 5d*). Linear regression on the Bland-Altman showed no significant slope (0.052 mm/mm 95%-CI 0.062-0.17 mm/mm, p = 0.36).

Discussion

This study shows that it is feasible to scan human cerebral arterial polymer casts with a human whole body 7T-MRI, providing the potential to characterize morphology of the human cerebral arterial tree over a large volume for vessels ≥0.1 mm in radius. Vessels down to a radius of 30 μm can be assessed at 9.4T-MRI (small bore system) showing the advantage of an increased resolution at the expense of a smaller sample volume. 7T-MRI performed well compared to manual measurements and 9.4T-MRI showed a very close agreement with the 7T-MRI measurements.

This technique could be an alternative to current techniques such as Micro-CT. Micro-CT will achieve a resolution slightly higher than that of the current presented 7T-MRI technique with a comparable scanning times of 2-6 hours.[13,14] The decision which technique is most feasible will depend on local availability and experience with either Micro-CT, 7T-MRI and 9.4T-MRI techniques. MRI has the advantage that it also allows for complementary in-vivo studies of the vasculature and blood flow.[22,23] However, *in vivo* CTA, MRI and 3D angiography can only be used to characterize the morphology of the larger end of the cerebral arterial tree, which makes it of limited use for the current purpose of characterizing the vascular tree in the range of 0.2 – 1 mm.[6,7]

The use of casts embedded in gadolinium-containing gelatine gel resulted in a high contrast between plastic arteries and surrounding gel and a high signal-to-noise ratio, even at the ultra-high resolutions achieved with 9.4T-MRI. This resulted in a new method for resolving the cerebral arterial tree at high resolutions.

At these high resolutions, the removal of air bubbles from the gadolinium-containing gelatine gel proved to be crucial. At the resolutions of 7T-MRI the artefacts caused by air could be avoided as long as the gel was carefully added into the PCV container such that no significant air bubbles were created. However, at the higher resolution used at 9.4T-MRI, sensitivity to artefacts caused by air increased and removal of even microscopic air bubbles became vital. This was successfully done by using a desiccator and an ultrasonic cleaner.

Because of the complex nature of the casts, fully automatic 3D reconstruction of the complete arterial network proved to be practically impossible. Hence, the current work opted for a semi-automatic approach. This approach is more time-consuming than an automatic approach but is still faster than traditional manual measurements on casts or dissected arterial trees. Using the current method, measuring a large number of assessable segments lengths and radii of a single cast could be captured in a 3-4

days (excluding MRI scan time). From our own experience capturing a comparable amount of data or radii using manual measurements on a single cast takes 1 week. If lengths are also required manual measurement on casts is not feasible and dissection is the preferred traditional method. Acquisition of a comparable amount of data on radii and lengths of arteries up to 300 micrometres from our own experience can take up to 1,5 months of full time work when done accurately.

In future research this method could be used to acquire large data-sets with quantitative knowledge and general descriptive of the morphology of the cerebral arterial tree. These could in turn be used for different purposes. One example would be generation of a general hemodynamic model for study on specific diseases, such as stroke and Moyamoya disease. A secondary option is to generate boundary conditions in patient-specific aneurysm flow models, for planning and evaluating the risk of by-pass surgery. The cerebral arterial resistance is known to be generated largely by the arterioles and capillaries.[2,3] Morphological data on the more distal arteries and arterioles in the cerebral arterial tree captured using 7T-MRI and 9.4T-MRI coupled with already existing morphological data on the larger cerebral arteries and the capillary network could prove valuable in estimating correct boundary conditions by enabling calculation of this resistance distally from the major cerebral arteries.[6,19,20,24]

The techniques used in the current study have their limitations. (a) Because of the limits to resolution, small side branches might be missed. The cerebral circulation is known to have many small perforating side branches which are often smaller than 10% in diameter of their parent artery.[25,26] For an artery smaller than two millimetres in diameter such a side branch would already be smaller than what is possible to measure using 7T-MRI at a resolution of 0.1 mm. (b) The used echo time might result in an increase in diameter appearance on MRI data. However, the current study found a good correspondence between manual measurements and MRI measurements which suggests that this effect was limited. (c) Intertwined arteries can appear larger in diameter when using purely a FWHM method. The circularity filter that was applied appeared to effectively avoid these errors, given the results of the validation. (d) An increasing field strength and resolution of 9.4T-MRI compared to 7T-MRI resulted in a decreased volume which could be captured, comparable to techniques such as micro-CT and confocal laser microscopy. This would limit acquisition of data on morphology of arteries smaller than 0.1 mm in radius of the cerebral arterial tree to only a small section of a cast. When acquiring general descriptive morphological data on the complete cerebral arterial tree, such a small section might theoretically not be representative for the remainder of the cerebral arterial tree. However, the use of multiple small sections of the same cast could give a better representation of the

cerebral arterial tree. (e) Finally, the quality of the casts which are used might influence the acquired morphology and its representation of the actual physiological situation. The radius of the arteries in the casts will depend on the pressure used during injection and shrinkage of the injection material during solidification and erosion. Pressure can be controlled and kept at a physiological level during production of casts. Shrinkage of Araldite F as used in the current study is known to be 3.17±0.52% and thus minimal.[15] Gravity may result in deformation off the casts, especially after air-draying the casts. We expect that this doesn't affect radius and length measurements but does have its effects when morphological branching angles are of interest.

In conclusion, 7T and 9.4T-MRI scanning of plastic casts embedded in gadolinium-containing gelatine gel makes it feasible to obtain quantitative characterization of the cerebral arterial morphology in a timely manner, easing characterisation of multiple casts. This data might help in modelling and understanding various cerebrovascular diseases.

Acknowledgements

We would like to thank Hugo Kuijf for his initial advice on possible reconstructive methods.

References

1. Hirsch, S., Reichold, J., Schneider, M., Székely, G. & Weber, B. Topology and hemodynamics of the cortical cerebrovascular system. *J. Cereb. Blood Flow Metab.* **32,** 952–67 (2012).
2. Baumbach, G. L. & Heistad, D. D. Regional, segmental, and temporal heterogeneity of cerebral vascular autoregulation. *Ann. Biomed. Eng.* **13,** 303–10 (1985).
3. Hall, C. N. *et al.* Capillary pericytes regulate cerebral blood flow in health and disease. *Nature* **508,** 55–60 (2014).
4. Cassot, F., Lauwers, F., Fouard, C., Prohaska, S. & Lauwers-Cances, V. A novel three-dimensional computer-assisted method for a quantitative study of microvascular networks of the human cerebral cortex. *Microcirculation* **13,** 1–18 (2006).
5. Cassot, F. *et al.* Branching patterns for arterioles and venules of the human cerebral cortex. *Brain Res.* **1313,** 62–78 (2010).
6. Rossitti, S. & Löfgren, J. Vascular dimensions of the cerebral arteries follow the principle of minimum work. *Stroke* **24,** 371–377 (1993).
7. Lescher, S., Samaan, T. & Berkefeld, J. Evaluation of the pontine perforators of the basilar artery using digital subtraction angiography in high resolution and 3D rotation technique. *AJNR. Am. J. Neuroradiol.* **35,** 1942–7 (2014).
8. Horsfield, K. & Woldenberg, M. J. Diameters and cross-sectional areas of branches in the human pulmonary arterial tree. *Anat. Rec.* **223,** 245–51 (1989).
9. Mittal, N. *et al.* A computer reconstruction of the entire coronary arterial tree based on detailed morphometric data. *Ann. Biomed. Eng.* **33,** 1015–26 (2005).
10. Koike, K., Ohnuki, T., Ohkuda, K., Nitta, S. & Nakada, T. Branching architecture of canine pulmonary arteries: a quantitative cast study. *Tohoku J. Exp. Med.* **149,** 293–305 (1986).
11. Nordsletten, D. A., Blackett, S., Bentley, M. D., Ritman, E. L. & Smith, N. P. Structural morphology of renal vasculature. *Am. J. Physiol. Heart Circ. Physiol.* **291,** H296-309 (2006).
12. Du Plessis, A. & Rossouw, P. X-ray computed tomography of a titanium aerospace investment casting. *Case Stud. Nondestruct. Test. Eval.* **3,** 21–26 (2015).
13. du Plessis, A., le Roux, S. G. & Guelpa, A. Comparison of medical and industrial X-ray computed tomography for non-destructive testing. *Case Stud. Nondestruct. Test. Eval.* **6,** 17–25 (2016).
14. Dalstra, M. *et al.* Hard X-ray micro-tomography of a human head post-mortem as a gold standard to compare X-ray modalities. *Soc. Photo-Optical Instrum. Eng. Conf. Ser.* **9967,** (2016).
15. Van Der Zwan, A. & Hillen, B. Araldite F as injection material for quantitative morphology of cerebral vascularization. *Anat. Rec.* **228,** 230–6 (1990).
16. Longair, M. H., Baker, D. A. & Armstrong, J. D. Simple Neurite Tracer: open source software for reconstruction, visualization and analysis of neuronal processes. *Bioinformatics* **27,** 2453–4 (2011).
17. Schindelin, J. *et al.* Fiji: an open-source platform for biological-image analysis. *Nat. Methods* **9,** 676–82 (2012).
18. Schneider, C. A., Rasband, W. S. & Eliceiri, K. W. NIH Image to ImageJ: 25 years of image analysis. *Nat. Methods* **9,** 671–5 (2012).
19. Garcia, D. Robust smoothing of gridded data in one and higher dimensions with missing values. *Comput. Stat. Data Anal.* **54,** 1167–1178 (2010).

20. Garcia, D. A fast all-in-one method for automated post-processing of PIV data. *Exp. Fluids* **50,** 1247–1259 (2011).
21. Cannon, R. C., Turner, D. A., Pyapali, G. K. & Wheal, H. V. An on-line archive of reconstructed hippocampal neurons. *J. Neurosci. Methods* **84,** 49–54 (1998).
22. van Ooij, P. *et al.* Quantification and visualization of flow in the Circle of Willis: Time-resolved three-dimensional phase contrast MRI at 7 T compared with 3 T. *Magn. Reson. Med.* **69,** 868–876 (2013).
23. Bouvy, W. H. *et al.* Assessment of blood flow velocity and pulsatility in cerebral perforating arteries with 7-T quantitative flow MRI. *NMR Biomed.* **29,** 1295–1304 (2016).
24. Cassot, F., Lauwers, F., Lorthois, S., Puwanarajah, P. & Duvernoy, H. Scaling laws for branching vessels of human cerebral cortex. *Microcirculation* **16,** 331–344 (2009).
25. Marinkovic, S. V., Milisavljevic, M. M., Kovacevic, M. S. & Stevic, Z. D. Perforating branches of the middle cerebral artery. Microanatomy and clinical significance of their intracerebral segments. *Stroke* **16,** 1022–9 (1985).
26. Umansky, F. *et al.* The perforating branches of the middle cerebral artery. A microanatomical study. *J. Neurosurg.* **62,** 261–8 (1985).

5

Branching pattern of the cerebral arterial tree

Authors:
Jasper H.G.Helthuis, MD[1,4], Tristan P.C. van Doormaal, MD, PhD[1,4], Berend Hillen, MD, PhD[3], Ronald L.A.W. Bleys, MD, PhD[2], Anita A. Harteveld, PhD[5], Jeroen Hendrikse, MD, PhD[5], Annette van der Toorn, PhD[5], Mariana Brozici, MD[2,6], Jaco J.M.Zwanenburg, PhD[5], Albert van der Zwan, MD, PhD[1,4]

Affiliations:
1 University Medical Center Utrecht, Department of Neurosurgery, Utrecht, The Netherlands
2 University Medical Center Utrecht, Department of Anatomy, Utrecht, The Netherlands
3 Radboud University Medical Center, Departent of Anatomy, Nijmegen, The Netherlands
4 Brain Technology Institute, Utrecht, The Netherlands
5 University Medical Center Utrecht, Department of Radiology, Utrecht, The Netherlands
6 Heilig Hart Ziekenhuis, Department of Pulmonology, Mol, Belgium.

Status:
Anatomical Record, 2018 Oct 17. Epub ahead of print

Abstract

Quantitative data on branching patterns of the human cerebral arterial tree are lacking in the 1.0-0.1 mm radius range. We aimed to collect quantitative data in this range, and to study if the cerebral artery tree complies with the principle of minimal work (Law of Murray).

To enable easy quantification of branching patterns a semi-automatic method was employed to measure 1294 bifurcations and 2031 segments on 7T-MRI scans of two corrosion casts embedded in a gel. Additionally, to measure segments with a radius smaller than 0.1mm, 9.4T-MRI was used on a small cast section to characterize 1147 bifurcations and 1150 segments. Besides MRI, traditional methods were employed. 733 bifurcations were manually measured on a corrosion cast and 1808 bifurcations and 1799 segment lengths were manually measured on a fresh dissected cerebral arterial tree.

Data showed a large variation in branching pattern parameters (asymmetry-ratio, area-ratio, length-radius-ratio, tapering). Part of the variation may be explained by the variation in measurement techniques, number of measurements and location of measurement in the vascular tree. This study confirms that the cerebral arterial tree complies with the principle of minimum work. These data are essential in the future development of more accurate mathematical blood flow models.

Introduction

Blood flow modelling could aid in better understanding of hemodynamics in many cerebrovascular diseases such as aneurysms, vascular dementia, moyamoya vasculopathy and stroke. However, for cerebrovascular blood flow modelling to be successful, clear morphological knowledge of the cerebral arterial tree is needed.[1] This tree spans from the circle of Willis, which is known to be highly variable, up to the capillary network.[2–4] The main branches of the circle of Willis each form a large arterial tree, supplying different and variable vascular territories of the brain.[5,6]

Morphological data on vascular trees are traditionally expressed by branching patterns described by mathematical relations between parent and daughter arteries at bifurcations as well as diameters and lengths of intermediate vessel segments.[7,8]

In addition, it is generally accepted that the morphology of the cerebrovascular tree follows the principle of minimum work as described by Murray.[9] This principle is expressed by the equation $r_0^3 = r_1^3 + r_2^3$, where according to convention r_0 is considered to be the radius of the parent artery and r_1 and r_2 of both daughter arteries.[7,10,11] Morphological data confirming that the cerebral arterial tree adheres to this principle of minimum work are therefore essential and we believe this could aid in optimization of models for the human vasculature and ease hemodynamic flow modelling.[12]

In the past, data of branching patterns of an arterial tree were gathered using manual measurements on *ex vivo* and *in vivo* specimens.[7,8,13–19] More modern techniques utilize newer three dimensional (3D) imaging techniques such as computed tomography angiography (CTA) and Magnetic Resonance Imaging (MRI) for *in vivo* capturing of larger arteries and micro-computed tomography (micro-CT) and confocal laser microscopy for capturing highly detailed *in* and *ex vivo* vascular networks.[13,20,21]

To our knowledge, information on the branching pattern of the human intracranial cerebral arterial tree is still limited. Also information is limited on whether the human cerebral arterial tree complies to the principle of minimum work as described by Murray.[10,18,22–25] Most studies performed measurements on arteries larger than one millimetre[18,23] whereas others studied only the microvasculature.[13,26] Data on vessels with intermediate sizes (30 μm – 1 mm) are scarce.

High resolution MRI scanning of corrosion casts has the potential to increase our knowledge on morphology in the smaller segments of the vascular tree (See chapter 4). The current study aims to add quantitative data on the branching pattern of the human cerebral arterial tree in the missing range between larger cerebral arteries and the capillary network by applying this new MRI based method using 7T and 9.4T MRI. Because MRI based methods are still relatively new, we also performed manual measurements on corrosion cast and dissection that will be presented along the MRI data as reference. This data could be used in future models of the cerebral arterial tree.[1] The data of the branching patterns are used to assess whether the human cerebral tree keeps the principle of minimum work as defined by the Murray's law.

Materials and Methods

General study design

Four measurement techniques were used. The first two techniques were earlier described 7T MRI and 9.4T MRI technique to quantify a large number of vessels in radius range of 0.1-1.0 mm and 30-200 µm respectively (See chapter 4). Third, manual measurements on a pressurized vascular cast were performed. Finally, vessel diameters of a freshly dissected human arterial tree were measured.

Brains used in the current study were derived from bodies that were donated to the Department of Anatomy. From these persons written informed consent was obtained during life that allowed the use of their entire bodies for educational and research purposes. As this research complies with the given written informed consent, in accordance with the Dutch law on dead bodies, no further IRB approval was required.

Casts

Preparation

For 7T MRI two full casts were produced (one male, 50 years and one female, 78 years). For 9.4T RMI a third cast (female, 57 years at 9.4T MRI) was produced from which only a small section was used (Figures 1a and 1b). For manual measurements a fourth full cast (female, 89 years) was produced and cut in smaller segments. None of the 4 used brains showed signs of pathology after harvesting and all were fully intact. The casts were created by the injection of a mixture of Araldite F/hardener HY 2967/dilutioner DY 026 SP through cannulas in the six major cerebral arteries of the brain under controlled pressure. The brains were subsequently corroded. This procedure was previously described in detail.[27]

MRI (7T and 9.4T)

MRI scanning and preparation

MRI protocols and post-processing were previously described (See chapter 4). In summary, to prepare for MRI scanning two complete casts of the cerebral circulation (7T MRI) and a small section of another cast were embedded in solution of gelatine (14%, powder, Sigma-Aldrich, Saint Louis, Missouri, USA) and a gadolinium-containing contrast agent (2.8*10^-3 mL contrast agent / mL water; Gadobutrol, Gadovist 1.0mmol/mL, Bayer Schering Pharma, Newbury, UK) in water, and subsequently placed in a custom made PCV container (7T MRI) or Perspex container (9.4T MRI)(Figure 1c). Next, 7T MRI was performed on a whole-body system (Philips Healthcare, Cleveland, OH, USA) with a 60 cm bore diameter. The acquired voxel size was of 0.1x0.1x0.1mm^3. 9.4T MRI was performed on a 9.4T/21cm MR system (Varian Inc. Palo Alto, CA, USA) with an acquired voxel size of 30x30x30 µm^3.(see figure 2 for example of MRI data)

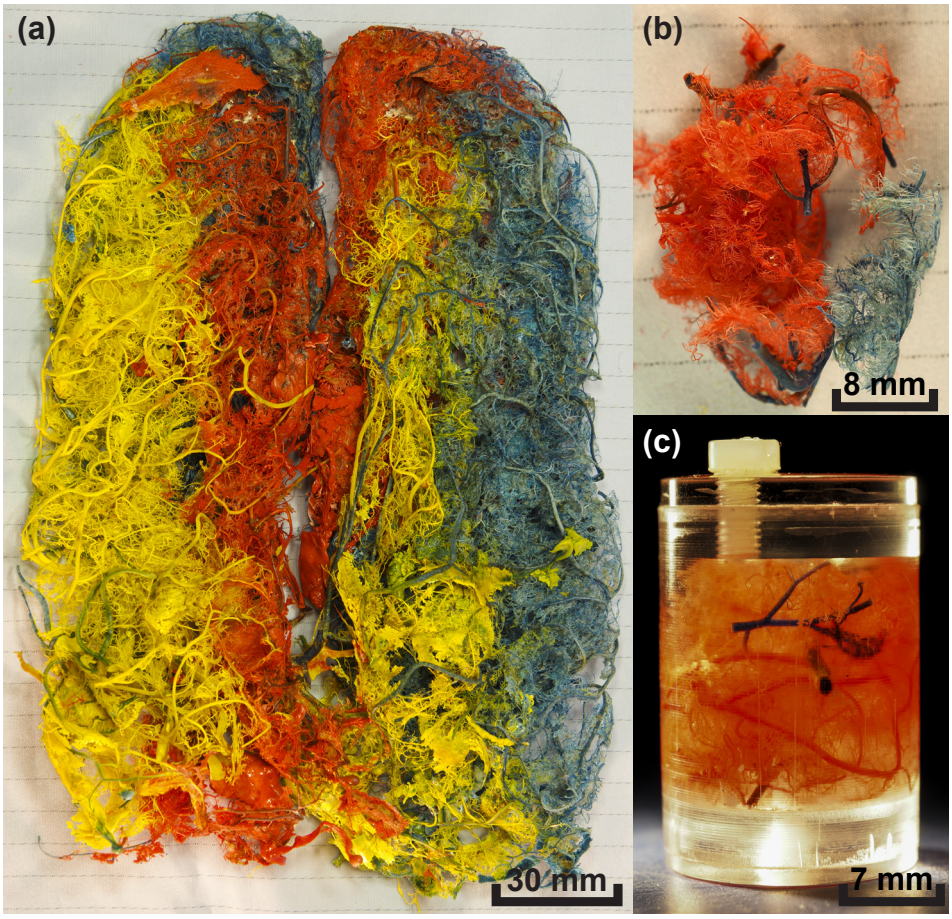

Figure 1: Examples of the casts.

(a) Photograph of one of the plastic casts of the full cerebral arterial circulation, as was used in the 7T MRI. Different colour pigments where used for the six major cerebral arteries. (b) Photograph of a small section of the casts as was used in the 9.4T MRI. (c) Photograph of the same small section of casts for the 9.4T MRI placed in the gadolinium-gelatine solution in a Perspex container.

To create the 3D reconstruction, a semi-automatic segmentation method was used in which the user manually selects locations along the arterial tree. Between these locations centrelines were traced. These centrelines consist of many separate connecting nodes at which for each node the radius was calculated using a full-with-at-halve maximum method.

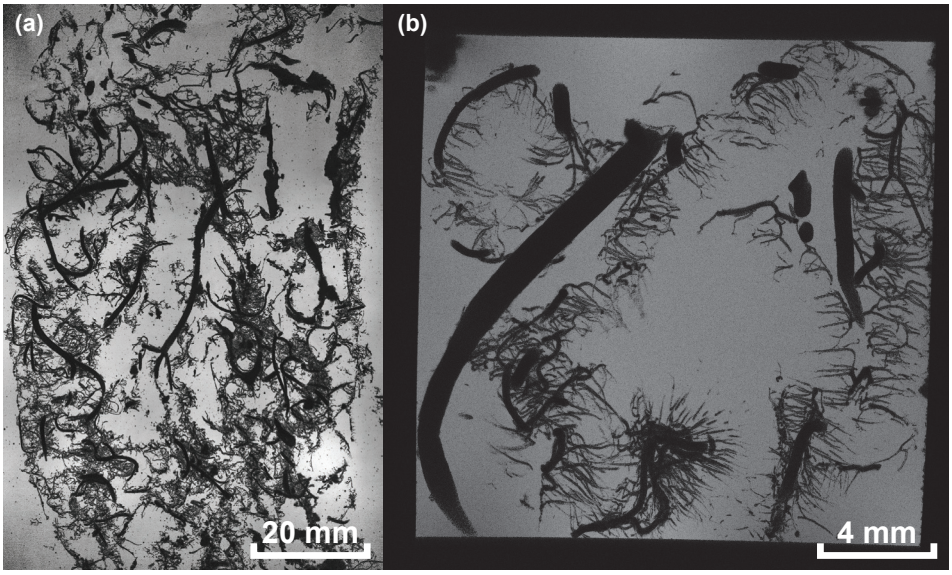

Figure 2: Example MRI data.
(a) Minimum intensity projection of 20 slices (1.95mm total thickness) of 7T MRI data. (b) Minimum intensity projection of 100 slices (1.50mm total thickness) of 9.4T MRI data.

Calculation of radii and lengths

The arterial trees acquired by MRI scanning were split in separate segments between bifurcations. For each segment length, proximal radius and distal radius were calculated using a custom MatLab code (version R2014a (8.3.0.532), The Mathworks, Inc). Each segment consists of many separate nodes with respective radii. To calculate a representative radius at the proximal and distal side of the segments a method had to be devised. The first and last quartiles of nodes of each segment were not used as it is known that just after and before a bifurcation the radius decreases and doesn't portraits the actual radius of a segment.[15,28] Using the radius of the nodes of the middle quartiles and their Euclidian distance from the start of the first node, a linear regression analysis was performed. Based on this linear regression analysis the proximal and distal radius were calculated. Length was calculated as the sum of all Euclidean distances between all nodes forming one segment.

Segments with a proximal diameter smaller than two voxel size and bifurcations with parent or daughter arteries with a diameter smaller than two voxel size were excluded from further analysis as two voxels are required to more accurately calculate diameters.[29] Finally this resulted in a database with length, radii and connective information for each segment in the arterial tree based on MRI data. Data of both 7T MRI casts were combined for ease of further calculations.

Manual measurements

Subsequently one cast was divided in smaller sections. On each section the diameters of parent and both daughter arteries were measured for every accessible bifurcation using a digital caliper under a microscope (OPMI-1, Carl Zeiss Meditec Inc., Dublin, California, USA, magnification 10-40x). Manual measurement of lengths on our casts was technically not possible.

Dissection

Brain preparation

A fresh human cadaver (male, 71 years) was decapitated within 24 hours post-mortem. Both common carotid arteries and vertebral arteries were cannulated and flushed with laundry detergent dissolved in water at room temperature (6-8 grams/litre. OMO Professional, Unilever N.V., Rotterdam, The Netherlands) until clear fluid returned through the internal jugular veins. Next a mixture of water, 20% gelatine and a 5% red gouache paint (Ecola, Royal Talens, Apeldoorn, The Netherlands), which would aid in subsequent dissection, was injected until the mixture clearly returned through the venous system. To prevent the gelatine paint mixture from leaking out of the vasculature, clamps were placed on the carotid and vertebral arteries, jugular veins and other collateral cervical veins and arteries showing leakage of fluid. Finally, the head was submerged in cold (5 degrees Celsius) laundry detergent solution (6-8 grams/litre) and placed overnight in the refrigerator at 5 degrees Celsius for gelatine to solidify.

Dissection method

The brain was obtained by cutting its connecting structures to the skull base after removal of the skull cap. Next, the cerebellum was removed from the brain by a cut through the pons. The circle of Willis was identified. The six major cerebral arteries were cut at the level of the circle of Willis and their respective arterial tree dissected to the level of arteries with a diameter of roughly 200-300 μm. Dissection was performed using an operating microscope (OPMI 6-CFC, Carl Zeiss Meditec Inc., Dublin, California, USA, magnification 10-40x). Dissected arterial trees were stored at 5 degrees Celsius in a mixture of laundry detergent and formaldehyde (6-8 gram/litre OMO professional, 0.3-0.5% Formaldehyde).

Measurement method

First the gelatine paint solution was removed from the arterial tree by spreading the arterial tree (Figure 3) on a flat surface and carefully manipulating the gelatine in the direction of greater diameter arteries. Next the diameters of each bifurcation and lengths between bifurcations were measured.

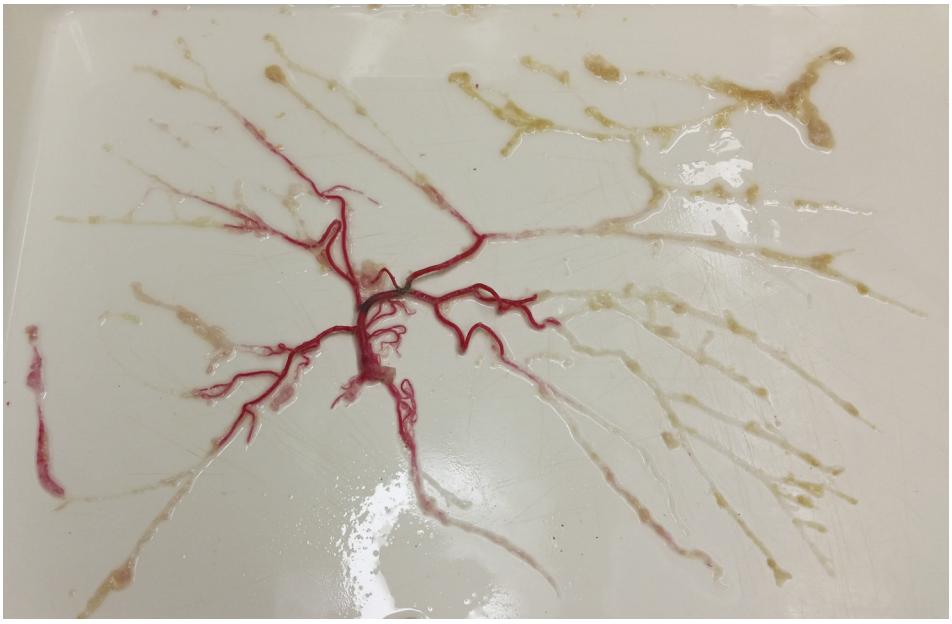

Figure 3: Dissected cerebral arterial tree of the right middle cerebral artery spread out on the table. Arteries are still partially filled with the gelatine-red paint solution.

Measurements of radius were done as described in more detail by Hillen et al.[4] In summary, the arteries were flattened on a flat surface under a clear glass microscope slide. The width of the flattened vessel was measured on top of this microscope slide using a digital caliper. Next the vessel wall thickness was determined on the same location as where the width was measured by flattening the artery between de tips of the digital caliper just until the tips started to indent the arterial wall. Using this width and vessel wall thickness the radius was calculated according to

$$radius = \frac{width - 2 \times vesselwall}{\pi}$$

For measurement of lengths, segments between bifurcations were carefully stretched until straight and subsequently measured using a digital caliper.

All measurements were performed under the same operating microscope mentioned above. Measurements of radius and length were all performed twice and averaged to mitigate measurement errors.

Data Analysis

Statistical analysis and definitions

Definitions for different parameters in the branching patterns of the cerebral arterial tree that were of interest to the current study are displayed in table 1. The lenght-to-radius ratio (LR) and tapering (T) were calculated from dissection- and MRI-data only as measurement of length was not feasible by manual cast measurements. From the data using MRI, the branching pattern parameters were calculated using MatLab. From the direct measurements on cast and dissection, these calculations were performed using Microsoft Excel 2013 (version 15.0.4745.1000, Microsoft Corp.)

A Kolmogorov-Smirnov (KS) test was used to check normal distribution. In case the data was not normally distributed, the median, interquartile range (IQR) and range of measurements were reported, and histograms were made.

Linear regression analysis was performed to analyse the area-ratio (AR) and the principle of minimum work. For (a) AR: regression was performed between the squared radius of the parent artery and the sum of the squared radii of all daughter arteries. The slope of this regression analysis would be the AR. (b) For the principle of minimum work: regression was performed between the cubed parent artery radius and the sum of cubed radii of all daughter arteries, where a slope of equal to one would mean the overall cerebral tree complies to the principle of minimum work. The robust regression and outlier removal (ROUT) as described by Motulsky et al.[30] was implemented in GraphPad Prism (version 6.01, GraphPad Software, Inc. La Jolla, CA, USA), and used with a Q value of 1% to select and remove outliers. No outliers were removed from data on asymmetry ratio (AS) due to the fact that these values are limited in a range between 0 and 1. All statistical analyses were performed using GraphPad Prism. The datasets generated during and/or analysed during the current study and MatLab scripts are available from the corresponding author on reasonable request.

Definition	Description
Bifurcation/trifurcation	location where an artery splits into two/three separate arteries
Segment	piece of artery between two bifurcations
Parent artery	inlet artery of a bifurcation. r_0 represents the radius of the parent artery
Daughter artery	outflow artery of a bifurcation. r_1 and r_2 represent the radii of the two daughter arteries, where according to convention r_1 is the largest radius
Proximal artery radius	radius at the proximal (upstream) side of a segment between two bifurcations
Area ratio (AR)	the ratio between the cross-sectional area of the parent artery and the sum of the cross-sectional area of all daughter arteries. This is for bifurcations calculated as: $AR = \frac{\pi r_1^2 + \pi r_2^2}{\pi r_0^2}$
Asymmetry ratio (AS)	the ratio between the cross-sectional areas of the smallest daughter artery (πr_2^2) and the the largest daughter artery (πr_1^2). This ratio can only be calculated for bifurcations and not for junctions with more than two daughter arteries such as trifurcations: $AS = \frac{\pi r_2^2}{\pi r_1^2}$
Length-to-radius ratio (LR)	The LR was defined as the length (L) of an arterial segment divided by its radius at the proximal end ($r_{proximal}$) of this segment. $LR = \frac{L}{r_{proximal}}$
Tapering (T)	the ratio between the radius at the distal end (r_{distal}) of a segment and the radius at the proximal end ($r_{proximal}$) of a segment. $T = \frac{r_{distal}}{r_{proximal}}$
Principle of minimum work	according to Murray(Murray, 1926b). Defined as: $r_0^3 = r_1^3 + r_2^3$ For analysis whether a bifurcation complies with this principle this formula was rewritten as: $\frac{r_1^3 + r_2^3}{r_0^3} = n$ If n equals 1 a respective bifurcation complies with the principle of minimum work.

Table 1: Definitions.

Results

Lengths and radii of segments

Table 2 shows the data on parameters. None of the parameters was normally distributed. A total of 1294, 1147, 733 and 1808 bifurcations were available for analysis for 7T MRI, 9.4T MRI, manual cast and dissection data respectively. A total of 2031, 1150 and 1799 segments were available for analysis of the 7T MRI, 9.4T MRI and dissection data respectively. Figure 4 shows the distribution of the parent artery radius (Figure 4 top), the proximal radius (Figure 4 middle) and length (Figure 4 bottom).

Between the different methods used to acquire data, there was a difference in distribution of included arterial diameters (Table 2 and Figure 4 top and middle). Data from manual measurement on casts included larger arteries (median 0.5 mm range: 0.09-1.61) compared to dissection and 7T MRI data (median 0.41 mm range: 0.10-1.41). 9.4T MRI data included only small arteries up to the pre-capillary network (median 0.12 mm range: 0.04-0.67).

Branching patterns

Parameters characterizing the branching patterns are summarized in *table 3* and histograms in figure 5. None of the resulting branching patterns were normally distributed. All branching patterns showed a broad distribution (Figure 5). For data obtained from the MRI measurements, this spread in branching patterns seemed to be larger for the AR. The median AS turned out to be larger in MRI data then from manual measurement results. Linear regression analyses of the AR are shown in figure 6. Linear regression analyses for the principle of minimum work according to the Law of Murray are shown in figure 7. The AR showed a larger IQR in the two casts that were used for MRI, compared to the AR measured in the cast that was used for manual measurements (Table 3). Linear regression analysis (Figure. 6) showed a larger slope for MRI data for AR. LR data showed a lower median value for MRI data then for dissection data. Median values for tapering were 0.99 for both MRI techniques and dissection (Table 3). Regression analysis (Figure. 7) on dissection data shows a slope close to one (1.04±0.01, R^2=0.97, p<0.0001) confirming the principle of minimum work while the slope for manual measurements on the casts is smaller than one with a value of 0.9±0.01 (R^2=0.96, p<0.0001) and for 7T MRI and 9.4T MRI are larger than one with slopes of 1.13±0.04 (R^2=0.73, p<0.0001) and 1.36±0.02 (R^2=0.85, p<0.0001) respectively.

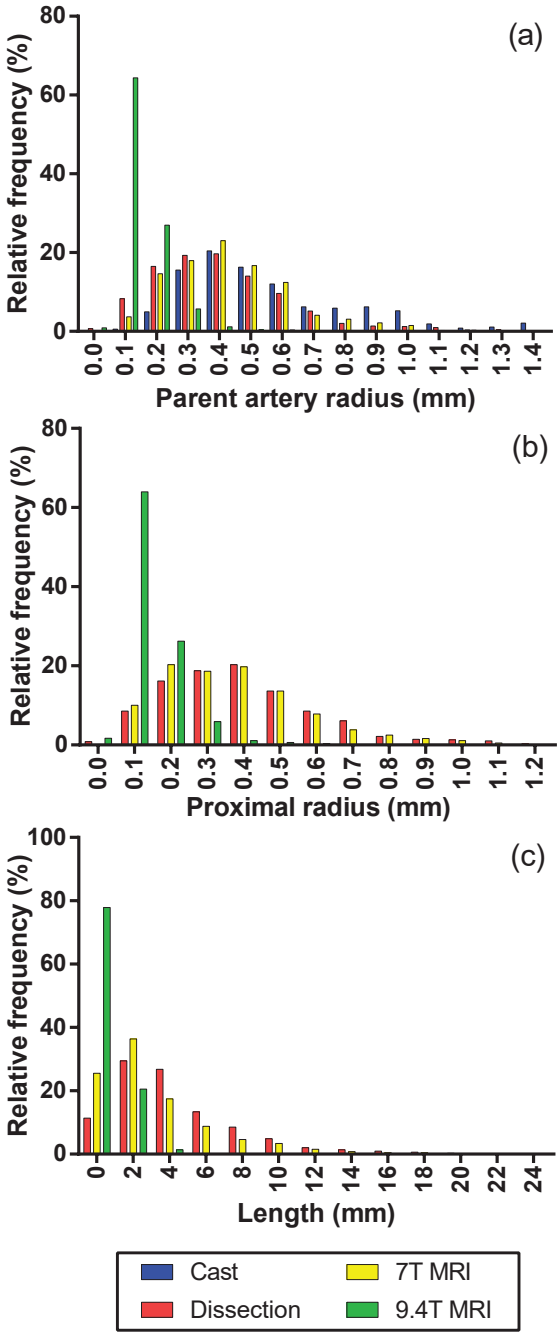

Figure 4: Relative frequencies in percentage (%).

Top: parent artery radius in millimetres (mm) for bifurcations, *middle*: proximal radius in mm for segments, *bottom*: Length for segments in mm.

Source	Bifurcations/ segments (n)	Parent artery radius (mm)	Proximal artery radius (mm)	Length (mm)
Cast	733	0.50 (0.35, 0.09-1.61)		
Dissection	1808/1799	0.37 (0.27, 0.03-1.59)	0.38 (0.27, 0.02-1.60)	3.60 (4.13, 0.13-35.68)
7T MRI	1294/2031	0.41 (0.24, 0.10-1.41)	0.36 (0.26, 0.10-1.50)	2.20 (3.40, 0.00-41.53)
9.4T MRI	1147/1150	0.12 (0.08, 0.04-0.67)	0.13 (0.08, 0.03-0.69)	0.49 (0.67, 0.00-5.68)

Table 2: General results.
Radii are reported as median radius in millimetres (mm) with interquartile range (IQR) and range: median (IQR, range).

	AR	AS	LR	Tapering
Cast	1.16 (725, 0.22, 0.57-1.81)	0.44 (733, 0.47, 0.00-1.00)	NA	NA
Dissection	1.05 (1733, 0.19, 0.51-1.61)	0.09 (1808, 0.26, 0.00-1.00)	10.49 (1681, 12.17, 0.22-42.38)	0.99 (1745, 0.09, 0.71-1.27)
7T MRI	1.38 (1252, 0.84, 0.07-3.71)	0.68 (1293, 0.40, 0.11-1.00)	6.82 (1854, 10.03, 0.00-29.58)	0.99 (1910, 0.11, 0.55-1.43)
9.4T MRI	1.45 (1123, 0.77, 0.05-3.63)	0.78 (1146, 0.27, 0.17-1.00)	4.24 (1098, 5.83, 0.00-17.45)	0.99 (1065, 0.08, 0.70-1.27)

Table 3: Branching patterns of manual measurements on cast and dissected arteries and measurements using 7T MRI and 9.4T MRI.
Values are all median (number without outliers, interquartile range, range). NA = not applicable, AR = area ratio, AS = asymmetry ratio, LR = length-to-radius ratio.

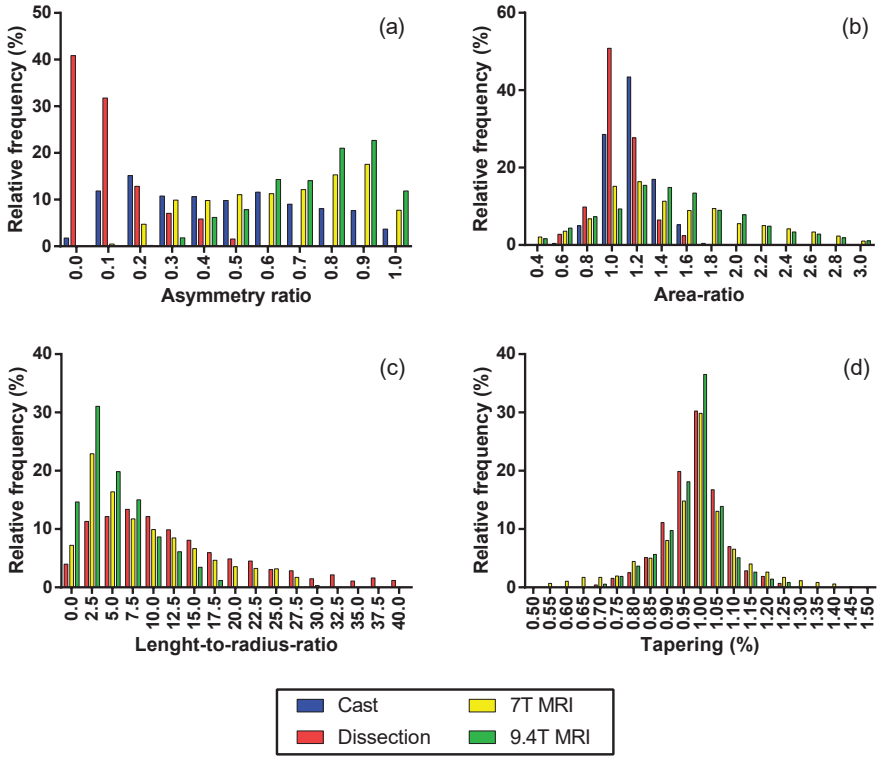

Figure 5: Relative frequencies

(a) asymmetry ratio, (b) area ratio, (c) length-to-radius-ratio (d) tapering.

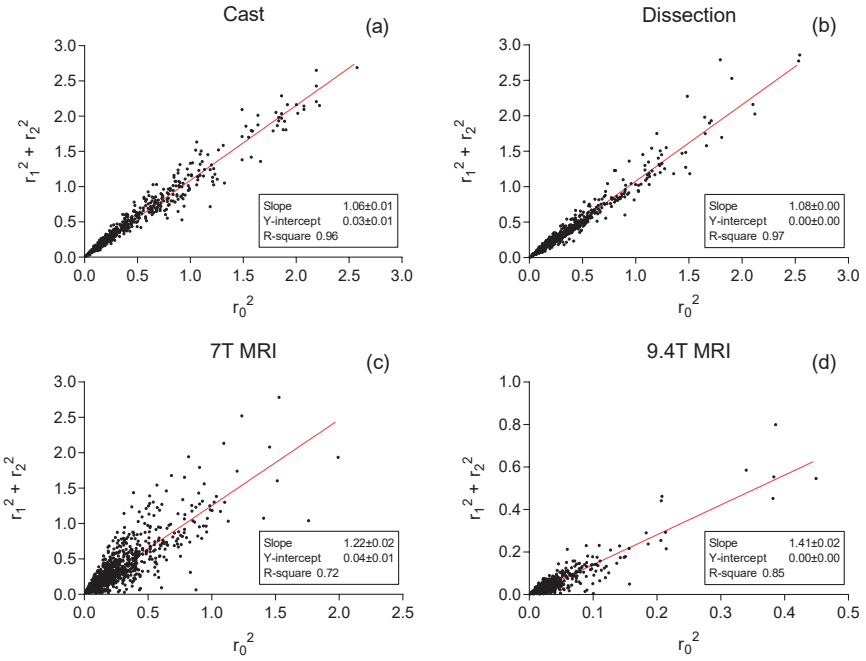

Figure 6: Area ratio.

Scatterplots of squared parent artery radius (r_0) versus sum of squared radii (r_1, r_2) of all daughter arteries for (a) cast, (b) dissection, (c) 7T MRI and (d) 9.4T MRI.

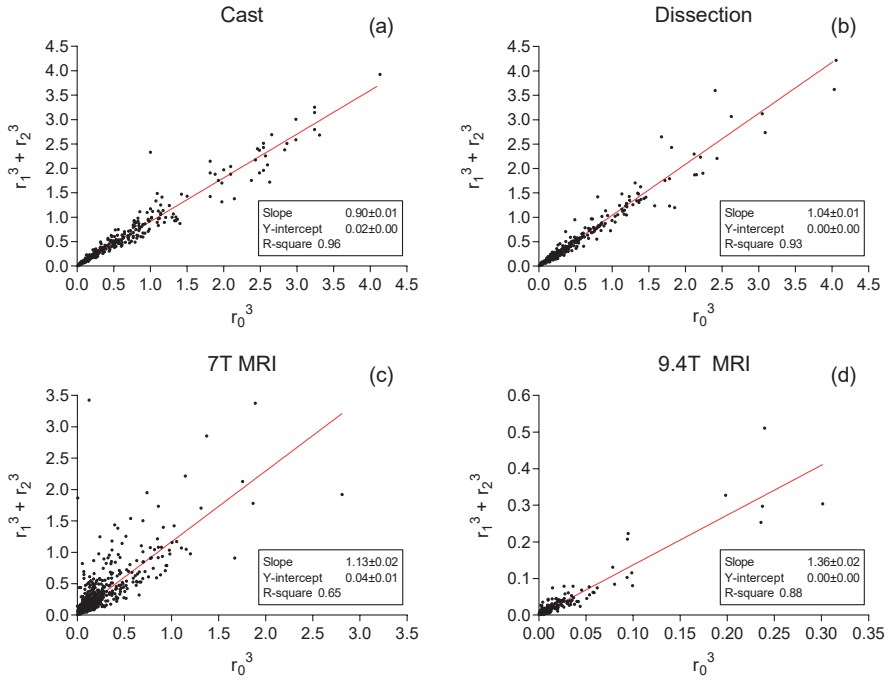

Figure 7: Principle of minimum work according to Murray.

Scatterplots of cubed parent artery radius (r_0) versus sum of cubed radii (r_1, r_2) of all daughter arteries for (a) cast, (b) dissection, (c) 7T MRI and (d) 9.4T MRI.

Discussion

To our knowledge this is the first study which shows branching patterns in the radius range between larger cerebral arteries (>1 mm) and the microvascular network (<100 μm). In the current study both 7T MRI and 9.4T MRI techniques were used. These techniques allowed for faster quantification than when done using manual measurement techniques and allowed characterization of a larger sample size and range than when solely a high resolution technique like micro-CT, confocal microscopy, stained histology slices or 9.4T MRI scanning would have been used.[13,15,21,31–37] Manual measurements on cast and dissected arteries were also performed to enable comparison to traditional techniques as MRI and reconstructive techniques are still relatively new in characterization of arterial branching.[1]

The data generated might be valuable for use in modelling of the cerebral arterial tree, which could improve understanding of different cerebrovascular diseases as it would ease hemodynamic blood flow modelling.[1,38–40] Data on tapering as presented could be of importance for pulse wave propagation modelling. The major sites for pulse wave reflection are thought to be at branching points and taper of arteries and arterioles. By confirming the lack of tapering the current data indicate that including tapering in modelling is not necessary.[41,42] Besides branching patterns, the current study presents data on whether the cerebral arterial tree complies with the optimality principles as described by Murray in the law of minimum work. These optimality principles in turn are used in models like tissue metabolism driven arterial tree generation.[43]

Main findings of the study

A large dataset containing bifurcations and segments of the human cerebral arterial tree was created, enabling quantification of branching patterns.

Asymmetry-ratio

There is a broad range in AS for all four methods. This shows that in the cerebral circulation bifurcations of various symmetries are present. Further there is a striking difference in AS in all four methods. With the lowest median AS of 0.09 for dissection and the largest of 0.78 for 9.4T MRI. This difference might be explained by the number of included smaller side branches. The cerebral circulation is known to have many small side branches bifurcating in a sharp angle from the main arteries.[44,45] With a voxel resolution of 0.1 mm for 7T MRI, the maximum radius of a measurable artery is 0.1 mm, hence these smaller side branches are not detected with the 7T MRI technique.

The same principle applies for the 9.4T MRI. The manual cast measurements also show a higher AS (0.44) than the measurements on the dissected vessel tree. This may be the result of the finding that the smaller side branches of the cast are too small to measure by hand without breaking them.

Hence AS in the current study is probably more a reflection of the amount of included smaller side branches. The AS of the dissection data might reflect the actual AS of the cerebral circulation as we believe the smaller side branches were lost.

Area-ratio

The current study shows a large range in AR with an increasing AR when smaller arteries, closer to the microvasculature, are included. This matches well with results from literature.

Based on the principle of minimum work the AR would range between 1.10 for turbulent flow in larger arteries and 1.26 for laminar flow in smaller arteries.[46] From literature we know that in the human vasculature the range of AR is much larger than this theoretical range.[17,20,28,47–49]

The wide range in AR found in the current study (between a median 1.05 and 1.45) might be partially explained by the difference in included side branches as reflected in the AS. Inclusion of small side branches will lead to a decrease in AR as those small branches only slightly increase the cross-sectional area at those. As MRI data included less small side branches an increased AR can be expected when compared to manual measurements on dissected arterial trees. Additionally, it is expected when getting closer to the capillary circulation there will be less smaller side branches which will further increase AR. The 9.4T MRI data included arteries close to the arteriole network and showed the highest AR of 1.45. This increasing trend in AR when including smaller arteries matches well with an even higher AR of 1.52 as shown by Cassot et al. who measured the cerebral microcirculation (mean±SD diameter 6.91±3.85 micrometres) in 9414 bifurcations in India ink-injected human brains.[26]

Other studies show that the larger arteries of the cerebral circulation have indeed tendency of a lower AR. Rossitti et al. studied 176 bifurcations on angiogram data with an AR of 1.2±0.4.[18] They included only arteries greater than 1 mm in diameter. Ingebrigsten et al. performed measurements on 69 3D angiograms of the larger bifurcations of the ICA, basilar artery (BA) and MCA for which the mean±SD AR were respectively 0.8±0.2, 0.7±0.4 and 1.2±0.3.[23]

Principle of minimum work

The data of the current study, combined with the already existing data in literature indicate that there is a large spread between different parts of the circulation and possibly between different subjects in regard to the principle of minimum work.[18,19,22–25,50] However, when including most side branches the cerebral circulation seems to follow the principle of minimum work.

Traditionally studies calculate the exponent of the equation $r_0^x = r_1^x + r_2^x$ for minimum work as defined by Murray. Theoretically the exponent would be 2.33 in case of fully turbulent flow and 3 in case of fully laminar flow.[46,51] However, solving *x* in this equation is only possible by numerical methods and can result in values of plus or minus infinity as discussed by Sherman et al.[11] Hence, in the current paper we chose the alternative by performing a simple regression analysis of the ratio between the cubed parent artery radius and the sum of the cubed daughter artery radii. The closer the slope to a value of one is, the more the arterial tree the principle of minimum work for laminar flow follows. The slopes as shown in figure 4 were 1.13±0.02, 1.36±0.02, 0.90±0.01, 1.04±0.01, for 7T, 9.4T, manual cast and dissection respectively.

Again, for the principle of minimum work the inclusion of small side branches, as reflected in the AS, might influence this ratio. For the dissection data, which most likely included most side branches, the slope was almost equal to 1 with a very good fit of the regression analysis (R^2 = 0.96). This might confirm that the cerebral circulation follows the principle of minimum work.

Only a few other studies performed a comparable regression analysis to confirm the principle of minimum work as done in the current study. In two studies of human cerebral[18] and retinal[50] arteries linear regression analysis demonstrated slopes of 0.87±0.07 (mean±SD) and 0.98. In a histological study by Wang et al. on 150 mice brain (366 bifurcations) the linear fit did not differ significantly from 1, showing that the mice cerebral circulation follows the principle of minimum work.[19]

Most studies that calculated the exponent also demonstrate that the cerebral circulation shows a large range but follows the principle of minimum work. Suwa et al. showed for arteries greater than 0.1 mm in 2 human brains an exponent of 2.67 and 2.79.[25] Ingebrigsten et al. analysed 3D angiograms of 69 human patients and found an exponent of 1.7±0.8, 1.2±0.3 and 2.9±1.2 for the major bifurcations of the ICA, basilar artery and MCA respectively.[23] In a study by Mut et al. which analysed MRI's (voxel size 0.6x0.6x0.6 mm) of 61 human brains and found an exponent of 2.5.[24] Cassot et al. showed an exponent of median 3.58 (IQR 2.29-6.14, range 0.662-1947, 9414

bifurcations) for the cerebral microvasculature.[22] Rossitti et al., who analysed 12 angiograms of 10 adult patients, found an exponent of 2.9±0.7 (for 157 bifurcations) for the ICA, ACA and MCA for arteries larger than 1 mm in diameter.[18]

Length-radius-ratio

LR was only acquired by dissection and both MRI techniques, as measurements of length on cast by manual techniques are not accurately possible. LR values for dissection and 7T MRI data ranged from values close to 0 to almost 43. 9.4T MRI showed LR values of 0 to almost 18. Median values were 6.82, 4.24 and 10.49 for 7T MRI 9.4T MRI and dissection respectively. These values found in the current study were lower than those described in literature, but showed a comparable range. As with the other branching patterns LR might also be depending on the inclusion of small side branches. However, in mathematical flow models the length of the segments is of less influence on flow, as radius has the greatest impact on resistance for flow.

In literature Iberall et al. estimated that for the cardiovascular system a good LR would be 50±10.[23] Koike et al. measured a LR of 9 on resin casts of the arterial tree of six dog lungs.[8] Based on data of Cassot et al. and Lauwers et al. the LR for the human cerebral microvasculature would lie between 10.1-16.4 depending on whether median or mean values are used for calculation.[13,34] Rai et al. measured the length and diameter of 100 human patients using CTA of the proximal cavernous ICA, the ICA terminus, the MCA origin and the M2 origin returning an LR of 13.4 and 13.1 for men and women respectively for ICA, and for MCA 15.3 and 14.1 for men and women.[52] Finally, in a Scanning Electron Microscopy study of capillaries of rat brain, lengths and diameters were published from which an LR of 30.5 (range 2.1-53.2) could be calculated.[35]

Tapering

Tapering showed median values of 0.99 for dissection and both MRI techniques, indicating that there is no significant tapering. However, tapering, just as the other branching patterns, showed a large range with values between 0.55-1.43, 0.70-1.27 and 0.71-1.27, for 7T MRI 9.4T MRI and dissection respectively.

To our knowledge there are no quantitative data on tapering of the cerebral arterial tree in literature. Based on the principle of minimal work one would expect that tapering is not present. This is confirmed by the current data.

Limitations

This study has several limitations: (a) for the different methods samples of different subjects were used. The differences in branching patterns found among the techniques in the current study might be caused by the usage of samples of different subjects. Since it is not known if the differences found are solely due to an inter-subject variability, due to difference in technique or as suggested above, due to the difference in included smaller side branches. (b) A second limitation is the change in vascular muscle tone post-mortem. It is known that post-mortem the arterial smooth muscle relaxation and contractility change.[53,54] This change could have an impact on cast production and radius measurements performed on dissection material. (c) The method used to store the dissected arteries could have influence on the diameters and lengths measured. In literature there are indications that tissue, when fixed using formalin, results in shrinkage of tissue which might impact measurements performed in the current study.[55,56] OMO laundry detergent could show a comparable effect, but this is unknown. (d) Another limitation mainly having effect on length measurements in dissection is the loss of axial stretch. When removing arteries using dissection their respective length is shortened by axial elasticity. To perform length measurements in dissection the arteries were stretched until straight, which would likely have caused inaccuracy in the length measurements. (e) For measuring the radius on dissected arteries both the width of a compressed artery and its arterial wall are measured. From these the radius is calculated. This method might introduce additional systematic error. (f) Although there were no neuropathological defects visible on inspection of the brains used, age of the subjects might have had an effect on the morphology and branching patterns of the cerebral arterial tree. (g) Lastly there was a difference in pressure at which the Araldite F mixture was injected in the casts used for manual measurement and MRI scanning. For the manual measurement cast pressure was controlled at a static pressure of 93 mmHg until solidification was complete. However, for the MRI, casts from a previous unpublished study were used, in which pressure was of less importance as only complete penetration of the cerebral circulation up to the level of the capillaries was required. This could have resulted in a difference in pressure during production, which might impact the radius of the arteries. However as shown in a study by Guo et al. the inner radius of arteries show less increase in radius at increasing pressures.[57] We expect the required pressure to result in adequate Araldite-F penetration to be around the level at which the increase in radius with increasing pressure is only minimal. Hence diameters should not differ much between the casts for manual cast measurements and casts used for MRI measurements due to possible difference in pressure during production of the casts.

It is however questionable if these limitations have a major and significant effect on the results and conclusions

In conclusion, to our knowledge this is the first study to show data of branching patterns in this range (0.1-1.0 mm diameter) of arteries of the human cerebral arterial tree. The current data on branching patterns show, as other authors have done previously in the cerebral microvasculature, such a large spread that these branching patterns can only be interpreted as general trends.[26] It is of importance that models take this large spread and variation throughout the cerebral arterial tree into account. Finally, the current work shows indications that on a macroscopic scale the cerebral arterial tree follows the principle of minimum work as described by Murray and that the reduction of radius of cerebral arteries occurs predominantly at the level of bifurcations rather than along segments between bifurcations.[10]

Acknowledgements

We would like to thank W.J.A. van Wolferen from the department of anatomy university medical centre Utrecht for his help in brain dissection and H. Kruijf from the image science institute Utrecht for his help in 3D reconstruction of 7T MRI data.

References

1. Hirsch, S., Reichold, J., Schneider, M., Székely, G. & Weber, B. Topology and hemodynamics of the cortical cerebrovascular system. *J. Cereb. Blood Flow Metab.* **32,** 952–67 (2012).
2. Alpers, B. J., Berry, R. G. & Paddison, R. M. Anatomical studies of the circle of Willis in normal brain. *A. M. A. Arch. Neurol. psychiatry* **81,** 409–418 (1959).
3. Hartkamp, M. J., van der Grond, J., van Everdingen, K. J., Hillen, B. & Mali, W. P. T. M. Circle of Willis Collateral Flow Investigated by Magnetic Resonance Angiography. *Stroke* **30,** 2671–2678 (1999).
4. Hillen, B. The variability of the circle of Willis: univariate and bivariate analysis. *Acta Morphol. Neerl. Scand.* **24,** 87–101 (1986).
5. van der Zwan, A. & Hillen, B. Review of the variability of the territories of the major cerebral arteries. *Stroke* **22,** 1078–84 (1991).
6. van der Zwan, A., Hillen, B., Tulleken, C. A., Dujovny, M. & Dragovic, L. Variability of the territories of the major cerebral arteries. *J. Neurosurg.* **77,** 927–40 (1992).
7. Zamir, M. On fractal properties of arterial trees. *J. Theor. Biol.* **197,** 517–26 (1999).
8. Koike, K., Ohnuki, T., Ohkuda, K., Nitta, S. & Nakada, T. Branching architecture of canine pulmonary arteries: a quantitative cast study. *Tohoku J. Exp. Med.* **149,** 293–305 (1986).
9. Murray, C. D. The Physiological Principle of Minimum Work: I. The Vascular System and the Cost of Blood Volume. *Proc. Natl. Acad. Sci. U. S. A.* **12,** 207–14 (1926).
10. Murray, C. D. The physiological principle of minimum work applied to the angle of branching of arteries. *J. Gen. Physiol.* **9,** 835–41 (1926).
11. Sherman, T. F. On connecting large vessels to small. The meaning of Murray's law. *J. Gen. Physiol.* **78,** 431–53 (1981).
12. Gabryś, E., Rybaczuk, M. & Kędzia, A. Blood flow simulation through fractal models of circulatory system. *Chaos, Solitons and Fractals* **27,** 1–7 (2006).
13. Cassot, F., Lauwers, F., Fouard, C., Prohaska, S. & Lauwers-Cances, V. A novel three-dimensional computer-assisted method for a quantitative study of microvascular networks of the human cerebral cortex. *Microcirculation* **13,** 1–18 (2006).
14. Horsfield, K. & Woldenberg, M. J. Diameters and cross-sectional areas of branches in the human pulmonary arterial tree. *Anat. Rec.* **223,** 245–51 (1989).
15. MacLean, N. F., Kratky, R. G., Macfarlane, T. W. & Roach, M. R. Taper: an important feature of Y-bifurcations in porcine renal arteries and human cerebral arteries. *J. Biomech.* **25,** 1047–52 (1992).
16. Mittal, N. *et al.* A computer reconstruction of the entire coronary arterial tree based on detailed morphometric data. *Ann. Biomed. Eng.* **33,** 1015–26 (2005).
17. Papageorgiou, G. L., Jones, B. N., Redding, V. J. & Hudson, N. The areas ratio of normal arterial junctions and its implications in pulse wave reflections. *Cardiovasc. Res.* **24,** 478–84 (1990).
18. Rossitti, S. & Löfgren, J. Vascular dimensions of the cerebral arteries follow the principle of minimum work. *Stroke* **24,** 371–377 (1993).
19. Wang, D. B., Blocher, N. C., Spence, M. E., Rovainen, C. M. & Woolsey, T. A. Development and remodeling of cerebral blood vessels and their flow in postnatal mice observed with in vivo videomicroscopy. *J. Cereb. Blood Flow Metab.* **12,** 935–46 (1992).

20. Beare, R. J. *et al.* Does the principle of minimum work apply at the carotid bifurcation: a retrospective cohort study. *BMC Med. Imaging* **11,** 17 (2011).
21. Nordsletten, D. A., Blackett, S., Bentley, M. D., Ritman, E. L. & Smith, N. P. Structural morphology of renal vasculature. *Am. J. Physiol. Heart Circ. Physiol.* **291,** H296-309 (2006).
22. Cassot, F., Lauwers, F., Lorthois, S., Puwanarajah, P. & Duvernoy, H. Scaling laws for branching vessels of human cerebral cortex. *Microcirculation* **16,** 331–344 (2009).
23. Ingebrigtsen, T. *et al.* Bifurcation geometry and the presence of cerebral artery aneurysms. *J. Neurosurg.* **101,** 108–13 (2004).
24. Mut, F., Wright, S., Ascoli, G. A. & Cebral, J. R. Morphometric, geographic, and territorial characterization of brain arterial trees. *Int. j. numer. method. biomed. eng.* **30,** 755–766 (2014).
25. Suwa, N., Niwa, T., Fukasawa, H. & Sasaki, Y. Estimation of intravascular blood pressure gradient by mathematical analysis of arterial casts. *Tohoku J. Exp. Med.* **79,** 168–98 (1963).
26. Cassot, F. *et al.* Branching patterns for arterioles and venules of the human cerebral cortex. *Brain Res.* **1313,** 62–78 (2010).
27. Van Der Zwan, A. & Hillen, B. Araldite F as injection material for quantitative morphology of cerebral vascularization. *Anat. Rec.* **228,** 230–6 (1990).
28. Hardy-Stashin, J., Meyer, W. W. & Kauffman, S. L. Branching coefficient ('area ratio') of the human aortic bifurcation determined in distended specimens. *Atherosclerosis* **37,** 399–402 (1980).
29. Bouvy, W. H. *et al.* Visualization of Perivascular Spaces and Perforating Arteries With 7 T Magnetic Resonance Imaging. *Invest. Radiol.* **49,** 307–313 (2014).
30. Motulsky, H. J. & Brown, R. E. Detecting outliers when fitting data with nonlinear regression - a new method based on robust nonlinear regression and the false discovery rate. *BMC Bioinformatics* **7,** 123 (2006).
31. Dickie, R. *et al.* Three-dimensional visualization of microvessel architecture of whole-mount tissue by confocal microscopy. *Microvasc. Res.* **72,** 20–6
32. Dutly, A. E. *et al.* Fluorescent microangiography (FMA): an improved tool to visualize the pulmonary microvasculature. *Lab. Invest.* **86,** 409–16 (2006).
33. Heinzer, S. *et al.* Hierarchical microimaging for multiscale analysis of large vascular networks. *Neuroimage* **32,** 626–36 (2006).
34. Lauwers, F., Cassot, F., Lauwers-Cances, V., Puwanarajah, P. & Duvernoy, H. Morphometry of the human cerebral cortex microcirculation: general characteristics and space-related profiles. *Neuroimage* **39,** 936–48 (2008).
35. Motti, E. D., Imhof, H. G. & Yaşargil, M. G. The terminal vascular bed in the superficial cortex of the rat. An SEM study of corrosion casts. *J. Neurosurg.* **65,** 834–46 (1986).
36. Reichold, J. *et al.* Vascular graph model to simulate the cerebral blood flow in realistic vascular networks. *J. Cereb. Blood Flow Metab.* **29,** 1429–1443 (2009).
37. Tsai, P. S. *et al.* Correlations of neuronal and microvascular densities in murine cortex revealed by direct counting and colocalization of nuclei and vessels. *J. Neurosci.* **29,** 14553–70 (2009).
38. Chaplain, M. A. J., McDougall, S. R. & Anderson, A. R. A. Mathematical modeling of tumor-induced angiogenesis. *Annu. Rev. Biomed. Eng.* **8,** 233–57 (2006).
39. Grassly, N. C. & Fraser, C. Mathematical models of infectious disease transmission. *Nat. Rev. Microbiol.* **6,** 477–87 (2008).

40. Vosse, F. van de & Stergiopulos, N. Pulse wave propagation in the arterial tree. *Annu. Rev. Fluid Mech.* **43,** 467–499 (2011).
41. Hamilton, W. F. The Patterns Of The Arterial Pressure Pulse. *J. Physiol.* **141,** 235–241 (1944).
42. Nichols, W. W., O'Rourke, M. F. & Vlachopoulos, C. in *McDonald's Blood Flow in Arteries. Theoretical, Experimental and Clinical Principles* 195–223 (Hodder Arnold, 2011).
43. Schneider, M., Reichold, J., Weber, B., Székely, G. & Hirsch, S. Tissue metabolism driven arterial tree generation. *Med. Image Anal.* **16,** 1397–414 (2012).
44. Marinkovic, S. V., Milisavljevic, M. M., Kovacevic, M. S. & Stevic, Z. D. Perforating branches of the middle cerebral artery. Microanatomy and clinical significance of their intracerebral segments. *Stroke* **16,** 1022–9 (1985).
45. Umansky, F. *et al.* The perforating branches of the middle cerebral artery. A microanatomical study. *J. Neurosurg.* **62,** 261–8 (1985).
46. Uylings, H. B. Optimization of diameters and bifurcation angles in lung and vascular tree structures. *Bull. Math. Biol.* **39,** 509–20 (1977).
47. Aharinejad, S., Schreiner, W. & Neumann, F. Morphometry of human coronary arterial trees. *Anat. Rec.* **251,** 50–9 (1998).
48. Fanucci, E., Orlacchio, A., Pocek, M., Magrini, A. & Salomoni, E. Optimal branching of human arterial bifurcations. *Invest. Radiol.* **25,** 62–6 (1990).
49. Hutchins, G. M., Miner, M. M. & Boitnott, J. K. Vessel caliber and branch-angle of human coronary artery branch-points. *Circ. Res.* **38,** 572–6 (1976).
50. Rossitti, S. & Frisen, L. Remodelling of the retinal arterioles in descending optic atrophy follows the principle of minimum work. *Acta Physiol. Scand.* **152,** 333–340 (1994).
51. Pollanen, M. S. Dimensional optimization at different levels of the arterial hierarchy. *J. Theor. Biol.* **159,** 267–70 (1992).
52. Rai, A. T., Hogg, J. P., Cline, B. & Hobbs, G. Cerebrovascular geometry in the anterior circulation: an analysis of diameter, length and the vessel taper. *J. Neurointerv. Surg.* **5,** 371–5 (2013).
53. Onoue, H. *et al.* Investigation of postmortem functional changes in human cerebral arteries. *J. Cereb. Blood Flow Metab.* **13,** 346–9 (1993).
54. Patel, D. J. & Janicki, J. S. Static elastic properties of the left coronary circumflex artery and the common carotid artery in dogs. *Circ. Res.* **27,** 149–58 (1970).
55. Kerns, M. J. J. *et al.* Shrinkage of cutaneous specimens: formalin or other factors involved? *J. Cutan. Pathol.* **35,** 1093–6 (2008).
56. Su, G. W., Foroozan, R. & Yen, M. T. Quantitative analysis of temporal artery contraction after biopsy for evaluation of giant cell arteritis. *Can. J. Ophthalmol.* **41,** 500–3 (2006).
57. Guo, X., Liu, Y. & Kassab, G. S. Diameter-dependent axial prestretch of porcine coronary arteries and veins. *J. Appl. Physiol.* **112,** 982–9 (2012).

6

A simple patient-specific cerebral blood flow model

Authors:
Jasper H.G. Helthuis, MD[1,3,5], Tristan P.C. van Doormaal, MD, PhD[1,3], Sepideh Amin-Hanjani, MD, PhD[2], XinJian Du, MD[2], Fady T. Charbel MD, PhD[2], Berend Hillen, MD, PhD[4], Albert van der Zwan, MD, PhD[1,3]

Affiliations:
1 Department of Neurosurgery, University Medical Center Utrecht, Utrecht, The Netherlands
2 Department of Neurosurgery, University of Illinois, Chicago, USA
3 Brain Technology Institute, Utrecht, The Netherlands
4 Department of Anatomy, University Medical Center Nijmegen, Nijmegen, The Netherlands
5 Department of Radiology, Medisch Spectrum Twente, Enschede, The Netherlands

Status:
Submitted

Abstract

In clinical practice, many complex choices in treatment of complex cerebrovascular diseases have to be made. A patient-specific mathematical blood flow could be of aid in these decisions. For certain cases, less accuracy is required and more simplistic models might be feasible. The current study is aiming to validate a patient-specific simplistic blood flow model in 20 healthy subjects. All subjects underwent MRI and Noninvasive Optimal Vessel Analysis (NOVA) to obtain patient-specific vascular morphology and flow measurements of all major cerebral arteries for validation. The mathematical model used was based on the Hagen-Poiseuille equations. Proximal boundary conditions were patient-specific blood pressure cuff measurements. For distal boundary conditions, a structured tree and a simple autoregulatory model were applied. Autoregulatory parameters were optimized based on the data of 10 additional healthy subjects. A median percentual flow difference of -3% (interquartile range -36% to 17%) was found. Regression analysis to an identity line resulted in R^2 values of 0.71 for absolute flow values. Bland-Altman plots showed a bias (levels of agreement) of 5% (-70 to 80%) for absolute flow. Based on these results the model proofed to be accurate within a range which might be feasible for use in clinic. Major limitation to the model arises from the simplifications made compared to the actual physiological situation and limitations in the validation method. As the model is validated only in healthy subject's further validation in actual patients is needed.

Introduction

Mathematical blood flow modelling is gaining a more important role in medical research, medical device development and could have an impact on patient-specific healthcare in the near future.[1–3] Mathematical blood flow-models in healthcare might prove feasible in modelling effects different treatment options could have over time on cerebrovascular diseases. For example, this could be useful in planning for neurosurgical flow replacement bypass surgery, aneurysm clipping effects and risk assessment of aneurysm rupture.

With ever-increasing processing power, more complex 3D-flow modelling using computational fluid dynamics (CFD) and fluid structure interaction (FSI) are gaining more interest and are getting closer to clinical applicability. However, the time required for current computer systems highly depends on the complexity of the model (i.e. the extent of arteries included) and available processing power, with time between capturing patient data and simulation results ranging from a few hours to a couple of days.[4–8] Additionally, the methods required to perform CFD and FSI are complex and require adequate training and detailed knowledge. Results from these 3D-flow modelling techniques are difficult to interpret and clinical significance of many calculated variables is often not known.[9,10]

For some clinical purposes, a larger margin of error than what is achieved using complex 3D-flow models might proof sufficient. This permits the use of more simplistic 1- and 0-dimensional (1D and 0D) models. The main advantage is easier clinical implementation of these models due to shorter processing time and lower requirements of clinical parameters as input. Also, lower dimensional models are cheaper to run than complex 3D models.[11] The simplistic linear equations often used in 0D models, regularly based on Hagen-Poiseuille equations, solve almost instantaneously on current computer systems. Additionally, the complexity of usage and interpretation of the results of a simplistic model is often lower. If a simplistic model could prove accurate enough for the required clinical purpose, these advantages would warrant easier implementation in clinical practice then when a complex 3D-flow model would be used.

Important for these more simplistic models to be used in clinic is the need for them to be patient-specific. The anatomical representation and boundary conditions should match the actual patient as closely as possible. Additionally, these models need to be validated against measurements in actual human subjects. This could be done by comparison against different imaging techniques such as quantitative-MRA (qMRA), 4D-MRA and doppler ultrasound. Performing and analysis of qMRA can be eased with software packages such as NOVA (Noninvasive Optimal Vessel Analysis, Vassol, Chicago Ill, USA) [12,13]

The current study set out to develop a simple patient-specific linear model of cerebral blood flow based on the laws as described by Poiseuille-Hagen to enable fast calculations of flow for clinical use. Additionally, this model is validated against NOVA flow measurements in healthy volunteers.

Methods

Subjects

Data of 30 healthy volunteers without history of cerebral disease were recruited after approval of the local institutions ethics commission and receiving of the subject's full informed consent. Volunteers were split in two groups. Group A: 10 healthy volunteers (mean±SD age 49±15.6, 60% female, mean±SD BMI 25±4) were scanned for fitting of boundary conditions (see below). Group B: 20 healthy volunteers (mean±SD age 62±16.0, 40% female, mean±SD BMI 27±3.2) were scanned for validation. All volunteers filed in a questionnaire screening for major confounding diseases and medication use. A time-of-flight (TOF) MRI (voxel-size 0.43x0.43x0.45 mm) and qMRA was performed on all subjects on a 3T MRI scanner (Excite, GE Healthcare, Milwaukee, Wis, USA). MR volume flow measurements on all major cerebral arteries were calculated using the NOVA software on a separate workstation (see *figure 1* for a schematic overview of general included arteries). The scan protocol uses a retrospectively gated fast 2D phase-contrast sequence and has been described previously.[12,13] Standard single measurement blood pressure cuff measurement was acquired just before the qMRA.

Patient-specific morphology

A semi-automatic image processing approach was used to enable acquisition of patient specific anatomical description in sense of length and average radius of arterial segments. The technical method has been previously described in chapter 4. In summary using Simple Neurite Tracer (version 2.0.2)[14] centrelines between manually selected points were traced. As cerebral arteries are known to have minimal to no tapering, each artery was segmented as one segment (e.g. middle cerebral artery M1 part would be one segment). Only when an aneurysm or a stenosis was present the artery was split in different segments to represent the malformation. Depending on the quality of the MRI, centrelines were drawn in arterial segments for the anterior, middle and posterior cerebral arteries up to the A3, M5 and P3. Centrelines where smoothed using the MatLab SmoothN algorithm (version 1.37)[15,16] with a smoothing parameter of 20. The centrelines consist of many separate nodes. At each of these nodes the radius was calculated using a full-width-at-halve-maximum (FWHM) method.[17] To perform this FWHM-calculation image data is sampled perpendicular around the centreline. Background noise (defined as 10% of the maximum voxel intensity) is removed and the radius is calculated in 50 directions rotating around the centreline. Next, to correct for incorrect calculated radii a circularity index is applied. Finally, for each segment the mean radius from all nodes forming this segment and its cumulative length were calculated. Finally, a matrix with connectivity of each segment, radius and length is formed which can be used for patient-specific calculations. All calculations are performed using custom MatLab code (version R2014a (8.3.0.532), The Mathworks, Inc, Natick, MA, USA).

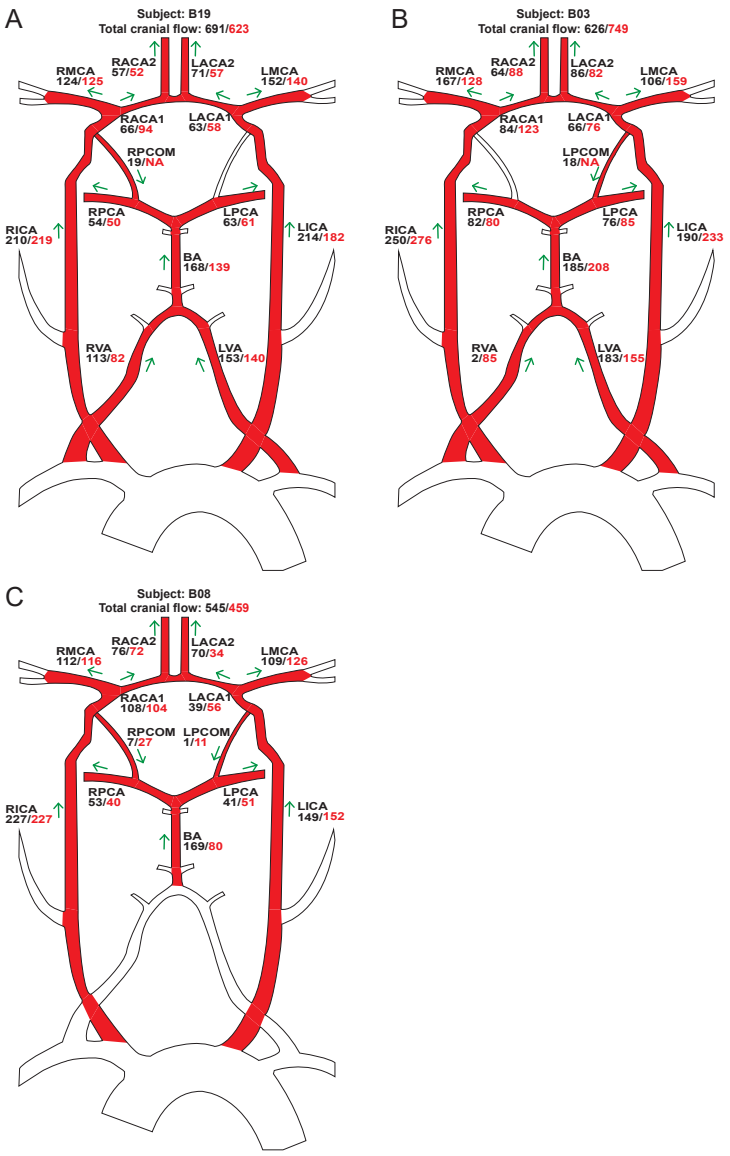

Figure 1: Computed flow is displayed in red next to the NOVA flow (black).

A: shows an example where the model closely resembles the actual NOVA flow. *B:* shows an example where especially the vertebral arteries (RVA and LVA) show a large difference between NOVA and computed flow, however the total flow through the RVA and LVA combined is almost the same as the NOVA flow as shown by the basilar artery. *C:* shows an example case where posterior communicating arteries (RPCOM, LPCOM) were present but show a large difference between the computed flow and NOVA flow. NOVA Vessel Map Copyright ©2001 VasSol, Inc. (Modified to include data from the mathematical blood flow model) Used with permission from VasSol, Inc.

Linear model

A simple linear model comparable to Hillen et al.[18] was constructed. Assumptions made were: (a) vessels are rigid, (b) vessels are uniform in radius over their length, (c) blood is an incompressible homogeneous Newtonian fluid, (d) flow is fully developed, steady and laminar, (e) presence of conservation of mass and momentum at all bifurcations. This basically results in a purely resistance model were the flow, pressure and resistance are related according to the Hagen-Poiseuille equation[19]:

$$\triangle P_i = \frac{8\mu L_i}{\pi r_i^4} \times Q_i \quad (1)$$

Were ΔP_i represents pressure drop along segment i, Φ_i flow through segment i, L_i and r_i length and radius of segment i. μ is de dynamic viscosity of blood which is set to 0.003Pa·s.

Boundary conditions

Proximal boundary conditions

At the inlets of the system the mean arterial pressure (MAP) served as boundary condition. The MAP was calculated based on the radial artery diastolic (DP) and systolic (SP) pressure as:

$$MAP = DP + \frac{1}{3}(SP - DP).$$[20,21]

Distal boundary conditions – structured tree

As the vascular territories of each major cerebral artery are known to be highly variable, distal outflow boundary conditions for each major cerebral artery needed to be different and patient-specific.[22,23] To perform this, the current study builds upon the structured tree as first described by Olufsen et al.[24] These trees assume certain branching patterns of arteries up to the arteriol level. Based on a parent artery radius (r_o) the radius of two daughter (r_1 and r_2) arteries can be calculated using scale factors α and β where $r_1 = \alpha r_0$ and $r_2 = \beta r_0$ These scale factors are based on the assumption as set forth by Murray et al.[25] and Uylings et al.[26] who describe bifurcations to be related as $r_0^\xi = r_1^\xi + r_2^\xi$ (law of Murray). In ideal laminar flow ξ would equal 3 and in fully turbulent flow 2.33. This ξ is different depending on the asymmetry of the bifurcation. As described by Zamir et al.[27] this asymmetry can be described by an area-ratio (AR) and an asymmetry ratio γ defined as:

$$AR = \frac{\pi r_1^2 + \pi r_2^2}{\pi r_0^2} \quad (2)$$

and

$$\gamma = \frac{\pi r_2^2}{\pi r_1^2} \quad \text{where} \quad r_2 \leq r_1 \tag{3}$$

Combining equations (2) and (3) results and the law of Murray, as described by Olufsen et al. [24], in:

$$AR = \frac{1+\gamma}{(1+\gamma^{\xi/2})^{2/\xi}} \tag{4}$$

Based on data described in chapter 5 the AR was chosen to be 1.33 and γ as 0.65. Finally, the scaling factors were calculated as described by Olufsen et al. [24] according to

$$\alpha = (1+\gamma^{\xi/2})^{-1/\xi} \tag{5}$$

$$\beta = \alpha\sqrt{\gamma} \tag{6}$$

The last description needed is the ratio between length and radius defined as:

$$LR = \frac{L}{R} \tag{7}$$

LR was based on a autoregulatory model (see below).

Based on these branching patterns and the radius of the distal outlets acquired from the patient-specific MRI, a structured tree up to a minimum radius of 0.1 mm was constructed for each distal outlet. These distal outlets were all of the most distal arteries constructed during segmentation and most often (depending on MRI quality) A3, M5 and P3 branches. Next a replacing resistance was calculated for each structured tree, assuming that blood flow is governed by the same Hagen-Poiseuille principle as set in equation (1), which served as distal boundary conditions. Distal to these resistances a constant pressure was applied (see further below).

Autoregulation

According to Liang et al. the cerebral perfusion rate is related to the MAP following a fourth-degree polynomial function.[28] To model autoregulation the current study opted to relate an auto-regulatory response in a simple manner to the MAP. To get a response comparable to the polynomial function as reported by Liang et al. a logistic function was used which performs vasoconstriction or dilatation in the structured trees in response to changes in the MAP. By this the resistances in the distal boundary conditions change in each subject. To ease this method, vasoconstriction and dilatation ware not per performed by changing the radius but by changing the LR according to:

$$LR = \frac{LR_{max} - LR_{min}}{1 + e^{-k(MAP - MAP_{phys})}} + LR_{min} \quad (8)$$

The physiolocial MAP (MAP_{phys}) was considered to be 1.24N/cm^2 (93 mmHg) based on a physiological blood pressure of 120/80 mmHg and the LR_{min} as 5 based on data presented in chapter 5. Values of all other parameters were chosen based on optimization using the data from the healthy subjects (see section "Model optimization" below).

Model optimization

Three parameters, the logistic growth rate paremter (k), *distal pressure*, and the maximum length-radius ratio (LR_{max}), used for the distal boundary conditions were computed using a brute force optimization algorithm. All combinations of these parameters in ranges and step sizes as depicted in *table 1* were used to calculate flow for the 10 healthy subjects in group A. Range and step sizes where based on physiological reasonable limits. As these parameters mostly have an effect on the total cerebral blood flow (CBF) through autoregulation, the parameter values were selected by minimizing the difference between the computed CBF and the CBF as measured using NOVA. Total cerebral blood flow was defined as the *inflow* into the model of each specific subject, mostly consisting of both internal carotid arteries and both vertebral arteries.

Solving method

A custom written MatLab code was to perform all calculations. First distal boundary conditions where added. Next autoregulation was applied to the distal boundary conditions. Finally, a square matrix with all resistances for all segments was generated which was used in turn to solve the set of linear equations.

Validation and statistics

Blood flow was computed using the method described above for the 20 healthy volunteers in group B. The robust regression and outlier removal (ROUT) as described by Motulsky et al. with a Q value of 1% to select and remove outliers was used in GraphPad Prism (version 6.01, GraphPad Software, Inc. La Jolla, CA, USA) to detect possible outliers.[29] All outliers were evaluated for possible reason for the large difference in model and NOVA flow measurements. In case of a true measuring error which could not be attributed to the model, outliers were excluded from further statistical analysis.

For the remaining segments after removal of outliers in all 20 healthy volunteers the percentual difference between NOVA and model flow compared to NOVA flow were calculated. Median, interquartile range (IQR), mean, standard deviation (SD) and range were calculated as descriptive statistics. Additionally, an Interclass Correlation Coefficient (ICC) using a Two-Way Mixed model searching for absolute agreement between single measurements including a 95%-confidence interval (95%-CI) was calculated using IBM SPSS Statistics (version 23.0.0.0, IBM Company, Armonk, NY, USA). A Bland-Altman plot with a range of agreement defined as a mean bias of ±2SD was generated and a scatter plot with regression analysis and calculation of a Pearson correlation coefficient to an identity line was performed using GraphPad Prism.

Results

Optimized values based on data of healthy subject group A for *k, distal pressure* and LR_{max} are displayed in *table 1*. 279 segments in which both flow calculations and NOVA measurements were performed were available from the 20 subjects. After exclusion of 8 outliers 271 segments remained for the validation. The median percentual difference in flow was -3% (IQR -36% to 17%, mean±SD -18±55%, range -476 – 78%).

Variable	Range	Step size	Optimized value
k	0.02-0.16	0.005	0.085
Distal pressure (N/cm²)	0.3-0.5	0.01	0.41
LR_{max}	60-110	2	82

Table 1: Model optimization. N/cm^2 = Newton per square centimetre. *k* = logostic growth rate parameter, LR_{max} = maximum length-radius ratio.

Figure 1 shows 3 examples of NOVA flow and computed flow in a standard NOVA report showing one adequate case without outliers (*figure 1A*) and highlighting problematic areas where outliers emerged in the vertebral arteries (VA, *figure 1B*) and posterior communicating arteries (Pcom, *figure 1C*).

For absolute flow the ICC for single measurements was 0.859 (95%-CI: 0.824-0.887). *Figure 2A* shows a scatter plot of absolute flow with an R-squared value of 0.71 for a regression analysis to an identity line. The Bland-Altman plot (*Figure 2B*) for absolute flow shows a mean bias of 5% with a level of agreement from -70% to 80%.

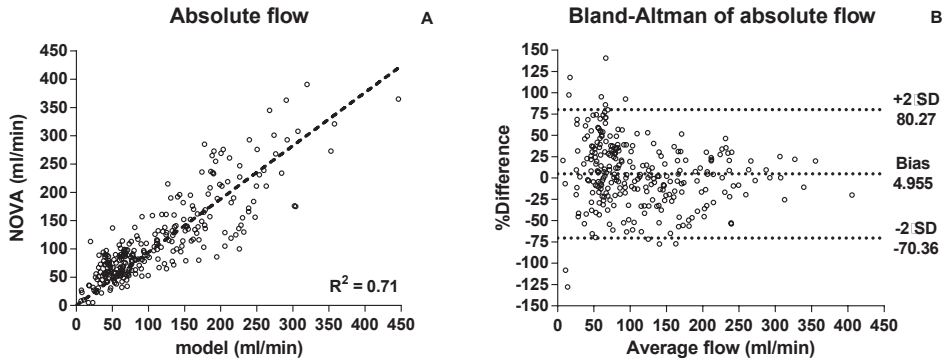

Figure 2: *A:* scatterplot comparison of computed absolute flow and NOVA flow (ml/min). The identity line shows a R^2 of 0.71. *B:* Blant-Altman plot for absolute flow.

Discussion

The current study is performed to develop a simplified linear mathematical model which should be easy to use in clinical settings for calculating the cerebral arterial blood. Validation of modelled flow was performed against non-invasive MRI based flow measurements using NOVA software in healthy subjects.

A -3% (IQR -36%-17%) median percentual difference between modelled and NOVA flow was found. Calculation of an ICC resulted in a value of 0.859 (95%-CI: 0.824-0.887). Some authors argue that this would indicate a good agreement.[30] To further analyse the actual level of agreement, scatterplots and Bland-Altman plots were generated.

The scatterplots with regression analysis to an identity line showed acceptable levels of correlation. The Blant-Altman plots show an acceptable bias of 4.9-5.9%. However, the levels of agreement for the Blant-Altman plots showed a relatively broad range from -65% to 75% for absolute flow. For all analysed arterial segments flow direction for both NOVA and calculated flow where the same, except for one outlier (Pcom, 6ml/min flow).

Based on these results, the model might prove feasible for purposes in which especially flow is of relevance and a more general trend in flow change is acceptable such as predicting optimal cerebral flow replacement surgery.

To the best of our knowledge we present the first model validated against a set of intra-cranial flow measurements in a larger population. Many other studies perform either no validation by comparison to flow measurements, limited flow or pressure measurements or to a limited number of patients.[31–36]

We utilized a TOF-MRI to acquire the morphology of the arterial structures of the specific subjects as this would be easy to acquire in a clinical setting. Arterial blood pressure was used as a patient-specific proximal boundary condition. To enable more easy to use patient-specific distal boundary conditions, a structured tree was used based on the particular branching patterns as measured previously in chapter 5.

As the cerebral circulation is known to show extensive autoregulation, we opted to include a simple autoregulatory model in the distal boundary conditions. During initial testing, running the model without the autoregulatory effects resulted in

unusable results showing large inaccuracies, with a median difference between NOVA and modelled flow of 547% (IQR: 403-818%). Hence, we included the simplified autoregulatory model which greatly improved accuracy as shown by the reported results of the current study.

The vertebral arteries (Vas) and posterior communicating arteries (Pcoms) showed the largest discrepancies. Some of these were detected by the outlier detection excluded. As shown in *figure 2B* the VAs often show an incorrect flow distribution. However, the total combined flow through the VAs is usually correct, as shown by the flow in the basilar artery. The incorrect distribution might be explained by the field-of-view of the MRI. The VAs were mostly visible for just a few millimetres length. This hampers reconstruction and increases effects of error in radius calculation of single nodes on the centrelines. If a larger field-of-view for the MRI is chosen the flow in the VA's will most likely be correctly calculated, hence we opted to exclude some of these measurements from validation.

Figure 2C shows incorrect Pcom measurements. Pcoms are generally the smaller arteries included in the patient-specific morphology. Smaller arteries are for both the NOVA technique and the mathematical model limited due to the MRI voxel resolution.[13,37,38] With larger Pcoms the difference percentual between NOVA and the model becomes smaller, showing that the model is able to capture flow through Pcoms if they are of hemodynamic importance.

Limitations

The most important limiting factor in validation of the model is the use of NOVA. NOVA is known for having a certain range of accuracy.[13,37,38] For certain arteries and lower resolutions this inaccuracy might further increase. Consequently, the model might prove to be more or less accurate then when a more accurate technique would be used, such as intraoperative ultrasonic flow probe measurements.

A second limiting factor is the accuracy of the patient-specific morphology acquired from the MRI. This is caused by multiple factors:

(a) As in resistance calculation the fourth-power of the radius is used. Small inaccuracies in calculation of the radius will result in a large error in resistance and in turn in flow calculations. Incorrect calculated radii can result when artefacts are present or centrelines are inadequately drawn. The current model tries to overcome effects of incorrect radius at single locations by assuming complete segments to be non-tapering and using the mean radius of an entire segment.

(b) Use of a semi-automatic method. This can result in the user missing arteries for segmentation. A user can likewise incorrectly segment or miss a stenosis or aneurysm. However, using a full-automatic method can include "false positive or negative" arteries, making incorrect connections between arteries or miss smaller arteries. Hence, the current study opted for a semi-automatic approach.

A third limiting factor is related to the use of structured trees as distal boundary conditions. As was shown by Cousins et al. the structured tree model is sensitive to the minimum radius which is used to determine the extent of the structured tree.[39] The minimum radius would differ between each major cerebral artery and should best be fitted to experimental data.[24,39] In the current study we however choose to use a fixed minimum radius close to the size of arterioles and optimized the distal pressure to data of healthy subjects. This partially removes the need for selecting an optimal minimum radius.

Furthermore, the model uses a simplified version of the structured trees by using the Hagen-Poiseuille equations for resistance calculation, assuming a constant viscosity for all arteries. However, it is known that viscosity decreases with a decreasing vessel radius.[40] Finally a fixed AR, γ and LR might not be the best representation of the actual arterial tree as these values are known to show a large distribution and might show different values between larger and smaller arteries.[41–49] However, the current model opted to use fixed values to keep the model simplistic to enable easier calculations.

A last limiting factor is the used auto-regulatory model. The current model opted for a simple logistic function between MAP and peripheral resistance. However, autoregulation is known to be more complex and might differ in an actual patient as the auto-regulatory response is known to change in cases of prolonged hemodynamically compromised cerebral blood supply.[50–53] A more complex version of autoregulation might improve accuracy of the model, but would increase complexity of the model, which might hamper clinical implementation.

Conclusion

The current study is performed out to develop a simple linear patient-specific model with fast and easy calculations of blood flow through the cerebral circulation, which would ease clinical applicability. The validation performed on healthy subjects shows the accuracy to be within the range which might be clinically feasible in the prediction of flow after treatments such as bypass surgery and/or complex aneurysm treatments. This warrants further validation of the model in a patient population to quantify its value in a patient-specific setting.

Acknowledgements

The research leading to these results have received funding from the Netherlands Organisation for Health Research and Development (ZonMw) Project number 11.631.0005. We would like to thank Marloes Vermeer from the Medical School Twente of the Medical Spectrum Twente for her advice in statistical methods and analysis.

References

1. Sforza, D. M., Putman, C. M. & Cebral, J. R. Computational fluid dynamics in brain aneurysms. *International Journal for Numerical Methods in Biomedical Engineering* **28,** 801–808 (2012).
2. Cebral, J. *et al.* Clinical application of image-based CFD for cerebral aneurysms. *Int. j. numer. method. biomed. eng.* **27,** 977–992 (2011).
3. Morris, P. D. *et al.* Computational fluid dynamics modelling in cardiovascular medicine. *Heart* **102,** 18–28 (2016).
4. Qian, Y., Takao, H., Umezu, M. & Murayama, Y. Risk analysis of unruptured aneurysms using computational fluid dynamics technology: preliminary results. *AJNR. Am. J. Neuroradiol.* **32,** 1948–1955 (2011).
5. Grinberg, L., Anor, T., Madsen, J. R., Yakhot, A. & Karniadakis, G. E. Large-scale simulation of the human arterial tree. *Clin. Exp. Pharmacol. Physiol.* **36,** 194–205 (2009).
6. Grinberg, L., Cheever, E., Anor, T., Madsen, J. R. & Karniadakis, G. E. Modeling blood flow circulation in intracranial arterial networks: a comparative 3D/1D simulation study. *Ann. Biomed. Eng.* **39,** 297–309 (2011).
7. Cebral, J. R. *et al.* Analysis of hemodynamics and wall mechanics at sites of cerebral aneurysm rupture. *J. Neurointerv. Surg.* 1–7 (2015). doi:10.1136/neurintsurg-2014-011247
8. Seo, J.-H., Eslami, P., Caplan, J., Tamargo, R. J. & Mittal, R. A Highly Automated Computational Method for Modeling of Intracranial Aneurysm Hemodynamics. *Front. Physiol.* **9,** 681 (2018).
9. Can, A. & Du, R. Association of Hemodynamic Factors With Intracranial Aneurysm Formation and Rupture. *Neurosurgery* **78,** 510–520 (2016).
10. Meng, H., Tutino, V. M., Xiang, J. & Siddiqui, A. High WSS or low WSS? Complex interactions of hemodynamics with intracranial aneurysm initiation, growth, and rupture: toward a unifying hypothesis. *AJNR. Am. J. Neuroradiol.* **35,** 1254–1262 (2014).
11. Groen, D. *et al.* Validation of Patient-Specific Cerebral Blood Flow Simulation Using Transcranial Doppler Measurements. *Front. Physiol.* **9,** 721 (2018).
12. Zhao, M. *et al.* Regional Cerebral Blood Flow Using Quantitative MR Angiography. *Am. J. Neuroradiol.* **28,** 1470–1473 (2007).
13. Zhao, M., Charbel, F. T., Alperin, N., Loth, F. & Clark, M. E. Improved phase-contrast flow quantification by three-dimensional vessel localization. *Magn. Reson. Imaging* **18,** 697–706 (2000).
14. Longair, M. H., Baker, D. A. & Armstrong, J. D. Simple Neurite Tracer: open source software for reconstruction, visualization and analysis of neuronal processes. *Bioinformatics* **27,** 2453–4 (2011).
15. Garcia, D. A fast all-in-one method for automated post-processing of PIV data. *Exp. Fluids* **50,** 1247–1259 (2011).
16. Garcia, D. Robust smoothing of gridded data in one and higher dimensions with missing values. *Comput. Stat. Data Anal.* **54,** 1167–1178 (2010).
17. Hoogeveen, R. M., Bakker, C. J. & Viergever, M. A. Limits to the accuracy of vessel diameter measurement in MR angiography. *J. Magn. Reson. Imaging* **8,** 1228–35 (1998).
18. Hillen, B., Hoogstraten, H. W. & Post, L. A mathematical model of the flow in the circle of Willis. *J. Biomech.* **19,** 187–194 (1986).
19. Sutera, S. P. & Skalak, R. The History of Poiseuille's Law. *Annu. Rev. Fluid Mech.* **25,** 1–20 (1993).

20. Paultre, F. & Mosca, L. Association of Blood Pressure Indices and Stroke Mortality in Isolated Systolic Hypertension. *Stroke* **36,** 1288–1290 (2005).
21. Sesso, H. D. *et al.* Systolic and diastolic blood pressure, pulse pressure, and mean arterial pressure as predictors of cardiovascular disease risk in Men. *Hypertension* **36,** 801–7 (2000).
22. van der Zwan, A., Hillen, B., Tulleken, C. A. & Dujovny, M. A quantitative investigation of the variability of the major cerebral arterial territories. *Stroke* **24,** 1951–9 (1993).
23. van der Zwan, A. & Hillen, B. Review of the variability of the territories of the major cerebral arteries. *Stroke* **22,** 1078–84 (1991).
24. Olufsen, M. S. Structured tree outflow condition for blood flow in larger systemic arteries. *Am. J. Physiol.* **276,** H257-68 (1999).
25. Murray, C. D. The physiological principle of minimum work applied to the angle of branching of arteries. *J. Gen. Physiol.* **9,** 835–41 (1926).
26. Uylings, H. B. Optimization of diameters and bifurcation angles in lung and vascular tree structures. *Bull. Math. Biol.* **39,** 509–20 (1977).
27. Zamir, M. Nonsymmetrical bifurcations in arterial branching. *J. Gen. Physiol.* **72,** 837–45 (1978).
28. Liang, F., Fukasaku, K., Liu, H. & Takagi, S. A computational model study of the influence of the anatomy of the circle of willis on cerebral hyperperfusion following carotid artery surgery. *Biomed. Eng. Online* **10,** 84 (2011).
29. Motulsky, H. J. & Brown, R. E. Detecting outliers when fitting data with nonlinear regression - a new method based on robust nonlinear regression and the false discovery rate. *BMC Bioinformatics* **7,** 123 (2006).
30. Koo, T. K. & Li, M. Y. A Guideline of Selecting and Reporting Intraclass Correlation Coefficients for Reliability Research. *J. Chiropr. Med.* **15,** 155–163 (2016).
31. DeVault, K. *et al.* Blood Flow in the Circle of Willis: Modeling and Calibration. *Multiscale Model. Simul.* **7,** 888–909 (2008).
32. Kailasnath, P. *et al.* Intracarotid pressure measurements in the evaluation of a computer model of the cerebral circulation. *Surg. Neurol.* **50,** 257–263 (1998).
33. Ho, H., Mithraratne, K., Schmid, H., Sands, G. & Hunter, P. Computer simulation of vertebral artery occlusion in endovascular procedures. *Int. J. Comput. Assist. Radiol. Surg.* **5,** 29–37 (2010).
34. Brosig, R. *et al.* Blood flow quantification using 1D CFD parameter identification. in *MEDICAL IMAGING 2014: IMAGE PROCESSING* (ed. Ourselin, S and Styner, M.) **9034,** 90342R (2014).
35. Roessler, F. C., Reith, W. & Siegel, G. Simulation of cerebral hemodynamics for preoperative risk assessment. *Brain Res.* **1118,** 183–191 (2006).
36. Charbel, F. T. *et al. A patient-specific computer model to predict outcomes of the balloon occlusion test. Journal of neurosurgery* **101,** 977–988 (2004).
37. Amin-Hanjani, S., Shin, J. H., Zhao, M., Du, X. & Charbel, F. T. Evaluation of extracranial–intracranial bypass using quantitative magnetic resonance angiography. *J. Neurosurg.* **106,** 291–298 (2007).
38. Calderon-Arnulphi, M. *et al.* In Vivo Evaluation of Quantitative MR Angiography in a Canine Carotid Artery Stenosis Model. *Am. J. Neuroradiol.* **32,** 1552–1559 (2011).
39. Cousins, W. & Gremaud, P. Boundary conditions for hemodynamics: The structured tree revisited. *J. Comput. Phys.* **231,** 6086–6096 (2012).
40. Secomb, T. W. & Pries, A. R. Blood viscosity in microvessels: experiment and theory. *Comptes rendus. Phys.* **14,** 470–478 (2013).

41. Helthuis, J. H. G. *et al.* Branching Pattern of the Cerebral Arterial Tree. *Anat. Rec.* (2018). doi:10.1002/ar.23994
42. Cassot, F., Lauwers, F., Fouard, C., Prohaska, S. & Lauwers-Cances, V. A novel three-dimensional computer-assisted method for a quantitative study of microvascular networks of the human cerebral cortex. *Microcirculation* **13,** 1–18 (2006).
43. Papageorgiou, G. L., Jones, B. N., Redding, V. J. & Hudson, N. The areas ratio of normal arterial junctions and its implications in pulse wave reflections. *Cardiovasc. Res.* **24,** 478–84 (1990).
44. Rossitti, S. & Löfgren, J. Vascular dimensions of the cerebral arteries follow the principle of minimum work. *Stroke* **24,** 371–377 (1993).
45. Cassot, F. *et al.* Branching patterns for arterioles and venules of the human cerebral cortex. *Brain Res.* **1313,** 62–78 (2010).
46. Hardy-Stashin, J., Meyer, W. W. & Kauffman, S. L. Branching coefficient ('area ratio') of the human aortic bifurcation determined in distended specimens. *Atherosclerosis* **37,** 399–402 (1980).
47. Fanucci, E., Orlacchio, A., Pocek, M., Magrini, A. & Salomoni, E. Optimal branching of human arterial bifurcations. *Invest. Radiol.* **25,** 62–6 (1990).
48. Hutchins, G. M., Miner, M. M. & Boitnott, J. K. Vessel caliber and branch-angle of human coronary artery branch-points. *Circ. Res.* **38,** 572–6 (1976).
49. Pollanen, M. S. Dimensional optimization at different levels of the arterial hierarchy. *J. Theor. Biol.* **159,** 267–70 (1992).
50. Aries, M. J. H., Elting, J. W., De Keyser, J., Kremer, B. P. H. & Vroomen, P. C. A. J. Cerebral Autoregulation in Stroke: A Review of Transcranial Doppler Studies. *Stroke* **41,** 2697–2704 (2010).
51. Paulson, O. B., Strandgaard, S. & Edvinsson, L. Cerebral autoregulation. *Cerebrovasc. Brain Metab. Rev.* **2,** 161–92 (1990).
52. Immink, R. V. *et al.* Impaired Cerebral Autoregulation in Patients With Malignant Hypertension. *Circulation* **110,** 2241–2245 (2004).
53. Urbano, F., Roux, F., Schindler, J. & Mohsenin, V. Impaired cerebral autoregulation in obstructive sleep apnea. *J. Appl. Physiol.* **105,** 1852–1857 (2008).

7

General discussion

General discussion

The research embodied in the current thesis aimed to develop a simplified patient-specific cerebrovascular blood flow model feasible for usage in a clinical setting. As set out in **chapter I** such models could aid physicians in complex treatment decisions for a variety of cerebrovascular diseases.

Depending on the specific usage case, more complex 3D flow modelling might be needed. One example is given in **chapter II** in which a 3D model was used to predict effects of proximal and distal occlusion in complex cerebrovascular aneurysms on intra-aneurysmal thrombosis and flow patterns. However, this example also showed the challenges in 3D flow modelling such as requirement of excessive user interference, calculation speed and difficulties in interpretation of results. For other purposes a more simplified 1D or 0D model might be feasible.

Simplified models have a few major advantages. First, their required patient specific input is less complex. While in 3D models proximal boundary conditions often need phase-contrast MRI measurements, simplified models as presented in **chapter VI** can suffice with for example only blood pressure cuff measurements.[1] Second, errors in generation of a 3D model due to inaccuracies in the captured imaging data of a specific patient, will likely have a larger effect on predicted results in 3D models compared to more simplistic models.[2] Third are a set of advantages of simplified models derived from the fact that these models are only able to calculate a limited set of hemodynamic properties (mainly pressure, blood flow and wave reflections).[3] This results in a few distinct benefits: (a) These parameters are often easier to interpret by treating physicians. For example, vascular neurosurgeons are likely able to understand volumetric flow rates without difficulty. (b) Hemodynamic parameters in simplified models are likely easier to link to patient outcome in certain cerebrovascular diseases.[4] (c) Validation of these hemodynamic parameters are more likely to succeed. As was shown in **chapter VI**, flow can be measured *in vivo* using for example PC-MRI, enabling validation of calculated flow values. Additionally, in simplified models, phantom studies can be performed more easily compared to 3D models.[5,6] The more complex parameters such as flow patterns and especially WSS as available in 3D models are not as easy to measure, hence validation of such models is more complex.

These advantages of simplified models will likely ease implementation in a clinical setting. One of such simplified models was presented in **chapter VI**. We developed and validated a model based on the Hagen-Poiseuille equations combined. This model was coupled with distal boundary conditions based on structured trees and a simple

autoregulatory model. This is one of the most simplistic approaches possible while still trying to be patient-specific. This model showed a relatively broad confidence interval which might partially be contributed to the high degree of simplification, but possibly also to inaccuracies in the "golden standard" used for validation.

To further evaluate to what extend this broad confidence interval limits clinical usability in complex patients we performed a pre-liminary study in 19 cerebrovascular bypass patients. We modelled the pre- and postoperative flow using the model as presented in **chapter VI**. We additionally had one experienced neurosurgeon predict bypass related clinical failure based on the modelled flow and compared this to short-term clinical follow-up. Based on an interclass correlation coefficient using a two-way mixed model searching for absolute agreement in single measurements there was a poor reliability when comparing the modelled flow to both Non-invasive Optimal Vessel Analysis (NOVA) MRI flow measurements and per-operative doppler flow measurements. However, when comparing NOVA to doppler measured flow there was also a poor reliability. Pre-liminary results showed a high sensitivity and negative predictive value (NPV) of both 100% when comparing predicted clinical outcome to actual outcome. However, the specificity and positive-predictive values (PPV) where low with 82.4% and 40% respectively. This shows that the modelled flow has a large confidence interval compared to the actual flow measurements**.** The high NPV and low PPV show that If the model predicts a successful bypass, it is likely safe to continue. However, if the model predicts a bypass to be non-successful, other clinical parameters and clinical experience are needed to determine if the bypass can safely be constructed. This limits clinical applicability. However, this pre-liminary study needs further refinement.

As discussed above the simplified model presented in **chapter VI** showed in a pre-liminary test that it might be able to predict a positive clinical outcome of a bypass surgery regardless of the broad confidence interval in actual flow values. It was however not able to predict a clinical failure. A more complex one-dimensional model as published by Charbel at al. was able to predict with a 100% sensitivity and 100 % specificity the outcome of a balloon occlusion test in 16 patients.[7] This shows that in a clinical setting simplified models have great potential.

The choice of which model to utilize mainly depends on the required output parameters, available patient-specific input and needed accuracy. 3D models are expected to be more accurate, However, the difference in accuracy between 3D and simplified models is expected to be of limited value when more simplistic hemodynamic properties are of interest such as volumetric flow rates. Yet, 3D models

are more complex and often require a more detailed patient-specific input increasing the difficulty to implement them clinically. However, the most important strength of a 3D model is their ability to provide detailed information on stresses in the arterial wall.[8–11] Therefore, in the distant future 3D blood flow modelling may play a prominent role in predicting outcomes of cerebrovascular diseases.

Nonetheless, as simplified models show great potential, one has to consider their usage before advancing to 3D models. If a relevant clinical question can be answered using a simplified model, this will greatly ease clinical implementation and validation. Hence, research in the near future should focus on further refinement and validation of simplified models, while development of 3D models also needs to progress as these will likely be required for a set of specific highly relevant clinical questions such as aneurysms rupture risk prediction.

Future perspectives and challenges

0D and 1D flow modelling

As stated, simplified models, such as presented in **chapter VI**, show great potential and are likely easier to implement in clinic. To the best of our knowledge two feasible simplified models showing promising results are currently available. One is the simplified model presented in the current thesis. A second is a model as presented by Charbel at al.[7] He utilized a sector based model in which distal boundary conditions and collateral flow were fitted using patient-specific phase-contrast MRI flow measurements of all major cerebral arteries. Using this they were able to accurately predict outcome of a balloon occlusion test (BOT) and capture leptomeningeal blood flow. However, this is at the expense of an increased requirement on patient specific input. The model as presented in the current thesis shows a lower degree of accuracy, but has a major advantage of requiring less complex patient specific input.

Depending on the usage case, one of these models might proof feasible. If potential collateral flow is of importance, the model as presented by Charbel et al. is well applicable.[7] When collateral flow is of less clinical importance to a specific question the more simplified model as presented in **chapter VI** could proof feasible. Depending on the specific usage case some further changes to these models might be required. For example, in case a lower dimensional model is used to answer clinical questions related to autoregulation, a simplified model as presented in the current thesis, adapted with a more complex autoregulatory model as discussed in **chapter III** model might proof sufficient.

As potentially applicable models are already available, research has to be focussed on further tuning these models to relevant clinical questions. When both models do not proof applicable to a clinical question a different simplified model might be developed using information as set out in **chapter III**.

Further development of the model presented in this thesis and by Charbel et al. is required.[7] Especially automation of different steps in pre- and postprocessing are of importance. For example, the semi-automatic segmentation technique using in the current thesis is still tedious, time-consuming and prone to user error. Usage of segmentation techniques available in 3D flow modelling such as the well-known Vascular Modelling toolkit (VMTK) or other already published techniques might proof useful.[2,12–16] Automation of these steps will reduce user error and improve workflow, which eases clinical implementation.

Additionally, further validation of these simplified models is required as both the model presented in the current thesis as well as the model presented by Charbel et al. are only validated in a relatively small group of patients.[7] A larger set of retrospective and subsequent prospective data is required.

During further development and validation of these models, physicians who will use the end product should be closely involved. They are able to give direct feedback on the workflow, graphical user interfaces and way of presenting data. This will enable further development of an easy to use method with understandable clinically relevant output and will warrant easier clinical implementation.

3D flow modelling

For some clinical questions 3D models might be required due to the need of information on flow patterns and wall stresses. In the prediction of risk of rupture of an intracranial aneurysm for instance, the size of the aneurysm is one of the most important determinants.[17] However in future 3D models the configuration and calculated hemodynamic parameters such as wall shear stress could be determined and therefore be helpful in solving this important question. Compared to simplified models, these 3D models are still facing considerable challenges. Many steps need to be automated and validated ranging from patient-specific input, to running the computational fluid dynamics (CFD) calculations and generating understandable output.

Automation

Automation will speed up the workflow, reduce the risk of user error and will increase repeatability and consequently reliability. An important step for automation is construction of the model used for calculations. Traditionally this is done by (a) segmentation of the arterial lumen from angiography data (e.g. magnetic resonance angiography, computed tomography angiography or 3D rotational angiography), (b) followed by generation of a 3D model, (c) removing unwanted or incorrect arterial segments, (d) generation of a mesh consisting of many separate smaller elements (e.g. an arterial wall is converted to a layer of millions of brick shaped elements) and (e) mesh corrections (e.g. artefact holes, smoothing). At each step different software (both commercial and open source) can be used, but still considerable human interference is required resulting in slowing of the process. Any error in mesh generation, often human error, will lead to incorrect results.[2] Therefore, automation is of major importance. Multiple authors have performed valuable ground work for automating this process and tools such as VTMK have been created.[2,12–16] However, many of these techniques are lacking in adequate validation in a patient population and still require

proper sensitivity analysis to show the possible effect of aspects such as image quality, user input and reconstruction parameters. Regardless, important steps towards the future have been made.[2,12–16]

Patient-specific boundary conditions

Another problem of importance is the usage of patient-specific boundary conditions. As shown in previous studies using either general or patient-specific inflow boundary conditions results in different results of 3D CFD results, most notably are differences in wall shear stresses (WSS).[1,18–21] Flow patterns are less sensitive to the usage of general inflow boundary conditions. In the future 4D MRI based flow measurements might proof even more reliable but but are more complex in usage.[22,23] Also in cases of aneurysm rupture prediction models, these patient-specific proximal boundary conditions are of major importance.[1,18–21]

As the distribution territories of the major cerebral arteries are known known to be highly variable.[24,25] the consequent distal boundary conditions will also largely vary between territories. This will have a profound effect on modelling blood flows. This challenge of adequate distal boundary conditions is valid for both 3D and lower dimensional models and can possibly be solved using the structured vascular tree as model presented in **chapter VI** or by incorporating MRI based flow measurements as was done by Charbel et al.[7]

Calculation times

Depending on the clinical usage case, calculation times might be of importance. For aneurysm rupture risk prediction, in which a single cerebrovascular aneurysm needs to be modelled, longer calculation times are acceptable. However, when for example a neurosurgeon wants to virtually "try out" the effects different clip locations and possible bypass locations will have on rupture risk and flow patterns, calculation times are of increasing importance. Optimally the physician immediately sees the results and effects of changing for example the aneurysm clip location. With utilisation of current supercomputer capabilities and optimized solving algorithms calculation times range from hours to days, still limiting clinical applicability.[2,11,26–28] Ever increasing processing power (as described by Moore's law) and expected decreasing costs of supercomputer usage, will likely lead to clinical feasible calculation times in the future.[29] However, if it is possible to use a simplified model for a specific research question, calculations will solve almost instantaneously, easing clinical implementation when a treating physician wants to evaluate different treatment options.

Post-processing and validation

Post-processing of results into easy to understand results are of importance. Certain hemodynamic factors such as an increase or decrease of WSS and wall tension are thought to have an effect on aneurysm formation and rupture risk.[30–41] Presenting a physician with distribution of WSS across an aneurysm wall, or change in WSS before and after a certain treatment, will not tell this physician to what risk a patient is exposed or to what extent a treatment results in an improved morbidity and mortality rate. A physician needs uncomplicated information such as a rupture risk before and after treatment, a clear percentage of risk of stroke or easy to understand flow values.

However, to be able to provide such easy to interpret results, large studies are needed to investigate the effects of different hemodynamic factors in all cerebrovascular diseases of interest. Adequate validation of results are needed before they can clinically be implemented. More complex models such as 3D CFD models, result in a larger set of different hemodynamic properties. Acquisition of large databases and finding adequate predicting parameters is challenging and often leads to conflicting results.[37]

The above described difficulties in automation, boundary conditions, processing times but especially interpretation and acquisition of large cohorts of 3D flow results leads to a lack of clinical implementation. Due to these further required developments, it is still unlikely that in the near future 3D flow modelling will pay a central role in clinical decisions for cerebrovascular patients. However, the technique and progressive improvements warrant further development and might lead to clinical implementation in the distant future. Hence, besides development and especially validation of simplified models, further development of 3D models needs to continue.

Concluding remarks

Patient-specific cerebrovascular blood flow models might benefit patients. Simplified models like presented in the current thesis show great potential. However, specific clinical questions, such as aneurysm rupture risk predictions, likely need 3D flow modelling.

Based on diseases and treatments of interest researchers and physicians have to strongly consider a simplified model over a 3D model if feasible. Even if al challenges in 3D models are overcome, simplified models keep a profound advantage as they will likely require less effort to implement in a clinical workflow and are easier to validate. If the broad confidence interval as presented in the current thesis is not adequate for a specific clinical question, other simplified models in which for example MRI based flow measurements are incorporated are likely suitable. One example is presented by Charbel et al.[7] However, if detailed knowledge on flow patterns or wall stresses are required 3D models are needed.

Hence in the future further development in both 3D and simplified models has to take place. Especially improvements in automation, workflow, speed and repeatability are needed. Many of these refinements in 3D modelling will also benefit simplified models and vice versa. Sensitivity analysis of the model for patient-specific input, methods and parameters need to be performed.[19] Validation in larger patient populations is needed to show the strengths and weaknesses of any model for future applicability in clinic.

References

1. Cornelissen, B. M. W. *et al.* Aneurysmal Parent Artery-Specific Inflow Conditions for Complete and Incomplete Circle of Willis Configurations. *AJNR. Am. J. Neuroradiol.* **39,** 910–915 (2018).
2. Seo, J.-H., Eslami, P., Caplan, J., Tamargo, R. J. & Mittal, R. A Highly Automated Computational Method for Modeling of Intracranial Aneurysm Hemodynamics. *Front. Physiol.* **9,** 681 (2018).
3. Vosse, F. van de & Stergiopulos, N. Pulse wave propagation in the arterial tree. *Annu. Rev. Fluid Mech.* **43,** 467–499 (2011).
4. Amin-Hanjani, S. *et al.* Effect of Hemodynamics on Stroke Risk in Symptomatic Atherosclerotic Vertebrobasilar Occlusive Disease. *JAMA Neurol.* **73,** 178–85 (2016).
5. Tsang, A. C. O. *et al.* Blood flow in intracranial aneurysms treated with Pipeline embolization devices: computational simulation and verification with Doppler ultrasonography on phantom models. *Ultrasonography* **34,** 98–108 (2015).
6. Fahrig, R., Nikolov, H., Fox, a. J. & Holdsworth, D. W. A three-dimensional cerebrovascular flow phantom. *Med. Phys.* **26,** 1589–1599 (1999).
7. Charbel, F. T. *et al.* A patient-specific computer model to predict outcomes of the balloon occlusion test. *J. Neurosurg.* **101,** 977–988 (2004).
8. Krijger, J. K. B., Hillen, B. & Hoogstraten, H. W. Mathematical models of the flow in the basilar artery. *Acta Morphol. Neerl. Scand.* **27,** 225–226 (1989).
9. Moore, S. M., Moorhead, K. T., Chase, J. G., David, T. & Fink, J. One-dimensional and three-dimensional models of cerebrovascular flow. *J. Biomech. Eng.* **127,** 440–449 (2005).
10. Reymond, P. *et al.* Patient-specific mean pressure drop in the systemic arterial tree, a comparison between 1-D and 3-D models. *J. Biomech.* **45,** 2499–2505 (2012).
11. Grinberg, L., Cheever, E., Anor, T., Madsen, J. R. & Karniadakis, G. E. Modeling blood flow circulation in intracranial arterial networks: a comparative 3D/1D simulation study. *Ann. Biomed. Eng.* **39,** 297–309 (2011).
12. The Vascular Modeling Toolkit (VMTK). Available at: http://www.vmtk.org/. (Accessed: 1st February 2019)
13. Ajam, A. *et al.* A Review on Segmentation and Modeling of Cerebral Vasculature for Surgical Planning. *IEEE Access* **5,** 15222–15240 (2017).
14. Boegel, M. *et al.* A fully-automatic locally adaptive thresholding algorithm for blood vessel segmentation in 3D digital subtraction angiography. in *Proceedings of the Annual International Conference of the IEEE Engineering in Medicine and Biology Society, EMBS* **2015,** 2006–2009 (Institute of Electrical and Electronics Engineers Inc., 2015).
15. C.-Y., H. *et al.* Gap-free segmentation of vascular networks with automatic image processing pipeline. *Comput. Biol. Med.* **82,** 29–39 (2017).
16. Cebral, J. R. *et al.* Efficient pipeline for image-based patient-specific analysis of cerebral aneurysm hemodynamics: technique and sensitivity. *IEEE Trans. Med. Imaging* **24,** 457–67 (2005).
17. Greving, J. P. *et al.* Development of the PHASES score for prediction of risk of rupture of intracranial aneurysms: a pooled analysis of six prospective cohort studies. *Lancet. Neurol.* **13,** 59–66 (2014).

18. Jansen, I. G. H. *et al.* Generalized versus Patient-Specific Inflow Boundary Conditions in Computational Fluid Dynamics Simulations of Cerebral Aneurysmal Hemodynamics. *Am. J. Neuroradiol.* **35,** 1543–1548 (2014).
19. Donders, W. P. Towards patient-specific (cerebro-)vascular model applications. (Maastricht University, 2016).
20. Marzo, A. *et al.* Influence of inlet boundary conditions on the local haemodynamics of intracranial aneurysms. *Comput. Methods Biomech. Biomed. Engin.* **12,** 431–44 (2009).
21. Venugopal, P. *et al.* Sensitivity of patient-specific numerical simulation of cerebal aneurysm hemodynamics to inflow boundary conditions. *J. Neurosurg.* **106,** 1051–60 (2007).
22. Bakhshinejad, A. *et al.* Merging computational fluid dynamics and 4D Flow MRI using proper orthogonal decomposition and ridge regression. *J. Biomech.* **58,** 162–173 (2017).
23. Itatani, K. *et al.* New imaging tools in cardiovascular medicine: computational fluid dynamics and 4D flow MRI. *Gen. Thorac. Cardiovasc. Surg.* **65,** 611–621 (2017).
24. van Laar, P. J. *et al.* In vivo flow territory mapping of major brain feeding arteries. *Neuroimage* **29,** 136–44 (2006).
25. van der Zwan, A., Hillen, B., Tulleken, C. A. & Dujovny, M. A quantitative investigation of the variability of the major cerebral arterial territories. *Stroke* **24,** 1951–9 (1993).
26. Qian, Y., Takao, H., Umezu, M. & Murayama, Y. Risk analysis of unruptured aneurysms using computational fluid dynamics technology: preliminary results. *AJNR. Am. J. Neuroradiol.* **32,** 1948–1955 (2011).
27. Grinberg, L., Anor, T., Madsen, J. R., Yakhot, A. & Karniadakis, G. E. Large-scale simulation of the human arterial tree. *Clin. Exp. Pharmacol. Physiol.* **36,** 194–205 (2009).
28. Cebral, J. R. *et al.* Analysis of hemodynamics and wall mechanics at sites of cerebral aneurysm rupture. *J. Neurointerv. Surg.* 1–7 (2015). doi:10.1136/neurintsurg-2014-011247
29. Mack, C. A. Fifty Years of Moore's Law. *IEEE Trans. Semicond. Manuf.* **24,** 202–207 (2011).
30. Can, A. & Du, R. Association of Hemodynamic Factors With Intracranial Aneurysm Formation and Rupture. *Neurosurgery* **78,** 510–520 (2016).
31. Cebral, J. R. *et al.* Characterization of cerebral aneurysms for assessing risk of rupture by using patient-specific computational hemodynamics models. *Am. J. Neuroradiol.* **26,** 2550–2559 (2005).
32. Y., M. *et al.* Hemodynamics of bleb formation in cerebral aneurysms. *Japanese J. Neurosurg.* **21,** 413–419 (2012).
33. Fukazawa, K. *et al.* Using Computational Fluid Dynamics Analysis to Characterize Local Hemodynamic Features of Middle Cerebral Artery Aneurysm Rupture Points. *World Neurosurg.* **83,** 80–86 (2015).
34. Hall, A. J., Busse, E. F., McCarville, D. J. & Burgess, J. J. Aortic wall tension as a predictive factor for abdominal aortic aneurysm rupture: improving the selection of patients for abdominal aortic aneurysm repair. *Ann. Vasc. Surg.* **14,** 152–157 (2000).
35. Isaksen, J. G. *et al.* Determination of wall tension in cerebral artery aneurysms by numerical simulation. *Stroke* **39,** 3172–3178 (2008).
36. Liu, J. *et al.* Morphologic and hemodynamic analysis of paraclinoid aneurysms: ruptured versus unruptured. *J. Neurointerv. Surg.* **6,** 658–663 (2014).
37. Meng, H., Tutino, V. M., Xiang, J. & Siddiqui, A. High WSS or low WSS? Complex interactions of hemodynamics with intracranial aneurysm initiation, growth, and rupture: toward a unifying hypothesis. *AJNR. Am. J. Neuroradiol.* **35,** 1254–1262 (2014).

38. Sforza, D. M. *et al.* Hemodynamics in growing and stable cerebral aneurysms. *J. Neurointerv. Surg.* **8,** 407–412 (2016).
39. Sforza, D. M., Putman, C. M. & Cebral, J. R. Hemodynamics of Cerebral Aneurysms. *Annu. Rev. Fluid Mech.* **41,** 91–107 (2009).
40. Takao, H. *et al.* Hemodynamic differences between unruptured and ruptured intracranial aneurysms during observation. *Stroke.* **43,** 1436–1439 (2012).
41. Venkatasubramaniam, A. K. *et al.* A comparative study of aortic wall stress using finite element analysis for ruptured and non-ruptured abdominal aortic aneurysms. *Eur. J. Vasc. Endovasc. Surg.* **28,** 168–176 (2004).

Addendum

English summary

English summary

This thesis describes the development of a simplified patient-specific cerebrovascular blood flow model feasible for clinical usage.

In **chapter I** an outline of the thesis and general introduction is given. General aspects related to blood flow modelling, such as laminar versus turbulent flow, viscosity and density, are introduced. Elastic properties of arterial wall are described as these will have an effect on blood flow modelling in case of a pulsatile flow. An explanation of important differences between zero-dimensional, one/two-dimensional and three-dimensional models are given and basic parameters such as volumetric flow rate, pressure and wall shear stresses (WSS) are defined. Basic cerebrovascular anatomy is recapitulated as this is required to understand a part of the complexity to cerebrovascular blood flow modelling. Finally, the need for patient-specific cerebrovascular blood flow modelling is described. Many cerebrovascular diseases are complex in which treatment is often based on experience and relatively small studies. Clinicians might be supported in treatment decisions by cerebrovascular blood flow models.

As cerebrovascular blood flow models are complex and might benefit from detailed 3D blood flow modelling, we initially performed such a model in 2 patients treated by proximal and distal occlusion of a complex intracranial aneurysm. In **chapter II** we present this model and its results. Based on patient-specific magnetic resonance angiography (MRA) we constructed a three-dimensional model. This model was used in a fluid-structure interaction analysis. Change in velocity, flow patterns, pressure distribution, WSS and wall tension were analysed and compared to follow-up imaging data. This pilot study showed the potential of such a 3D model to predict flow-changes indicating it might be a feasible patient-specific tool. However, the technique also proofed to be complex. Many different steps requiring input of a well-trained user were needed. Calculations took multiple days. This limits clinical usability. Hence, we opted to continue further development of a more simplified cerebrovascular blood flow model based on the Hagen-Poiseuille equations as we assumed this would be more likely to succeed in a clinical setting in the near future

In **chapter III** we performed a literature survey to identify important causes that might hamper development of such a simplified patient-specific blood flow model. Results discussed in this chapter will to some extend be applicable to more complex 3D flow modelling. We demonstrated to what extend different hemodynamic properties might be simplified to ease calculations. To generate a patient-specific model, adequate description of patient morphology is needed. This can be captured using existing

imaging techniques such as computed tomography angiography, MRA and 3D digital rotational angiography. Proximal and distal boundary conditions are of importance and need to be patient specific as well. In this aspect, especially distal boundary conditions are challenging as the cerebral arterial circulation is highly variable. This variability cannot be adequately measured using current imaging techniques. Also, the cerebral arterial circulation is known to show a highly variable collateral circulation. More proximal, this is defined in the anatomy of the circle of Willis, which can be captured using the same imaging techniques as mentioned above. On the distal side, leptomeningeal collateral anastomosis are present. These can only be captured indirectly, making patient-specific distal boundary conditions more challenging. Finally, the cerebral arterial circulation shows extensive autoregulation of which models of different complexity exist.

For the development of a simplified patient-specific model we first investigated the distal boundary conditions. We opted for a structured tree in which branching patterns are used to simulate the arterial tree up to the arteriole level. To adequately model this structured tree branching patterns specifically for the cerebral arterial circulation were needed. However, in literature these were missing in the range of arteries with a radius of 0.2-1 mm.

In **chapter IV** we validated a technique using 7T and 9.4T MRI for scanning human cerebral arterial plastic casts for acquisition of detailed morphological data of a large part of the cerebral circulation.

In **chapter V** we used this 7T and 9.4T MRI technique in conjunction with traditional manual measurements to gather branching patterns specific for the cerebral arterial tree in the range of 0.1-1 mm radius arteries. The data showed a large variation in branching patterns. Part of this variation might be explained by the measurement techniques, number of measurements and location of measurements in the vascular tree. This study also confirmed the cerebral arterial circulation follow the principle of minimum work (Murray's law).

In **chapter VI** a simplified mathematical blood flow model of the cerebral circulation was produced. The model used a set of linear equations based on the Hagen-Poiseuille equations, warranting fast calculation times. Blood pressure cuff measurement served as a simple accessible proximal boundary condition. A semi-automatic approach was used to segment patient-specific morphological data form a time-of-flight MRA. Distal boundary conditions were generated by using the branching patterns determined in **chapter V** by forming structured trees behind to the most distal segmented arteries. A

simple autoregulatory model was added changing peripheral resistances based on the mean arterial pressure. Calculated flow values were compared to phase-contrast MRI based measurements using the Noninvasive Optimal Vessel Analysis (NOVA) software. First, data of 10 healthy subjects was used to optimize parameters of autoregulation and distal boundary conditions. Next data of 20 healthy subjects were used in which NOVA flow measurements and calculated flow were compared to validate the model. The model showed to be accurate in a range that might proof feasible for clinical use.

In **chapter VII** based on the work presented in the current thesis, combined with data from the literature, future perspectives and challenges are described. For some purposes 3D models are likely required, especially when information on flow patterns and wall stresses are needed. However, based on the current thesis and literature, simplified models show great potential. They are easier to validate, interpret and likely implement. Hence, when possible researchers and physicians developing a patient-specific blood flow model for a specific clinical question should first consider the usage of such a simplified model.

Regardless of the complexity of a chosen model, further improvements in automation and workflow are needed. For 3D models also improvements in calculation speed are desirable. Additionally, adequate validation and sensitivity analysis are required to show the models strength and weaknesses. In 3D modelling these improvements and validation show a greater challenge, hence these models are not likely to become clinical applicable in the near future, compared to the more simplified models. Future research should focus on further development of 3D models and validation of already existing simplified models (after fine-tuning them to relevant clinical questions) in larger retrospective and prospective patient cohorts.

Addendum

Nederlandse samenvatting

Nederlandse samenvatting

In dit proefschrift wordt de ontwikkeling van een versimpeld patiënt-specifiek cerebrovasculair bloedstroom model geschikt voor klinisch gebruik beschreven.

Een algemene introductie en overzicht van dit proefschrift wordt gegeven in **hoofdstuk I**. Verschillende hemodynamische aspecten van belang bij het modelleren van bloedstroom, zoals laminaire versus turbulente flow, viscositeit en densiteit, worden behandeld. De elasticiteit van de arteriële vaatwand wordt beschreven aangezien deze in geval van pulsatiele bloedstroom een impact heeft op bloedstroom modellen. Een uitleg wordt geven over belangrijke verschillen tussen nul-dimensionale, een/twee-dimensionale en drie-dimensionale (3D) modellen. Basale parameters zoals volumestroom, druk en wall shear stresses (WSS) worden gedefinieerd. Basale cerebrovasculaire anatomie wordt herhaald aangezien begrip hiervan van belang is om de complexiteit van cerebrovasculaire bloedstroom modellering in te zien. Tot slot wordt nader toegelicht waarom er een noodzaak is tot patiënt-specifieke cerebrovasculaire bloedstroom modellen. Ondanks hun complexe aard wordt de behandeling van cerebrovasculaire ziekten vaak gebaseerd op ervaring en relatief kleine studies. Een patiënt-specifiek cerebrovasculair bloedstroom model kan mogelijk de clinicus ondersteunen in deze beslissingen.

Complexe 3D modellering zou zinvol kunnen zijn bij onderzoek naar cerebrovasculaire aandoeningen. Een dergelijk model en de voorspellingsresultaten hiervan worden in **hoofdstuk II** gepresenteerd. Er werd een 3D bloedstroom model ontwikkeld toegepast in 2 patiënten met complexe intracraniële aneurysmata welke zijn behandeld middels proximale en distale occlusie. Gebaseerd op een patiënt-specifiek magnetische resonantie angiografie (MRA) werd een 3D model geconstrueerd voor gebruik in een fluid-structure interactie analyse. Veranderingen in stroomsnelheid, flow patronen, drukverdeling, WSS en spanning in de wand werden geanalyseerd en vergeleken met beeldvorming vervaardigd gedurende follow-up. Dit proefonderzoek toonde de potentie van dergelijke complexe 3D modellen in het voorspellen van veranderingen in bloedstroom. Dit geeft aan dat een dergelijk model mogelijk geschikt zou zijn als een patiënt-specifiek hulpmiddel voor de clinicus. Echter toont het ook de complexiteit van een 3D model. In veel van de stappen is er input van de gebruiker nodig die hierbij goed getraind moet zijn in de verschillende aspecten van 3D modellering. Berekeningen duurden meerdere dagen. Dit limiteert de toepasbaarheid van een 3D model in een klinische setting. Daarom kozen wij er voor een versimpeld bloedstroom model van de cerebrovasculaire circulatie te ontwikkelen gebaseerd op de Hagen-Poiseuille vergelijkingen.

In **hoofdstuk III** hebben wij een literatuuronderzoek verricht om te pogen belangrijke factoren aan te wijzen welke de ontwikkeling van een versimpeld patiënt-specifiek cerebrovasculair bloedstroom model beperken. De resultaten zoals besproken in dit hoofdstuk zullen ook grotendeels toepasbaar zijn op meer complexe 3D modellen. We bespreken tot welke mate hemodynamische aspecten kunnen worden versimpeld om berekeningen te vergemakkelijken en versnellen. Om een patiënt-specifiek model te ontwikkelen is er een adequate omschrijving nodig van de morfologie van de arteriën van de patiënt. Deze kan worden verkregen middels beeldvormende technieken zoals computertomografie angiografie (CTA), MRA en 3D digitale rotatie angiografie. Proximale en distale randvoorwaarden zijn eveneens van groot belang. Met name distale randvoorwaarden zijn hierin uitdagend aangezien de cerebrale arteriële circulatie een grote variabiliteit vertoont. Deze variabiliteit kan niet nauwkeurig worden gemeten middels huidige beeldvormende technieken. Daarnaast is er tevens sprake van een variabele collaterale circulatie. Meer proximaal wordt deze collaterale circulatie gevormd door de cirkel van Willis. Informatie hierover kan relatief eenvoudig worden verkregen middels bovengenoemde beeldvormende technieken. Distaal wordt de collaterale circulatie gevormd door leptomeningeale anastomosen. Deze kunnen alleen indirect gemeten worden. Hierdoor zijn met name de distale randvoorwaarden uitdagend. Tot slot is het bekend dat de cerebrale arteriële circulatie een grote mate van autoregulatie vertoont. Hiervoor bestaan er reeds meerdere modellen in een verschillende mate van uitgebreidheid en complexiteit.

In de ontwikkeling van een patiënt-specifiek model hebben wij ons eerst gericht op de distale randvoorwaarden. Wij kozen ervoor een gestructureerde vaatboom tot op het niveau van arteriolen te modelleren op basis van vertakkingspatronen. Informatie over deze vertakkingspatronen voor cerebrale arteriën van 0.2-1 mm radius ontbreekt in de literatuur. Metingen aan cerebrale arteriële vaatboom zijn verricht om deze vertakkingspatronen te bepalen.

In **hoofdstuk IV** hebben wij een 7T en 9.4T MRI-techniek gevalideerd voor het scannen van plastic afgietsels van de humane cerebrale arteriële circulatie. Deze techniek zou verder gebruikt kunnen worden voor verzamelen van gedetailleerde morfologische informatie van een groot deel van de cerebrale circulatie.

In **hoofdstuk V** hebben wij deze 7T en 9.4T MRI-techniek samen met traditionele handmatige metingen gebruikt om informatie te verzamelen over vertakkingspatronen van de cerebrale arteriële vaatboom in vaten van 0.1-1 mm radius. De verzamelde data liet een grote variatie in vertakkingspatronen zien. Deels

zou deze variabiliteit verklaard kunnen worden uit foutmarge in de meettechniek, het aantal uitgevoerde metingen en locaties van metingen in de vaatboom. De data bevestigde verder dat de cerebrale arteriële circulatie de wet van minimum weerstand (Murray's wet) volgt.

In **hoofdstuk VI** presenteren we het versimpelde mathematische bloedstroom model voor de cerebrale arteriële circulatie zoals ontwikkeld in dit proefschrift. Het model gebruikt een set aan lineaire vergelijkingen gebaseerd op de wet van Hagen-Poiseuille. Hierdoor is de tijd benodigd voor berekeningen zeer kort. Een semiautomatische benadering werd gebruikt om de patiënt-specifieke morfologie te segmenteren op basis van een time-of-flight MRA. Een gestructureerde vaatboom gebaseerd op de vertakkingspatronen uit **hoofdstuk V** werd gebruikt als distale randvoorwaarden. Een simplistisch autoregulatie model werd toegevoegd waarbij de weerstanden van de distale randvoorwaarden werden gewijzigd op basis van de gemiddelde arteriële druk. Berekende bloedstroom waarden werden vergeleken met fase-contrast MRI-metingen verkregen middels Noninvasive Optimal Vessel Analysis (NOVA) software. Metingen in 10 gezonde vrijwilligers werden gebruikt om parameters in autoregulatie en distale randvoorwaarden te optimaliseren. Vervolgens werden metingen in 20 aanvullende gezonde vrijwilligers gebruikt voor validatie van het model. Het model toonde een accuraatheid binnen een bereik die mogelijk nog klinisch toepasbaar is.

Op basis van het werk beschreven in het huidige proefschrift en literatuur wordt in **hoofdstuk VII** een algemene discussie gegeven met beschrijving van toekomstige uitdagingen. Voor sommige doeleinden zal expliciet een 3D bloedstroom model nodig zijn, met name wanneer er informatie nodig is over bloedstroom patronen en krachten welke worden uitgeoefend op de vaatwand. Echter, gebaseerd op de huidige literatuur en het model gepresenteerd in dit proefschrift, tonen versimpelde bloedstroom modellen veel potentie. Ze zijn gemakkelijker te valideren, interpreteren en implementeren. Daarom zouden onderzoekers en clinici, wanneer mogelijk, eerst het gebruik van een versimpeld model moeten overwegen wanneer zij een patiënt-specifiek bloedstroom model ontwikkelen voor de cerebrale arteriële circulatie.

Verdere verbeteringen in automatisering en workflow zijn noodzakelijk, ongeacht de complexiteit van het model welke gekozen wordt voor een klinische vraagstelling. Daarnaast zijn er voor 3D modellen verbeteringen in snelheid van berekeningen gewenst. Bovendien zijn adequate validatie en sensitiviteitsanalyses benodigd om de sterke en zwakke punten van een model te achterhalen. Voor 3D modellering

ligt in deze validatie een nog grotere uitdaging dan in versimpelde modellen. Hierdoor is de kans kleiner dat 3D modellen op korte termijn een niveau bereiken geschikt voor klinisch gebruik. Onderzoek in de toekomst zou zich dan ook verder moeten richten op doorontwikkeling van de technieken voor 3D modellering met daarnaast validatie van reeds bestaande versimpelde modellen (eventueel na enige aanpassing op specifieke vraagstellingen) in grotere retrospectieve en prospectieve cohorten.

Addendum

Dankwoord

Savani en Henri

Mijn paranimfen. Al sinds onze studietijd zijn wij vrienden en maken we samen vele bijzondere momenten mee. Ik ben zowel blij als vereerd dat jullie op deze speciale dag tijdens de verdediging van mijn proefschrift mij bij willen staan.

MST

Collega's van de radiologie. Bedankt voor geven van de ruimte om mijn onderzoek af te maken naast mijn opleiding. Het is niet altijd even makkelijk als iemand uit de kliniek verdwijnt en het klinische werk op anderen aankomt.

Saskia, Bogusia en André

Dank voor de gezelligheid en vele goede gesprekken. Het was een waar plezier om naast jullie te kunnen werken. Jullie zijn als een hechte familie voor mij geworden.

Prof. Tulleken

Professor, dank voor de vele inspirerende gesprekken en kilo's aan chocolade. Het was een inspiratie om een tijd lang een kamer met u te mogen delen.

Elana

Bij Elana heb ik een warme en fijne werkplek gevonden. De vele gepassioneerde werknemers en stagiaires hebben allen bijgedragen aan het succes van dit proefschrift.

Familie

Ook mijn familie verdient een bedankje. In drukke tijden was ik niet altijd in staat bij alle gelegenheden, zoals verjaardagen, aanwezig te zijn. Toch voel ik me altijd welkom bij jullie. Dit warme gevoel helpt mij door drukke en soms zware tijden.

Danyta en Hiro

Mijn promotor en copromotor. Jullie niet aflatende begeleiding en geduld hebben gezorgd voor dit geweldige resultaat. We waren het niet altijd direct met elkaar eens, echter de vele discussies en fijne samenwerking heeft tot een nog mooier resultaat geleid dan initieel gedacht kon worden.

Er wordt wel eens gezegd dat het gezin de hoeksteen is van onze samenleving. Voor mij vormt mijn gezin één van de belangrijkste schakels in mijn leven en op weg naar dit proefschrift. Alleen met de steun van mijn vrouw Danyta en de ruimte die mijn gezin mij gegeven heeft, kon dit proefschrift tot stand komen.

Bart en Tristan

Prof Kumar

Dear prof Krischna Kumar. I thoroughly enjoyed my visits to the Indian Institute of Technology Madras. I was warmly welcomed by you and your team. I sincerely hope that there will be room for further collaboration in the future.

Allereerst wil ik mijn ouders bedanken. Zij hebben zich er altijd maximaal voor ingezet dat ik alle kansen in het leven kreeg en mijzelf maximaal kon ontwikkelen. Van wijze raad en goede opvoeding tot aan het financieren van mijn studie. Zonder hun continue inzet, zorg en steun was ik niet zo ver gekomen.

Moeder en Vader


Berend Hillen
Prof. Berend Hillen. Uw werk heeft ten grondslag gelegen aan het bloedstroom model in mijn proefschrift. Uw raad en advies was van grote waarde om dit proefschrift tot een succesvol einde te brengen.
Jeroen Hendrikse, Anita en Annette
Ik vond in jullie, samen met andere onderzoekers van het Image Sciences Institute en het UMC Utrecht, een groep gepassioneerde onderzoekers. Jullie bijdrage was onmisbaar voor het tot een succesvol einde brengen van mijn proefschrift.
Claartje
Claartje. Dank voor de gezelligheid en je hulp bij de soms onlogische rompslomp bij subsidies, financiële en organisatorische zaken.
Jaco
Jaco, in een groot deel van mijn project was je bijna als een copromotor voor me en een belangrijke schakel in het succes van meerdere hoofdstukken uit dit proefschrift. Ik wil je dan bedanken voor de fijne en goede samenwerking.
Sander
Sander. Uren hebben wij voor een whiteboard gestaan om verscheidene formules en scripts uit te denken. Vele mooie en leuke projecten hebben wij samen mogen uitvoeren, van servers installeren tot printplaten strijken en etsen. Dank voor de leuke, leerzame en mooie tijd samen.
UMC Utrecht
Zonder de enthousiaste en vriendelijke mensen die ik op een aantal plekken in het UMC Utrecht heb gevonden was mijn proefschrift niet tot stand gekomen.
Anatomie
Prof. Roland Bleys, Willem van Wolferen, Simon Plomp en Fiona van Zoomeren. Dank voor de mogelijkheid meerdere maanden gebruik te mogen maken van de faciliteiten op jullie afdeling anatomie en de hulp bij het opzetten van experimenten.
Beoordelingscommissie
Aan de leden van de beoordelingscommissie, aan jullie was de zware taak opgelegd mijn proefschrift te lezen en te onderwerpen aan jullie grondig oordeel. Hiervoor mijn dank.
Sindhoor Bhat
Dear Bhat. We had great fun and many wonderful experiences together. Finding suitable food during exchange periods was challenging but successful. The same was true for our collaboration. We did not always initially agree but reached successful results in the end. I wish you and your family all the best in life and hope to see you again someday.

Addendum

Curriculum vitae

Curriculum vitae

Jasper Hermannus Gerhardus Helthuis was born on the 6th of May 1989 in Almelo, The Netherlands. After finishing his primary education, he obtained in 2007 his VWO gymnasium degree at the Pius X College in Almelo with profiles "nature and healthy" and "nature and technology" including additional courses in Greek, Economy, Management and Organization and Philosophy. He started his medical education at Utrecht University. He received his bachelor and master degree in 2010 and 2013, respectively. He took elective courses in Biotechnology, Pain management, Neurosurgery and Head and Neck Anatomy. He performed an internship aboard in otolaryngology and head and neck surgery in the hospital for Sick Children and The Toronto General Hospital in Toronto, Canada, under supervision of Prof. Dr. Ralph Gilbert and Prof. Dr. Paolo Campisi. During his scientific internship at the ELANA laboratory in Utrecht, under guidance of Prof. Dr. Albert van der Zwan, he focused on optimizing the laser technique of the new Suture-less Excimer Laser Assisted Nonocclusive Anastomosis (SELANA) and determining the learning curve of this new neurosurgical and cardiac device. After obtaining his medical degree, he started as a PhD candidate at the Neurosurgical Department of the University Medical Centre Utrecht and the Brain Technology Institute in Utrecht. He worked under direct guidance of his promotor Prof. Dr. Albert van der Zwan and co-promotor Dr. Tristan van Doormaal. His focus was on development of a clinical applicable blood flow model to aid neurosurgeons in difficult treatment decisions. He started his residency in radiology under the supervision of Dr. Caroline Klazen at Medisch Spectrum Twente in Enschede. Jasper Helthuis is married to Danyta Isthylova Tedjo and they live together with their son Hiro The Helthuis in Almelo.